ATTITUDE ESTIMATION AND CONTROL OF A DUCTED FAN VTOL UAV

by

Andrew David Roberts

Under the Supervision of Dr. Abdelhamid Tayebi

A Thesis Submitted in Partial Fulfillment

of the Requirements for the Degree of

Master of Science

in Control Engineering

Lakehead University, Thunder Bay, Ontario

August 2007

Library and
Archives Canada

Published Heritage
Branch

395 Wellington Street
Ottawa ON K1A 0N4
Canada

Bibliothèque et
Archives Canada

Direction du
Patrimoine de l'édition

395, rue Wellington
Ottawa ON K1A 0N4
Canada

Your file Votre référence
ISBN: 978-0-494-31836-2
Our file Notre référence
ISBN: 978-0-494-31836-2

NOTICE:
The author has granted a non-exclusive license allowing Library and Archives Canada to reproduce, publish, archive, preserve, conserve, communicate to the public by telecommunication or on the Internet, loan, distribute and sell theses worldwide, for commercial or non-commercial purposes, in microform, paper, electronic and/or any other formats.

The author retains copyright ownership and moral rights in this thesis. Neither the thesis nor substantial extracts from it may be printed or otherwise reproduced without the author's permission.

AVIS:
L'auteur a accordé une licence non exclusive permettant à la Bibliothèque et Archives Canada de reproduire, publier, archiver, sauvegarder, conserver, transmettre au public par télécommunication ou par l'Internet, prêter, distribuer et vendre des thèses partout dans le monde, à des fins commerciales ou autres, sur support microforme, papier, électronique et/ou autres formats.

L'auteur conserve la propriété du droit d'auteur et des droits moraux qui protège cette thèse. Ni la thèse ni des extraits substantiels de celle-ci ne doivent être imprimés ou autrement reproduits sans son autorisation.

In compliance with the Canadian Privacy Act some supporting forms may have been removed from this thesis.

While these forms may be included in the document page count, their removal does not represent any loss of content from the thesis.

Conformément à la loi canadienne sur la protection de la vie privée, quelques formulaires secondaires ont été enlevés de cette thèse.

Bien que ces formulaires aient inclus dans la pagination, il n'y aura aucun contenu manquant.

Canada

Reproduced with permission of the copyright owner. Further reproduction prohibited without permission.

Abstract

A significant area of current research is to develop aircraft which are unmanned. More specifically, some researchers are focusing on hovering type aircraft, or vertical take-off and landing (VTOL) aircraft. Since these types of aircraft do not need to be constantly in motion to maintain lift, they have certain advantages over fixed-wing aircraft. Suitable applications could involve aerial photography, atmospheric measurements or surveillance and defense. The most common type of VTOL aircraft is the helicopter. One disadvantage of this aircraft is the degree of danger involved due to the exposed rotor blades. This is one motivating factor behind the *ducted fan* system. This type of system uses a rotor which is enclosed in a aerodynamically shaped duct. The introduction of a duct also tends to increase the thrust obtained from the rotor, which is known as *thrust augmentation*. In traditional helicopters a tail rotor is used to counter the torque acting on the main rotor which is mainly due to the aerodynamic drag experienced by the rotor. To counter the rotor torque in the ducted fan system, a second counter-rotating rotor can be used. The two rotors are placed in series which is also known as a *coaxial rotor*.

In order for VTOL aircraft to be autonomous, a control system is required to provide attitude stabilization. Using this type of control, a pilot could then direct the aircraft while the onboard controller performs the required action to keep the aircraft stable and flying at the desired operating point. One crucial part in achieving this task is the requirement of accurate knowledge of the system's attitude. To obtain information related to the systems attitude, a number of inertial sensors can be used. These sensors usually consist of accelerometers, magnetometers, and gyroscopes. All of these sensors are often used since each sensor has its own limitations.

A description of the system aerodynamics is given to describe the system forces and torques. Also, a thorough description of several forms of attitude representation is given. A PD controller for the attitude regulation has been successfully implemented based on the use of attitude estimation algorithms relying on the IMU signals.

Simulations and experimental results are given to show the performance of the estimation and control algorithms. Also, a fully operational prototype has been developed which is used to carry out experimental results.

Acknowledgments

Throughout my undergraduate and masters degree at Lakehead University, I have had the honor and privilege of working with Dr. Abdelhamid Tayebi as my supervisor, to whom I cannot express enough gratitude and appreciation for his guidance and support throughout this thesis and my academic career.

I would like to offer my sincere appreciation to Kailash Bhatia for his help with building the system prototype. His innovative ideas matched with his expertise and skill have solved many of the challenges we faced. I would like to thank Warren Paju for his help in building the system and choosing key system components. I also offer my thanks to Manfred Klein and Bruce Misner who have provided me with the equipment and parts I needed for the project.

I would like to express my appreciation to all of the professors who I have had the pleasure to learn from while at Lakehead University, and to my fellow graduate students and friends for their help, encouragement, and their company which has made my stay in Thunder Bay even more enjoyable.

I would like to thank my parents and family, for their endless love and support, and for their encouragement for me to further my education in engineering.

Finally, I would like to thank Erin, for her continued love and belief in me to succeed.

Andrew D. Roberts

Contents

List of Figures

Chapter 1

Introduction

The idea of a hovering aircraft is not by any means a new idea. New advances in technology may have made it easier to develop some of the aircraft which we are familiar with, yet the history of vertical take-off and landing (VTOL) aircraft can date back centuries. In fact, the concept of a man-operated hovering flying machine was suggested by Leonardo da Vinci in one of his sketches in the 15th century. Even Leonardo's design was inspired by Archimedes (200BC) and ancient Chinese flying toys. Throughout the last couple of centuries a number of inventors have developed aircraft prototypes of varying size and limited success. Yet, it wasn't until the introduction of the internal combustion engine when then idea of practically realistic VTOL aircraft materialized.

1.1 The Coaxial Rotor

From the very first VTOL aircraft prototypes, designers were well aware of the requirement to counter the torque created by the spinning rotors. The most popular solution is the helicopter tail-rotor. One disadvantage of a tail-rotor is that power is wasted producing thrust which does not contribute to the lift of the aircraft. In an effort to remove this waste of thrust, a number of early prototypes considered the use of two main rotors which rotated in opposite directions to cancel the aerodynamic torques, while each rotor contributed to the lift of the aircraft. This design, known as the coaxial rotor, was first patented by Henry Bright in 1859. Although they are less common, coaxial rotor helicopters and other VTOL aircraft have recently been developed for commercial and military use. One example of a coaxial rotor helicopter is the Russian Kamov Ka-50. In fact the Kamov company produced a series of coaxial helicopters of this type. A disadvantage associated with coaxial helicopters is that it is not usually practical to implement two engines. As a result a complex transmission, for example a planetary gearset, is used to spin the rotors in opposite directions and at varying speeds, all powered from the same motor.

A type of dual-rotor helicopter that is more common is the tandem style helicopter. This helicopter uses two or more rotors that are spinning on different axes. A popular helicopter which uses this topology is the Bell Osprey V-22. Other helicopters have been designed where the rotors overlap, which is a cross between the coaxial and tandem arrangements. With multiple-rotor systems, the airflow pattern created due to the rotor (known as the *wake*) can be considerably different than that of single rotor designs. Also, in coaxial rotors, since the lower rotor is operating in the wake of upper rotor, it is less efficient at producing thrust than the top rotor. Considerable research has been focused on this area, for example [2].

1.2 The Ducted Fan

The ducted fan, as its name implies, is created by surrounding a fan, propeller, or rotor by a shroud. Since a rotating propeller creates a pressure distribution over the area of the propeller, vortices are created at the tips of the propellers resulting in a decrease in efficiency. By introducing a shroud around the propeller, the pressure distribution over the rotors is increased over an open rotor. This results in improved efficiency and greater thrust, which is known as *thrust augmentation.* This is especially true at low duct velocities. However, at higher velocities the improvement in thrust can be negligible or even be less than an unshrouded rotor. This is due to the increased aerodynamic drag of the duct itself. Therefore, the use of ducted fans are more common in VTOL systems, which usually exhibit lower velocities. Another advantage stems from the fact that the rotors are no longer exposed, as is the case with helicopters. This feature can improve the safety of the aircraft, especially when smaller scale systems are used in close proximity to operators or other personnel. Ducted fans have been used as propulsive devices in a number of large-scale aircraft, for example the British Egley EA7 Optica shown in Figure (1.1)[1] and the Bell X-22 ducted fan aircraft.

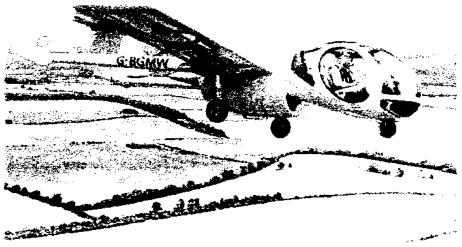

Figure 1.1: Edgley EA7 Optica

The ducted fan is somewhat more popular for use with smaller scale systems, and a number of groups have used the ducted fan as the primary aircraft structure, for example [11], [18] and [27]. This is possible due to the advent of smaller and more powerful electronics which can enable these systems to fly remotely or as fully autonomous systems. These systems are usually actuated with vanes or control surfaces at the exit of the duct, known as *thrust vectoring.* These control surfaces can vary from system to system since sometimes a single rotor is used requiring the control surfaces to counter the rotor aerodynamic torque. Therefore, on some systems some vanes may have more fins or increased surface area to counter this torque while leaving overhead to produce the required stabilizing torques on the other system axes.

These types of systems, as shown in Figure (1.2), have been the focus of several research groups due to the many potential applications where unmanned aircraft are desired or where human presence may be hazardous.

A main objective of this thesis is to give a thorough description of the theory used to develop a ducted fan VTOL UAV. Since most, if not all, of the system forces are created by airflow inside and outside the system, some aerodynamic analysis is required to anticipate the thrust due to the rotors, as well as the forces and torques generated by the control surfaces.

---

[1] Photograph curtesy of Johan Visschedijk, 1000aircraftphotos.com

1.3 Attitude Estimation

To enable VTOL aircraft to operate autonomously, feedback is required which contains information about the systems attitude, or orientation, in order to provide automatic control of the system. Typically, this type of feedback is obtained using inertial sensors such as gyroscopes, accelerometers and magnetometers. The study of attitude estimation from inertial sensors has been the focus of many researchers due to the high number of applications to which it can be applied. Mobile robots, whether they exist in the air, on the ground or under water, can all use the same types of inertial sensors to obtain estimates of the system orientation. Sophisticated aircraft navigation systems are not always available for small vehicles due to size and weight constraints, in addition to the substantial cost. These systems can use high-quality inertial sensors in addition to other navigational systems such as GPS to obtain accurate knowledge of the system attitude. Therefore, some researchers have focused on using low-cost sensors in addition to the use of adaptive estimation algorithms.

There are several forms of attitude representation which can be used to describe the system's attitude. Among the most common are the quaternion, the direct cosine matrix, and Euler angles. A thorough description of these forms is given which is based on the work presented in [21], in addition to [6], [14], and [23]. This description includes the attitude kinematics related to the attitude representation. As a result, differential equations which describe the system attitude over time as a function of the system angular velocity are given.

One problem associated with the low cost sensors is the constant bias of the gyroscope signals, since integration of these signals results in drifting of the attitude estimates. However, knowledge of the gyroscope bias is not a sufficient condition to guarantee accurate accounts of the attitude. Therefore, alternative ways to obtain attitude estimation in addition to the gyroscope is desired. One alternative is to measure the system attitude using low-pass inertial sensors. In general, this method provides accurate estimates under steady state conditions, or at low frequencies. This is due to the fact that the accelerometers are affected by physical accelerations of the system, and both accelerometers and magnetometers have a limited bandwidth and are affected by noise. Furthermore, the problem of bandwidth is usually compounded with the effect of low-pass filters which are most likely implemented in the system to reduce the effect of noise and other disturbances. The relationship between frequency and sensor accuracy for the gyroscopes is opposite to that of accelerometers and magnetometers. The gyroscope signals tend to be less accurate at low frequencies due to a pseudo-constant sensor bias. To address this relationship between frequency and sensor accuracy, complementary filters have been used to *fuse* the different measurements.

1.4 Attitude Stabilization

The main difficulty of the attitude stabilization problem is obtaining accurate estimates of the system's attitude. Still, controllers have been presented in the past which assume the system's attitude is known. In [7] and [29] the attitude stabilization problem has been solved providing the system attitude and angular velocity are known exactly. In most cases, a PD controller is used where the proportional and derivative feedback are provided by the actual (or estimated) quaternion and system angular velocity, respectively. In [26], a similar PD controller is presented which also provides compensation for the gyroscopic torques of the system.

Since knowledge of the system states is not always possible some authors have investigated attitude stabilization where the angular velocity is unknown, for example [12] and [24]. Assuming that the system attitude is known and a biased angular velocity measurement is obtained, a number of bias observers have been presented by [13] and [28]. An attitude estimator has been presented by [20] assuming the angular velocity is known exactly and that system accelerations are small. Complementary filtering has been used with biased angular velocity measurements and measurement of the system attitude using low-pass sensors by [26], [27], [13] and [5]. Different approaches to the estimation problem have also been presented. These methods include optimal estimation methods and Kalman filtering. For example, in [9] an approach is used which evaluates the probability of a system's orientation based on vector measurements. In [20] a Kalman filter is used with a switching topology that uses either the gyroscopes or the vector observations, depending on the frequency content of the input signals. In the case where the attitude and angular velocity are unknown, feedback of attitude estimates with PD control have been shown, experimentally (for example see [18] and [26]), to stabilize the system, yet theoretically this remains an open problem.

In general, angular velocity and low-pass attitude measurements are used in attitude estimation. A significant portion of the literature assumes that either the system angular velocity or the system attitude are known. In this thesis, it is assumed that neither of these states are ideal. The work in this thesis is based on the work presented in [27]. Three different methods are shown which used biased angular velocity measurements and measurements from low-pass sensors to obtain estimates of the system attitude and angular velocity sensor bias. In two of the three algorithms, a complementary filter is used. A number of simulations are given to show the performance of the attitude estimation in a closed loop system with PD control. Some simulations are given which show the effect of system accelerations, which deteriorate the quality of the measurement obtained from the low-pass sensors since accelerometers are used. Finally, a description of a system prototype is given, which is used to test the theory and provide experimental results.

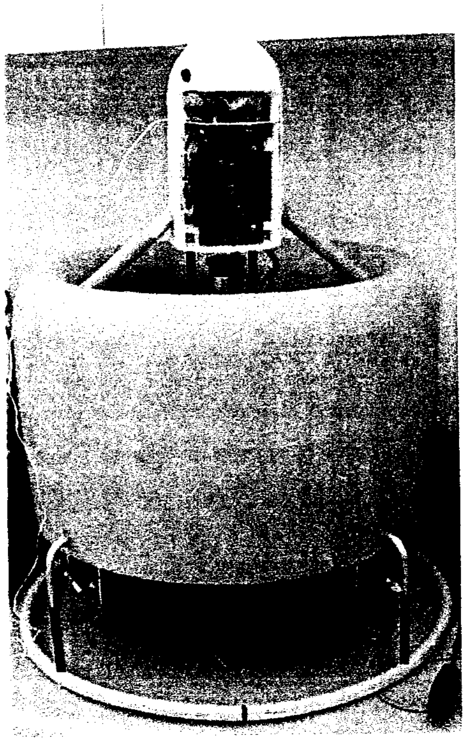

Figure 1.2: Lakehead University Ducted Fan System

Chapter 2

Aerodynamic Theory

For the proposed system, almost all system forces and torques are a result of the motion of air through and around the duct. An investigation of these aerodynamic forces is required to explain qualitatively, and where possible, quantitatively the forces and torques which are acting on the system. The analysis presented is a summarized review of the work in [1], [8], [10] and [15]. Many assumptions and approximations are often used for aerodynamic analysis since effects such as turbulent flow and vortices are difficult to predict and describe analytically. This leads to extensive wind tunnel testing which is often used to verify the assumptions used for specific aircraft and to measure the net aerodynamic forces. External disturbances can be avoided if operating indoors, yet practical aircraft should have the ability to operate outdoors in the presence of unpredictable airflow. In order to maintain a desired position or velocity in the presence of unpredicted airflow, it can be useful for the aircraft controller to be robust or to include the effect of external forces (for example see [18]).

The first objective of this chapter is to review commonly used aeronautical terms and to give an introduction to general aerodynamic forces. Usually the standard terminology is focused on fixed-wing or helicopter type applications, but can be easily applied to the ducted fan. This introduction is followed by a study of the relationship between the thrust produced by the rotor and the resulting airflow which it creates. The use of a duct around a propeller creates significant differences between a conventional helicopter and a ducted fan, which will be explored. Finally, an explanation of how forces and moments are created on an airfoil is given. This explanation can be applied to the rotor blades and control ailerons to quantitatively describe the forces and torques acting on the system.

2.1 Preliminary

An introduction for some basic aerodynamic principles is given which is based on [1] and [15]. A simple airfoil is illustrated by Figure 2.1. A characteristic of this airfoil is that the upper surface contour is different from the lower surface. Many wings share this asymmetric shape which is known as *camber*. A dashed line shows the *mean camber line*, which gives the midpoint of the local thickness from the leading to trailing edges. The *chord*, c, is the shortest distance from the leading edge to the trailing edge of an airfoil. The local camber is defined as the distance from the chord line to the mean camber line, which is perpendicular to the chord line. For airfoils with zero camber, the mean camber line is the same as the chord. The wing *span*, b, is the length of the wing, shown in Figure 2.1 without the presence of an aircraft fuselage. The *aspect ratio*, AR, of a wing is a function of the span and the wing surface area, S, given by (2.1).

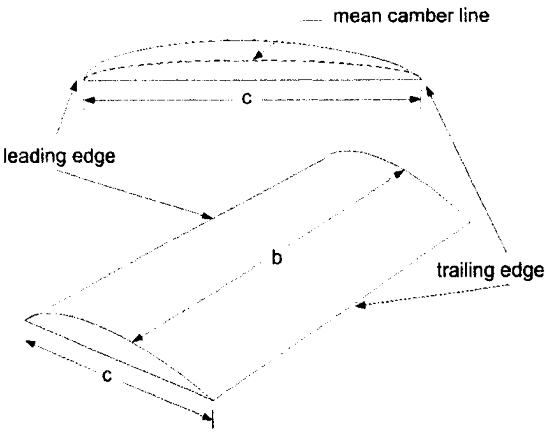

Figure 2.1: Airfoil Physical Parameters

$$\text{Aspect Ratio} = AR = \frac{b^2}{S} \tag{2.1}$$

These physical descriptions can be applied to the ducted fan system by considering the duct as a circular wing, also known as an annular airfoil. Figure 2.2 shows the duct which encloses two propellers. The duct airfoil is shown using dashed lines which is the cross section of the duct. The airfoil chord is the same as the height of the duct. Since the duct does not achieve lift in the same manner as a fixed-wing aircraft, aerodynamic theory which addresses airflow over an airfoil does not apply to the duct in the same manner. However, the propellers and control ailerons are airfoils where conventional aerodynamic theory applies.

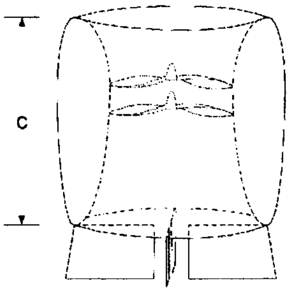

Figure 2.2: Duct Airfoil

When an airfoil is immersed in moving air, a *flow field* is created. An example of a flow field is given by Figure 2.3. The flow field describes the direction and velocity of the air surrounding the airfoil. The flow field is shown using a series of dashed lines, known as *stream lines.* Stream lines describe the motion of a finite fluid element within the flow field. By definition, the mass flow for a stream line has no normal component to the stream line boundary, or in other words, a particle cannot cross a streamline since its motion is parallel to it. This flow field creates a pressure distribution on the lower and upper surfaces which results in aerodynamic forces.

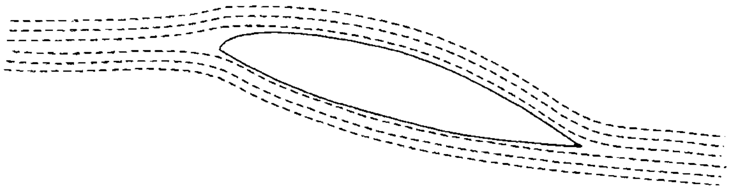

Figure 2.3: Example of a Flow Field

To describe the aerodynamic forces, consider Figure 2.4 which illustrates an airfoil immersed in a moving field of air with a velocity v_∞. The angle of attack, α, is the angle between the direction of airflow and the chord line of the airfoil. The interaction of the air on the wing results in the net force F. This net force is decomposed into vectors which are perpendicular and parallel to the direction of the incoming air, also known as the *free stream.* These vectors are the lift, L, and drag, D. Since these vectors are defined with respect to the direction of the free stream, the lift cannot be always considered to be exactly vertical with respect to the inertial or body-fixed frames of reference.

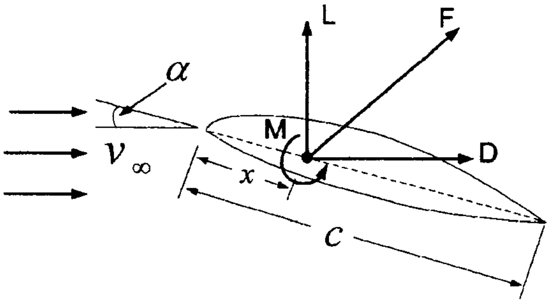

Figure 2.4: Resulting Forces of an Airfoil

In addition to the lift and drag, the moment M is caused since the pressure distribution on the upper and lower surfaces is not uniform. Figure 2.5 illustrates the effective non-uniform pressure distribution which results in the force F and moment M. The forces on an airfoil are taken at a point along the chord line at a distance x from the leading edge. The value of x where $M = 0$ is known as the aerodynamic center of pressure. Due to the absence of M at the center of pressure, it is useful to use this point to model the aerodynamic forces. For symmetric airfoils, the center of pressure is always located at a quarter of the chord length, or $x = c/4$.

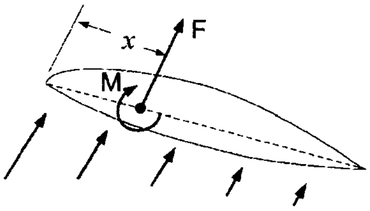

Figure 2.5: Non-uniform Pressure Distribution

2.1.1 Bernoulli's Equation

Although air is actually a gas, the movement of air can be modeled as a fluid. In fact, aerodynamics is a subset of fluid dynamics. One important and fundamental property of fluid dynamics is called *dynamic pressure*. Dynamic pressure exists when a fluid, in this case air, has a net velocity greater than zero. The dynamic pressure, p_d, is a function of the fluid velocity, v, and fluid density, ρ, and is given by

$$p_d = \frac{1}{2}\rho v^2 \tag{2.2}$$

Another type of pressure is known as *static pressure*, p. This is the thermodynamic pressure or the pressure experienced by a fluid particle from the particle's point of reference. A relationship between the static and dynamic pressure known as *Bernoulli's equation* is given by

$$p + p_d = \text{constant} \tag{2.3}$$

Note that this is a simplified version of Bernoulli's equation since it does not account for the effect of potential energy as a function of gravity.

Bernoulli's equation is only valid for uniform, incompressible, inviscid (frictionless) flows where no energy is supplied to the system. An example of an application of Bernoulli's equation is shown in Figure 2.6, which illustrates air flowing through an arbitrary converging duct. Applying Bernoulli's equation, the pressure and airflow velocity is considered at regions 1 and 2 within the duct by

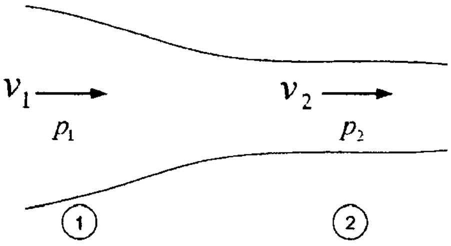

Figure 2.6: Static and Dynamic Pressure – Bernoulli's Equation

$$p_1 + \frac{1}{2}\rho v_1^2 = p_2 + \frac{1}{2}\rho v_2^2 \tag{2.4}$$

Since the velocity of the air must increase in a converging duct (assuming incompressible flow), the dynamic pressure in region 2 will increase. Since the sum of static and dynamic pressure is constant, the static pressure in region 2 is less than region 1. This example can be extended to the airflow over a wing. If the flow field velocity is known accurately over the airfoil, then the airfoil pressure distributions can be obtained. Since pressure is a force per area, the net force on an airfoil can be determined from the obtained pressure distributions. The challenge is then focused on determining the flow field velocity for a given airfoil.

2.1.2 Dimensionless Coefficients

Often in aerodynamic theory dimensionless coefficients are used to describe the aerodynamic forces. Since the ducted fan system shares characteristics with fixed-wing aircraft as well as helicopters, these quantities can be expressed differently. Since the lift and drag can change with respect to the direction of the free stream, or the airfoil angle of attack, these coefficients are also a function of the angle of attack. Expressions for the lift and drag coefficients for an airfoil are given by

$$C_L = \frac{L}{\frac{1}{2}\rho S v_\infty^2} \tag{2.5}$$

$$C_D = \frac{D}{\frac{1}{2}\rho S v_\infty^2} \tag{2.6}$$

where v_∞ is the free stream velocity, and S is the airfoil surface area. Another commonly used aerodynamic force is *thrust*. The convention shown for the thrust coefficient by

$$C_T = \frac{T}{\frac{1}{2}\rho A(\omega R)^2} \tag{2.7}$$

corresponds to helicopter design, where T is the thrust. Since the thrust for a helicopter rotor is related to the rotor speed, ω, rather than the free stream velocity, the thrust coefficient is given with respect to the rotor speed and the rotor radius, R. The quantity A is used to define the rotor disk area, $A = \pi R^2$. The power coefficient, C_P, describes the ideal power consumed by the rotor with respect to the rotor speed and radius. Since $P = Tv_i$, the ideal power coefficient is related to the thrust coefficient by

$$C_P = \frac{P}{\frac{1}{2}\rho A(\omega R)^3} = \sqrt{\frac{a_d}{2}} C_T^{3/2} \tag{2.8}$$

where a_d is a ratio of the rotor disk area to the duct exit area. Due to unaccounted system losses, the actual power coefficient will be greater than the predicted or ideal value for a given value of thrust. To describe the *induced* power coefficient, C_{P_i}, the aerodynamic power factor κ is used (see [10]) as shown in

$$C_{P_i} = \frac{P_i}{\frac{1}{2}\rho A(\omega R)^3} = \kappa\sqrt{\frac{a_d}{2}} C_T^{3/2} \tag{2.9}$$

$$P_i = \kappa P \tag{2.10}$$

The *Reynolds number*, which is given by

$$\mathrm{Re} = \frac{\rho v x}{\mu} \tag{2.11}$$

is a dimensionless coefficient which is used to estimate the quality or properties of an airflow over some airfoil, where ρ is the fluid density, x is the length of the airfoil parallel to the flow stream, v is the airflow velocity, and μ is the fluid viscosity. Higher Reynolds numbers are attributed to turbulent flows or when the flow stream becomes separated (see Aerodynamic Forces on an Airfoil for description of flow separation).

The speed of an airflow or airfoil is often given in relation to the speed of sound, v_{sound} (see Appendix). The ratio of the airspeed to the speed of sound, M, is known as the *mach number.* The mach number, given by

$$M = \frac{v}{v_{sound}} \tag{2.12}$$

is useful especially when making assumptions regarding the compressibility of air. For mach numbers less than unity, air is often assumed to be incompressible, or ρ is constant.

2.2 Vertical Flight, Thrust, and the Resulting Airflow

It is obvious that the ducted fan system produces lift by drawing air through the duct by the propellers. In addition to the air drawn by the propellers, other air can be forced into the duct due to vertical climb (referenced to body-fixed frame) or wind. Since the aerodynamic forces caused by the control ailerons are dependent on the airflow through the duct, a relationship between the thrust, motion of the aircraft and the resulting airflow is required. For comparison purposes, aerodynamic theory for a ductless system, or a helicopter, is presented followed by the introduction of a duct.

2.2.1 Open Rotor Theory – The Helicopter

According to Newton's laws of motion, the thrust (or vertical force) is the result of accelerating a mass of air. Figure (2.7) illustrates the movement of air through an open rotor. There are several different regions specified by a number within a circle. Region 0 is located at a distance sufficiently far above the rotor that the air is not affected by the rotor. In region 0 the air can be modeled to have a downward velocity of v_0 which is used to model vertical movement. In hover and in the absence of wind, one can assume that the air at a distance sufficiently far above the rotor has zero velocity, or $v_0 = 0$. Below this region, air is drawn by the rotor and is accelerated through the rotor until it reaches the fully developed wake region. The velocity of the airflow just above the rotor is known as the *induced velocity*, v_i. In the wake region, the velocity of the airflow is known as the *exit velocity*, v_e. The region of moving air is called the *slipstream* which is identified by the dashed lines. For a system in equilibrium, for example hover, the slipstream is constant assuming no external disturbances. The propeller is modeled as a thin disk where a pressure differential occurs. An expression for the mass flow rate is given by

$$\dot{m} = \rho A v_i = \rho A_e v_e \tag{2.13}$$

where v_i and v_e are the induced and exit airflow velocity, respectively. Assuming the induced velocity is uniform, irrotational, and the system is in equilibrium (for example hover), the mass flow rate for the air moving through the rotor is constant. The mass flow rate through the rotor must be the same as the mass

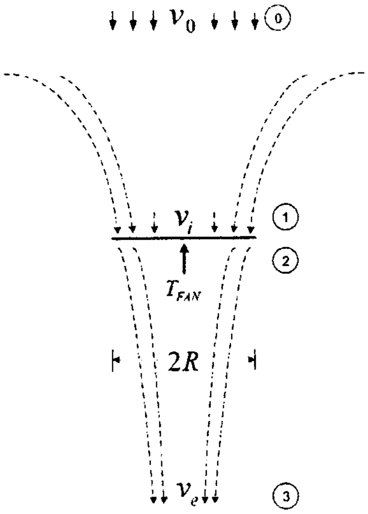

Figure 2.7: Open Rotor

flow rate at the duct exit due to the conservation of mass. The rotor disk area and duct exit area are given by A and A_e, respectively. The force or thrust produced is equal to the mass flow rate times the total change in velocity, which for a state of hover is equal to the exit velocity.

$$T = \dot{m}\left(v_e - v_0\right) = \dot{m}v_e \tag{2.14}$$

The velocity of the airflow can be determined using the change in kinetic energy over time, which is also the power supplied to the airflow. Since power is given as force times velocity, the power supplied to the air is the product of the rotor thrust and the induced velocity,

$$P = Tv_i \tag{2.15}$$

If the system losses are assumed to be negligible, the power supplied by the system is also equal to the change in kinetic energy ΔKE, of the airflow over time t, as shown by

$$P = \frac{\Delta KE}{t} = \frac{1}{2}\dot{m}(v_e - v_0) = \frac{1}{2}\dot{m}v_e \tag{2.16}$$

Since the power supplied to the system must be the same for (2.15) and (2.16), this yields a relationship between the induced velocity and the exit velocity given by

$$v_e = 2v_i \tag{2.17}$$

From the definition of the mass flow rate in (2.13), this leads to a relationship between the rotor area and the exit wake area. Also, from (2.14), a relationship between the thrust and the induced velocity is obtained, given by

$$A_e = \frac{A}{2} \tag{2.18}$$

$$T = \dot{m}v_i = 2\rho A v_i^2 \tag{2.19}$$

Bernoulli's equation can also be used to determine an expression for the thrust. Since the propeller is modeled as a thin disk, the thrust produced can be given as the product of the pressure distribution over the disk and the disk area. Bernoulli's equation is applied for regions 0 to 1, and 2 to 3, but cannot be applied for regions 1 to 2 since the propeller adds energy to the slip stream. This application of Bernoulli's equation leads to

$$p_0 = p_1 + \frac{1}{2}\rho v_i^2 \tag{2.20}$$

$$p_2 + \frac{1}{2}\rho v_i^2 = p_0 + \frac{1}{2}\rho v_e^2 \tag{2.21}$$

$$T = (p_2 - p_1)\,A = \frac{1}{2}\rho A v_e^2 \tag{2.22}$$

Comparison of (2.19) and (2.22) leads to the same conclusions given by (2.17) and (2.18). The area reduction of the wake is known as wake contraction which can be observed for real helicopters. The theory exaggerates the wake contraction since friction, non-uniform and rotational flow, which all consume power, are not accounted for.

2.2.2 Single Rotor Ducted Fan

As shown in [10], the same method used to analyze the airflow for a helicopter can be applied to the ducted fan assuming certain duct induced effects are accounted for. Introducing the duct prohibits wake contraction until the airflow is outside the duct. If the duct is divergent, or the duct area is increased towards the duct exit, then the airflow tends to follow the direction of the duct contour due to the *coanda* effect. The coanda effect is the phenomenon where a moving fluid tends to follow the contour of a smooth surface. As a result, the wake will have a larger area than that of a helicopter. In addition to the thrust provided by the rotor, the duct provides additional thrust which can be attributed to the pressure distributions above and below the propeller. For a helicopter, another source of inefficiency is attributed to *tip loss*. Tip loss occurs due to the high pressure difference between the bottom and top of the rotor. At the wing tips, air flows from below the rotor creating vortices. For a ducted system, provided the separation between the duct wall and the rotor is minimal, the vortices and tip losses can be reduced. Another problem with the helicopter theory is that a single rotor introduces a rotational wake, where lost energy is not accounted for. The wake rotation will be reduced in the ducted fan system due to the two counter-rotating propellers, also known as a coaxial rotor. As a consequence, the two propellers will create a very complex wake which may be turbulent and thus will still consume energy. A significant disadvantage of coaxial ducted fan system is that thrust will not be evenly divided amongst the two propellers.

Before considering a coaxial system, the momentum theory will be applied to a single rotor ducted fan, which is illustrated by Figure 2.8. The area of the wake, A_e, is given in relation to the propeller disk area using the ratio a_d. The mass flow rate is now given as a function of the exit area by

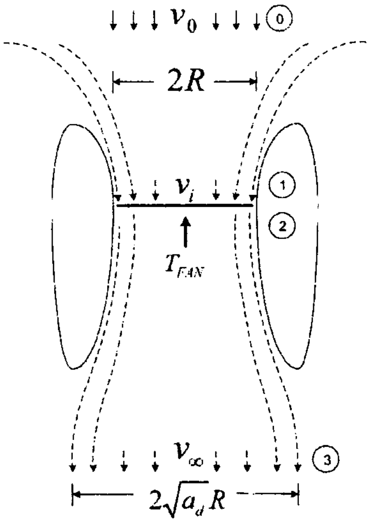

Figure 2.8: Single Propeller Ducted Fan

$$A_e = a_d A \tag{2.23}$$

$$\dot{m} = \rho A v_i = \rho a_d A v_e \tag{2.24}$$

$$v_i = a_d v_e \tag{2.25}$$

The total thrust is the sum of the propeller or fan thrust, and the force experienced by the duct

$$T = T_{FAN} + T_{DUCT} \tag{2.26}$$

The total system thrust is used to determine the acceleration of air in the slipstream for a hovering state ($v_o = 0$).

$$T = \dot{m}(v_e - v_o) = \dot{m} v_e \tag{2.27}$$

$$T = \rho a_d A v_e^2 = \rho \frac{A}{a_d} v_i^2 \tag{2.28}$$

$$v_i = \sqrt{\frac{T a_d}{\rho A}} \tag{2.29}$$

Applying Bernoulli's equation to regions 0 to 1, and 2 to 3,

$$p_o + \frac{1}{2}\rho v_o^2 = p_1 + \frac{1}{2}\rho v_i^2 \tag{2.30}$$

$$p_2 + \frac{1}{2}\rho v_i^2 = p_o + \frac{1}{2}\rho v_e^2 \tag{2.31}$$

an expression for the fan thrust is given by

$$T_{FAN} = (p_2 - p_1)A = \frac{1}{2}\rho v_e^2 A \tag{2.32}$$

$$\frac{T_{FAN}}{T} = \frac{1}{2a_d} \tag{2.33}$$

The above equations for the ducted fan are the same for the helicopter when $a_d = 0.5$. As shown in (2.33), increasing the wake area will increase the thrust experienced by the duct. For a given thrust, increasing the wake area lowers the required induced velocity. Since the required power at the propeller shaft is $P = Tv_i$, increasing the wake area lowers the power required to hover. Since this is an ideal case, the theory tends to exaggerate the contribution of thrust by the duct. There are physical limits to the extent of which the duct exit area can be increased to obtain additional thrust. A phenomena known as flow separation can occur due to excessive duct exit areas where the airflow does not conform to the surface of the duct which nullifies the duct induced effects.

2.2.3 Dual Rotor Ducted Fan

Consider Figure 2.9 which illustrates the dual propeller or coaxial ducted fan. A study performed in [2] showed that for a coaxial helicopter the distribution of thrust on the propellers was dependant on the ratio of the vertical separation of the rotors to the rotor diameter. This effect is worsened for the coaxial ducted fan since the duct further restricts the airflow to the lower rotor. To reflect the distribution of thrust, the thrust for the upper and lower rotors is given by T_1 and T_2, respectively. The total propeller thrust is then given by

$$T_{FAN} = T_1 + T_2 \tag{2.34}$$

Since both rotors have the same area, both the mass flow rate and airflow velocity must be equal for both rotors. The airflow velocity for both rotors is then given as the induced velocity. The thrust for each rotor contributes to the resulting induced velocity, even though there is no change in velocity from the top to bottom rotors. Therefore, the total fan thrust is given as the sum of the two individual rotor thrusts by

The mass flow rate for the duct is given in terms of the induced and exit velocity

$$\dot{m} = \rho A v_i = \rho a_d A v_e \tag{2.35}$$

$$v_i = a_d v_e \tag{2.36}$$

Applying Bernoulli's equation for regions 0 through 5, we obtain

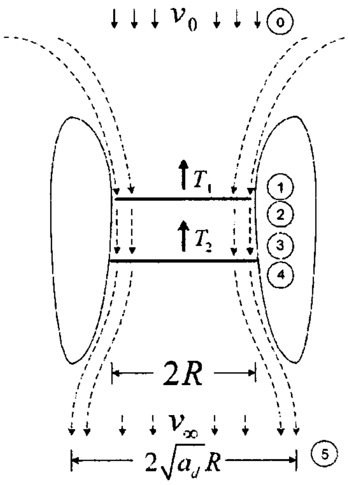

Figure 2.9: Coaxial Ducted Fan

$$p_o = p_1 + \frac{1}{2}v_i^2 \tag{2.37}$$

$$p_2 + \frac{1}{2}v_i^2 = p_3 + \frac{1}{2}v_i^2 \tag{2.38}$$

$$p_4 + \frac{1}{2}v_i^2 = p_o + \frac{1}{2}v_e^2 \tag{2.39}$$

The top and bottom rotor thrust, T_1 and T_2 are found using the pressure differences across regions 1 to 2, and 3 to 4, respectively,

$$T_1 = (p_2 - p_1)A \tag{2.40}$$

$$T_2 = (p_4 - p_3)A \tag{2.41}$$

From (2.38), since the velocity of the airflow between the rotors is the same, there is no change in pressure. As a result $p_2 = p_3$. To find the total rotor thrust T_1 and T_2 are combined given by

$$T_{FAN} = T_1 + T_2 \quad = \quad (p_2 - p_1 + p_4 - p_3)A \quad = \quad \frac{1}{2}\rho A v_e^2 \tag{2.42}$$

The result for the total rotor thrust for the coaxial ducted fan is the same as (2.32), which was obtained using a single propeller. Although this is an ideal case, this result suggests that the airflow through a coaxial ducted fan can be approximated by a single rotor with a total thrust T_{FAN}.

2.2.4 Vertical Climb and Descent

In [10] and [19], an analysis of a rotor is given when in a state of vertical climb or descent. During vertical climb or descent, the duct will experience airflow due to movement in addition to the induced velocity. During a climb, the airflow due to movement contributes to the induced velocity since both have a downward direction. During a descent, airflow due to movement flows upward which opposes the downward induced velocity. This creates a turbulent flow where momentum theory cannot be applied. This turbulent region exists until the rate of descent exceeds the exit wake velocity. For a propeller producing $10lbs$ of thrust with a rotor area of $0.1m^2$, the induced velocity is approximately $19m/s$. If the exit velocity is assumed to be equal to the induced velocity, or $A_e = A$, then this corresponds to a vertical descent of approximately $69km/hr$. Since the rate of descent will rarely intentionally be in excess of $69km/hr$, the system will always be in a state of turbulent airflow during descent. Regardless of airflow, the vertical acceleration of the system can be modeled using the current thrust. The difficulty exists for determining thrust in turbulent airflow. If the rate of descent is controlled to be negligible with respect to the induced velocity, then the turbulent flow is also negligible and the thrust is obtained as if in a state of hover.

During a vertical climb the main objective is to determine the net airflow through the duct to determine the aerodynamic forces applied to the control ailerons. To include the airflow due to vertical movement, v_o, the expression for the mass flow rate is modified as follows

$$\dot{m} = \rho A_e(v_e + v_o) = \rho A(v_i + v_o) \tag{2.43}$$

An expression for the total thrust, as a function of the mass flow rate and the overall acceleration of the airflow, is given by

$$T = \dot{m}(v_e + v_o) - \dot{m}v_o = \dot{m}v_e = \rho a_d A v_e^2 \tag{2.44}$$

The conclusion from the dual-rotor ducted fan model is that it can be approximated using a single-rotor model. Applying Bernoulli's equation for a single-rotor ducted fan in vertical climb we obtain

$$p_o + \frac{1}{2}\rho(v_o + v_i)^2 = p_1 + \frac{1}{2}\rho(v_o + v_i)^2 \tag{2.45}$$

$$p_2 + \frac{1}{2}\rho(v_o + v_i)^2 = p_o + \frac{1}{2}\rho(v_o + v_e)^2 \tag{2.46}$$

which leads to an expression for the rotor thrust which is given by

$$T_{FAN} = (p_2 - p_1)A = \frac{1}{2}\rho v_e(v_e + 2v_o)A \tag{2.47}$$

Comparison with (2.44) yields the ratio between the rotor thrust and the total thrust given by

$$\frac{T_{FAN}}{T} = \frac{1}{2a_d}\left(1 + \frac{2v_o}{v_e}\right) \tag{2.48}$$

For a state of hover, or $v_o = 0$, the result given by (2.48) is the same as previously given in (2.33). Despite this similarity, the new result is concerning since it does not have an upper bound which suggests the total thrust is less than the fan thrust, or the duct impedes high rates of climb. A solution for the induced velocity is found from (2.47) and (2.44) using the quadratic formula given by

$$v_i = -a_d v_o + \sqrt{a_d^2 v_o^2 + \frac{2a_d^2 T_{FAN}}{\rho A}} \tag{2.49}$$

since

$$v_e = \frac{v_i}{a_d} \tag{2.50}$$

The negative result is disregarded since the induced velocity must be positive. The given airflow over the control ailerons will be the sum of the induced velocity and the velocity due to the vertical climb. For a state of hover the expression given by (2.49) becomes

$$v_i(v_o = 0) = \sqrt{\frac{2a_d^2 T_{FAN}}{\rho A}} \tag{2.51}$$

Recall for a state of hover the ratio of the rotor thrust to the total thrust is given by .

$$\frac{T_{FAN}}{T} = \frac{1}{2a_d} \tag{2.52}$$

which leads to

$$v_i(v_o = 0) = \sqrt{\frac{Ta_d}{\rho A}} \tag{2.53}$$

The result given by (2.53) is the same as the previous result given by (2.29). This comparison is encouraging since (2.29) was obtained using momentum theory, where (2.53) was obtained using Bernoulli's equation. Despite the similarity, both results are mere approximations to the airflow within the duct since system losses are not modeled. Another source of error for Bernoulli's method is the assumption that the static pressure in the wake region is not affected by the wake velocity, although this approximation was also used by [10].

2.3 Aerodynamic Forces on an Airfoil

There are a number of methods which are commonly employed in the field of aerodynamic analysis, or more generally, fluid dynamics. In general, these methods mathematically describe the contour of a wing which establishes a boundary condition for differential equations describing a flow stream. One particular set of differential equations which can also describe fluid properties such as compressibility and viscosity is the *Navier-Stokes equations.* The Navier-Stokes equations are superior in their ability to model fluid dynamics, but are usually too difficult to solve analytically. The study of *computational fluid dynamics* involves the solution of complex differential equations by numerical methods. For analytical solutions, the difficulty involved in theory is usually overcome by making assumptions of the flow stream and on the airfoil. An assumption valid for flow streams moving at a velocity less than the speed of sound ($M < 1$), is that the flow is incompressible. For this case the resulting simplified equations are known as the *Euler Equations*. Further assumptions can be made involving the angle of attack for an airfoil. Two independent researchers, Joukowski and Kutta, worked at the beginning of the 20th century in the field of aerodynamics. Unaware of each others work, they both suggested that the lift on an airfoil can be modeled by a circulation of air around the airfoil. This method is now known as the *Kutta-Joukowski theorem*, and is an effective and relatively easy method for determining the lift on an airfoil for small angles of attack. Two useful references were used to formulate the proposed aerodynamic theory for flow over an airfoil (see Anderson [1] and Katz [8]). Anderson provides a clear and thorough development of aerodynamic theory where Katz is more abstract and involves more rigorous mathematics which can be used to prove some of the theorems listed above.

An application to classic aerodynamic theory is required to determine the force which will be exerted on the control ailerons. The Kutta-Joukowski theorem is given by

$$\frac{L}{b} = \rho v_\infty \Gamma \qquad \alpha << 1 \tag{2.54}$$

where v_∞ is the velocity of the flow stream, and Γ is the total circulation around the airfoil. This is only valid for small angles of attack, otherwise known as the small disturbance theorem. This theorem is usually applied to two-dimensional approximations which gives the lift per unit span, or L/b. A proof of the Kutta-Joukowski theorem is given by [8] using the small angle theorem ($\alpha << 1$) in addition to Bernoulli's equation.

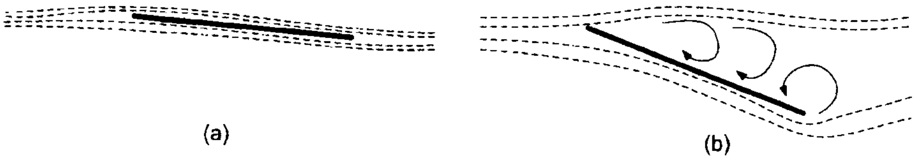

Figure 2.10: Thin Sheet Airfoil

Consider Figure 2.10 which shows a thin sheet immersed in a flow stream at small and large angle of attack. Figure 2.10(a) shows the airfoil at a very small angle of attack which results in a smooth laminar flow on the upper and lower surfaces of the sheet. Figure 2.10(b) shows the same airfoil at a larger angle of attack. As the angle of attack increases the air does not conform to the surface of the airfoil. This results in flow separation and turbulent flow on the upper surface of the airfoil. As a consequence the pressure distribution on the upper surface increases and lift deteriorates. This is known as airfoil stall and occurs at very low angles of attack due to the abrupt leading edge. For a thin sheet, vortices can begin to form well before the stall angle, α_{max}, which gradually increase until stall occurs.

The thin sheet is sometimes desired due to physical simplicity and the minimization of drag. Consider Figure 2.11 which illustrates a thin sheet airfoil versus a symmetric airfoil of similar chord and angle of attack. Since the symmetric airfoil does not have an abrupt leading edge the air is able to conform more to the curved surface than the thin sheet. The circulation Γ for airfoils is shown by the literature to be dependant on the camber line of the airfoil. Therefore, symmetric airfoils will generate the same amount of lift as a thin sheet. The drag for a symmetric airfoil is also suggested to be negligible for small angles of attack. The

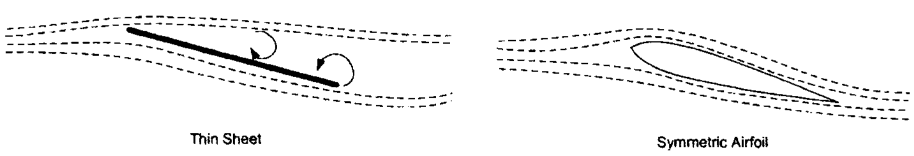

Figure 2.11: Thin Sheet versus Symmetric Airfoil

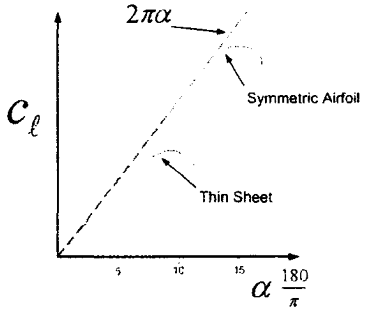

Figure 2.12: Lift Coefficient for Thin Sheet vs Symmetric Airfoil

superior airfoil then is the symmetric airfoil since it has a larger stall angle (see [1]). For a thin sheet, the stall gradually occurs but the stall angle is taken to be approximately $\alpha_{max} = 0.157rad\,(9^o)$. The stall for a symmetric airfoil occurs more abruptly which gives a more linear relationship between the angle of attack and the lift. The stall angle for a symmetric airfoil is approximately $\alpha_{max} = 0.262rad\,(15^o)$. There is an improvement of the range of angle of attack for the symmetric airfoil over the thin sheet by 67%. Figure 2.12 gives an example of lift coefficients for a thin and symmetric airfoil. This figure is used to demonstrate the discussed effects qualitatively and should not be used to obtain values for lift coefficients (for more detail see [1]).

For laminar or non-turbulent flow, the air velocity distribution on the surfaces of the wing can be modeled as a circulation of air, Γ. For turbulent flows, the circulation is disturbed and the Kutta-Joukowski theorem (2.54) does not hold. For non-turbulent flows, the circulation is given by

$$\Gamma = \pi\alpha c V_\infty \tag{2.55}$$

which is developed by the condition that the circulation must provide a vertical flow such that there is no normal component of the air velocity on the surface of the airfoil. Using (2.54), this results in a description of lift as a function of the span b and airfoil chord c, given by

$$L = \pi b c \rho V_\infty^2 \alpha \tag{2.56}$$

The lift coefficient for the case of a thin or symmetric airfoil at low angles of attack is given by

$$C_l = \frac{L}{\frac{1}{2}\rho A v^2} = 2\pi\alpha \tag{2.57}$$

where the *lift curve slope*, a, is given as the change in the lift coefficient with respect to the change in the angle of attack,

$$a = \frac{\partial C_l}{\partial \alpha} = 2\pi \tag{2.58}$$

This is an ideal case since the lift coefficient is affected by the airfoil Reynolds and Mach numbers. In [19] an experimentally obtained value of $a = 5.73$ is used to incorporate losses such as turbulent flow due to high Reynolds number. For high sub-sonic Mach numbers, the value of a can also increase.

The lift curve slope for cambered and symmetric airfoils are both equal to 2π. The difference of a cambered airfoil is that lift is produced at zero angle of attack as well as differences in the stall characteristics. If α_o is the attack angle at which the airfoil produces zero lift, then the lift coefficient is given by

$$C_l = a(\alpha - \alpha_o) \tag{2.59}$$

2.3.1 Flapped Airfoil

Although the symmetric airfoil has shown to be a dramatic improvement over the thin airfoil, it is still limited to a small range of angles of attack. Another type of airfoil which offers improvements to avoiding flow separation is the *flapped airfoil*. The circulation theory and the Kutta Joukowski theorem was applied to a flapped airfoil by Katz (see [8]). An example of a flapped airfoil is shown by Figure 2.13. The hinge point of the airfoil is located at a fraction of the airfoil chord, kc.

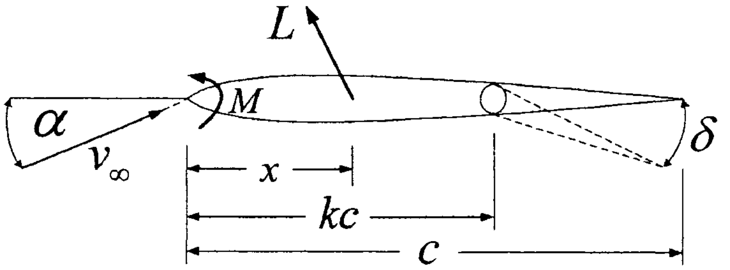

Figure 2.13: Flapped Airfoil

The angle of attack of the airfoil with respect to the direction of the airflow is α, and the flap angle is given by δ. Using this convention the lift and moment at the leading edge of the airfoil are given by

$$C_l = 2\pi\left(\alpha + \delta\left(1 - \frac{\theta_k}{\pi} + \frac{\sin\theta_k}{\pi}\right)\right) \tag{2.60}$$

$$C_m = \frac{\pi}{2}\left(\alpha + \delta\left(1 - \frac{\theta_k}{\pi}\right) + \frac{2\delta}{\pi}\sin\theta_k - \frac{\delta}{2\pi}\sin 2\theta_k\right) \tag{2.61}$$

respectively, where

$$\theta_k = \cos^{-1}(1-2k) \tag{2.62}$$

The aerodynamic center or center of pressure is not necessarily at the quarter chord position for a flapped airfoil. The point on the airfoil where no aerodynamic moment exists is given by x. This point is used to model the forces and torques applied to the system center of gravity, which is given by

$$x = \frac{C_m}{C_l} \tag{2.63}$$

Since it may not be physically feasible to perform both angles α and δ, the leading portion of the airfoil can be fixed at zero angle of attack or $\alpha = 0$. The new lift and moment coefficients are given by

$$C_l = 2\delta\left(\pi - \theta_k + \sin\theta_k\right) \tag{2.64}$$

$$C_m = \frac{\delta}{2}\left(\pi - \theta_k + 2\sin\theta_k - \frac{1}{2}\sin 2\theta_k\right) \tag{2.65}$$

which results in a fixed center of pressure given by

$$x = \frac{1}{4} + \frac{2\sin\theta_k - \sin 2\theta_k}{8\left(\pi - \theta_k + \sin\theta_k\right)} \tag{2.66}$$

The resulting lift located at the center of pressure is given as a percentage of the airfoil chord by

$$L = \frac{1}{2}C_l\rho bcv^2 \tag{2.67}$$

where b is the span of the airfoil, and v is the airflow velocity.

2.4 Rotor Blade Element Analysis

A method is shown in [10] and [19] which uses the results obtained from analysis of an airfoil at a low angle of attack can be applied to the rotor blades to determine the resulting thrust as a function of the rotor angular velocity ω. Consider Figure 2.14, which is not drawn to scale, that illustrates the geometry of the rotor blade in addition to the airflow across the blade.

The rotor blade is assumed to be rectangular in shape and has a blade pitch given by θ, chord c, and radius R. The *local* blade radius is given by r. The illustration shows there are two components to the airflow across the blade. These components are the local blade velocity, ωr, and the vertical velocity due to the induced velocity v_i and the vertical airflow due to vertical duct velocity, v_o. A dimensionless quantity which gives the total vertical airflow velocity with respect to the blade tip speed, or ωR, is called the *inflow ratio* and is given by

$$\lambda = \frac{v_i + v_o}{\omega R} \tag{2.68}$$

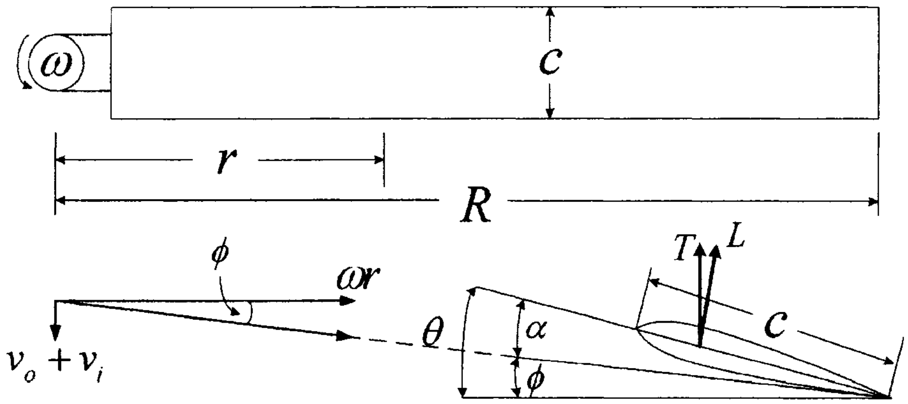

Figure 2.14: Airflow and Rotor Geometry

Since the airflow has a downward component, the angle of attack, α, is reduced by the angle ϕ,

$$\alpha = \theta - \phi \tag{2.69}$$

Since the rotor is required to spin at a very high velocity, an assumption is made that $\omega r >> v_i + v_o$, or $\phi << 1$, and

$$\tan\phi = \frac{v_i + v_o}{\omega r} \approx \phi \tag{2.70}$$

This is used to express the inflow ratio as a function of the angle ϕ which is given by

$$\lambda = \frac{v_i + v_o}{\omega r}\frac{r}{R} = \phi x \tag{2.71}$$

where x is the ratio of the local radius to the total radius

$$x = \frac{r}{R} \tag{2.72}$$

Since the angle ϕ is assumed to be small, the rotor thrust is then equal to the airfoil lift. Using the result given by (2.56), the incremental lift of a rotor blade is expressed as a function of the increment in rotor area by

$$dS = cdr \tag{2.73}$$

$$dL = \frac{1}{2}\rho C_l(\omega r)^2 dS = \frac{1}{2}\rho C_l(\omega r)^2 cdr \tag{2.74}$$

Since the lift is assumed to be collinear with the thrust, the change in the thrust coefficient is now given due to the change in lift by

$$dC_T = n\frac{dL}{\frac{1}{2}\rho A(\omega R)^2} = C_l\left(\frac{ncR}{A}\right)\left(\frac{r}{R}\right)^2\frac{dr}{R} \tag{2.75}$$

where n is the number of blades, and A is the total rotor disk area, or $A = \pi R^2$.

The *rotor solidity ratio*, σ, is the ratio of the actual blade area over the total rotor disk area

$$\sigma = \frac{ncR}{\pi R^2} \tag{2.76}$$

The thrust coefficient given by (2.75) is given using the rotor solidity ratio as well as the local radius ratio, x, by

$$dC_T = \sigma C_l x^2 dx \tag{2.77}$$

An expression for the lift coefficient, C_l, was previously given by (2.59). The local lift coefficient is dependant on the local angle of attack. The angle of attack depends on the local blade pitch, θ, and the inflow ratio, λ. Most rotor blades are twisted, or have a different value of pitch depending on the local radius. A linear approximation to the twist is given by

$$\theta = \theta_{75} + (x - 0.75)\theta_r \tag{2.78}$$

where θ_r is the constant linear rate of twist per unit rotor length, and θ_{75} is the value of the blade pitch at 75% of the total rotor radius. Assuming that the rotor blade is a symmetric or non-cambered airfoil, the local lift coefficient is then given by

$$C_l \;=\; a\alpha \;=\; a(\theta - \phi) \;=\; a(\theta_{75} + (x - 0.75)\theta_r - \frac{\lambda}{x} \tag{2.79}$$

which results in the incremental thrust coefficient given by

$$dC_T = \sigma a\left(\theta_{75} + (x - 0.75)\theta_r - \frac{\lambda}{x}\right)x^2 dx \tag{2.80}$$

The induced velocity v_i was previously assumed in momentum theory to be uniform over the entire disk area. There are methods suggested in the literature which attempt to model a non-uniform inflow ratio. For these models, the equation given by (2.80) are nonlinear which must be solved numerically for a specific rotor. To determine a general expression for thrust, a reasonable assumption is that the inflow ratio is constant, or the induced velocity is the same for every value of rotor radius. Since an increase in inflow ratio will decrease the angle of attack and thus decrease the thrust, this approximation is conservative since it under predicts the thrust coefficient. However, the assumptions on incompressible, irrotational, inviscid flow in addition to the assumption that the thrust and lift have the same direction tends to predict thrust values which are greater than actual values. These over predictions dominate over the under prediction for the inflow ratio. Assuming the inflow ratio is constant, the incremental thrust coefficient is integrated over the range of $0 < x < 1$ which further assumes that the rotor extends into the center of rotation. This results in a thrust coefficient of

$$C_T = \sigma a \left(\frac{\theta_{75}}{3} - \frac{\lambda}{2} \right) \tag{2.81}$$

This approximation is justified since the contribution to lift for values of radius near the center of rotation is negligible. The thrust is related to the thrust coefficient by (2.7). The thrust is then given as a function of the rotor angular velocity, ω by

$$T = \frac{1}{6} \sigma a \rho A R^2 \left(2\theta_{75} - 3 \left(\frac{v_i + v_o}{\omega R} \right) \right) \omega^2 \tag{2.82}$$

It is clear from (2.82) that the thrust is reduced during a climb ($v_o > 0$), and increased during descent ($v_o < 0$). Furthermore, for a given rotor velocity the degradation in thrust is proportional to the velocity v_o ($\Delta T \propto 1/\Delta v_o$). Equation (2.49) shows that the induced velocity is a function of v_o and T. Since there are different expressions for the induced velocity for conditions of climb and descent, it is difficult to obtain a general description of the thrust for all operating conditions. If the duct vertical velocity (with respect to the body frame) is negligible when compared to the induced velocity, a simplified version of the thrust can be obtained. For a system with $A = 0.1m^2$, $T_{FAN} = 44.5N$ (10lb), the induced velocity is $19.3m/s$ or $69km/h$. Assuming the duct vertical velocity is relatively small, or $v_i >> v_o$, the system can be assumed to be effectively in a hovering state where the induced velocity is given by

$$v_i = \sqrt{\frac{T a_d}{\rho A}} \tag{2.83}$$

The contribution by v_o is discarded resulting in the description of thrust by

$$T = 2\mu\theta_{75}\omega^2 - 3\mu\frac{\omega}{R}\sqrt{\frac{a_d}{\rho A}}\sqrt{T} \tag{2.84}$$

$$\mu = \frac{1}{6}\sigma a \rho A R^2 \tag{2.85}$$

where μ is a constant used for convenience. Since the result given by (2.84) is quadratic in form a solution for $\sqrt{T}$ is given by

$$\sqrt{T} = \left(-\frac{1}{2}\sqrt{\frac{9\mu^2 a_d}{R^2 \rho A}} + \frac{1}{2}\sqrt{\frac{9\mu^2 a_d}{R^2 \rho A} + 8\mu\theta_{75}} \right) \omega \tag{2.86}$$

where the negative result is discarded since the thrust must be positive. By squaring the above result we obtain

$$T = k_T \omega^2 \qquad v_o << v_i \tag{2.87}$$

$$k_T = \left(-\frac{1}{2}\sqrt{\frac{9\mu^2 a_d}{R^2 \rho A}} + \frac{1}{2}\sqrt{\frac{9\mu^2 a_d}{R^2 \rho A} + 8\mu\theta_{75}} \right)^2 \tag{2.88}$$

which shows the thrust to be proportional to the square of the angular velocity ω, by the proportionality constant k_T, given that the vertical climb or descent of the duct is negligible with respect to the induced velocity. This gives the thrust value of the rotor only, where the total thrust on the system is given by the rotor thrust and the duct thrust.

2.5 Power Analysis and Rotor Drag

The procedure used to determine the thrust as a function of the rotor speed ω can be applied to determine the total torque acting on the rotor. Since the thrust is not perfectly oriented in the desired direction of thrust, a small contribution of the thrust is also attributed to an additional drag force on the rotor known as *induced drag*, or the drag due to lift. A second source of drag is the *profile drag*, or frictional drag which is neglected in most of the theory thus far. The increment in rotor torque as a function of the change in lift, inflow angle ϕ, and change in frictional drag coefficient D_f, is given by

$$dQ = r(\phi dL + dD_f) \tag{2.89}$$

A more convienient analysis of the rotor torque is related to the rotor shaft power. In general, power is related to torque by

$$P = Q\omega \tag{2.90}$$

and the ideal power, P, is given by

$$P = Tv_i \tag{2.91}$$

which is the power predicted from ideal conditions. The ratio κ was previously suggested to account for the non-ideal characteristics or losses such as rotational turbulent flow, as well as to account for the assumptions required to determine the thrust. The power estimate which includes these losses is known as the *induced power* and is given by

$$P_i = \kappa P \tag{2.92}$$

where the literature suggests that κ can be assumed to have a value of 1.15 [19]. The frictional drag coefficient is often considered to be a constant or average value. In [10] an approximation to the frictional drag coefficient is suggested which is given by

$$C_d = 0.1166Re^{-0.2} \tag{2.93}$$

where Re refers to the Reynolds number at 3/4 of the radius. In [19] a frictional drag coefficient is given as a function of the average blade pitch by

$$C_d = \frac{D}{\frac{1}{2}\rho S(\omega R)^2} \tag{2.94}$$

The incremental drag coefficient is given as a function of the local radius r by

$$dD = \frac{1}{2}C_D\rho c(\omega r)^2dr \tag{2.95}$$

The resulting torque is then the product of the drag increment, the local radius, and the number of blades given by n

$$dQ = rndD = \frac{1}{2}C_D\rho nc\omega^2r^3dr \tag{2.96}$$

$$Q = \frac{1}{2}nC_D\rho c\omega^2\int_0^R r^3dr = n\frac{1}{8}C_D\rho cR^4\omega^2 \tag{2.97}$$

from which the profile power or the power consumed by drag is found in light of (2.90) by

$$P_o = \frac{1}{8}nC_D\rho cR^4\omega^3 \tag{2.98}$$

The total power, or power applied at the shaft, P_a, is given as the sum of the induced power and the profile power by

$$P_a = \kappa P + P_o \tag{2.99}$$

A measure of efficiency for helicopter type systems is known as the *figure of merit*, or FM, which is given by

$$FM = \frac{P}{\kappa P + P_o} \tag{2.100}$$

The resulting applied power coefficient, C_{P_a}, is then given as a function of the thrust coefficient by

$$C_P = \frac{P}{\frac{1}{2}\rho A(\omega R)^3} = \frac{Q/R}{\frac{1}{2}\rho A(\omega R)^2} = C_Q \tag{2.101}$$

An interesting characteristic is that the thrust coefficient is equal to the torque coefficient as shown by

$$C_{P_a} = \kappa\sqrt{\frac{a_d}{2}}C_T^{3/2} + \frac{1}{4}\sigma C_D \tag{2.102}$$

Having obtained a value for the frictional skin coefficient, the total resulting torque is given by

$$Q = \frac{1}{2}C_{D_f}\rho AR^3\omega^2 \tag{2.103}$$

Furthermore, the total applied power can be found and used to size an appropriate power plant for the system.

2.6 System Forces Due to External Airflow

In addition to the airflow induced velocity and velocity due to climb, external airflow can cause aerodynamic forces on the duct. This external airflow can be caused by motion of the aircraft or by wind. Consider Figure 2.15(a) which gives a general case of the system at an arbitrary orientation. The net effect of all external wind is given by the vector v_{ext}, which is taken with respect to the body-fixed frame. The external airflow can be separated into two vectors which are parallel and perpendicular to the body-fixed z axis, given by v_{xy} and v_z, respectively. The airflow component which is parallel to the body-fixed z axis is analogous to a vertical climb in a hover state. The resulting airflow through the duct due to the induced velocity and v_z can be modeled as discussed previously in the section on vertical flight.

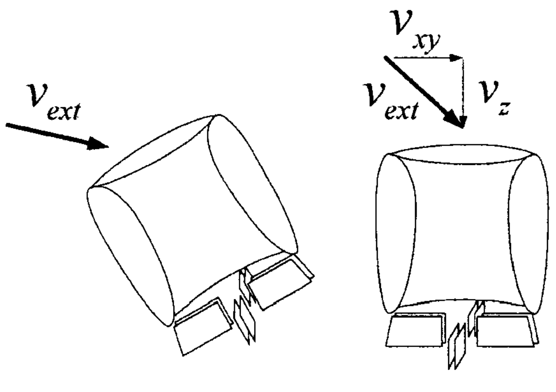

Figure 2.15: External Airflow

The perpendicular component, namely v_{xy} produces a resulting force in addition to the moment τ_{xy}. The force F_{xy} is not caused by traditional lifting theory, rather is caused by friction between the airflow and the duct. If the force F_{xy} is known then the orientation of the aircraft can be used to determine the corresponding lift and drag as illustrated in figure 2.15(b).

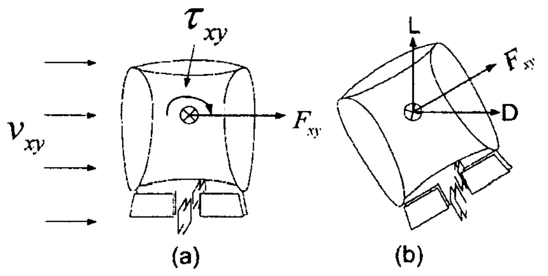

Figure 2.16: Airflow Normal to System

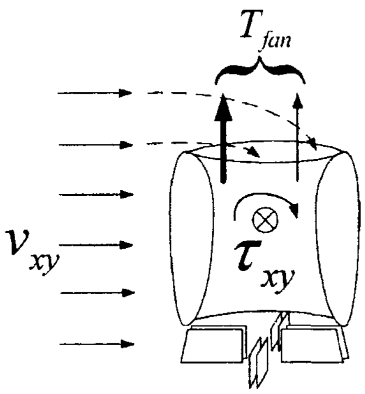

Figure 2.17: Non-uniform Thrust Distribution Due to Airflow

The moment τ_{xy} is caused mostly by the non-uniform distribution of airflow through the duct but can also be caused by the control ailerons acting as a lever arm. The principal cause of this torque was previously studied (see [4]). When there is airflow normal to the duct opening, more air is directed into the rotor on the downwind side of the duct. This creates a non-uniform thrust distribution on the rotor which produces the moment τ_{xy}. If the airflow is a result of aircraft velocity, this torque will tend to counteract the angle of attack used for forward flight. As the aircraft velocity increases the torque also increases which creates the tendency for the duct to rotate back toward the hovering state. If the airflow is due to wind, then the torque will cause the duct to rotate such that the thrust is directed down-wind. This results in both the wind and the duct angle of attack contributing to the forward motion of the duct.

2.6.1 Modeling of External Forces

Aerodynamic analysis of the force F_{xy} due to the airflow over the duct, nose, and tail of the system would be very complex due to the physical geometry. This force can be approximated by assuming that most of the drag is due to the large duct surface area which can be further approximated as an airflow over a cylinder. Experimental research of drag coefficients is given in [1] for a cylinder as a function of the Reynolds number (see [1] pg. 257). The result of this research is that the drag coefficient of a cylinder is approximately equal to 1.2 for a range of Reynolds number from 100 to 2.5×10^5. For an outer duct diameter of 19 inches ($d = 0.4826m$), the Reynolds number is more specifically given by (2.104), which limits the normal airflow velocity to $8m/s$, or $29km/h$. After this velocity there is a significant *decrease* in the drag coefficient of a cylinder. The drag coefficient is given with respect to the *projected* surface area, or the product of the duct chord, c_{duct}, and the duct diameter, d. Using this approximate model the force on the duct is given by (2.106). The direction of the force is in the opposite direction as the perpendicular airflow v_{xy}.

$$Re = \frac{\rho d}{\mu} v = 31232v \tag{2.104}$$

$$C_D = \frac{D}{\frac{1}{2}\rho A v^2} \approx 1.2 \qquad 0 < v < 8m/s \tag{2.105}$$

$$F_{xy} = \frac{1}{2} \rho \, c_{duct} \, d \, C_d \, v^2 \tag{2.106}$$

Chapter 3

Aircraft Attitude Representation

When describing the motion of the aircraft, or more generally any body of mass, the translational motion as well as the rotational motion must be defined. The objective of this chapter is to review the required mathematical background to describe the rotational motion of a rigid body. The study of attitude representation is common in texts dealing with robotics (for example see [6], [14], and [23]). A paper which deals exclusively with attitude representation is given by Shuster [21], which the majority of the work in this chapter is based on.

In order to describe a single rotation, two frames of reference are used. When describing the attitude of a moving rigid body, these two frames are often referred to as the inertial frame and the body-fixed frame. The inertial frame of reference does not move, and is considered to be a set of axes positioned at the aircraft point of origin rigidly attached to the earth. A second set of axes is rigidly attached to the aircraft center of mass which defines the body-fixed frame. The orientation of the aircraft is then described by the difference between the inertial and body-fixed frames.

3.1 The Direct Cosine Matrix

A common method used to describe rotations between two frames of reference is the direct cosine matrix (DCM), which is also often referred to as a rotation matrix. To demonstrate how a rotation matrix is determined consider the case shown in Figure (3.1) which illustrates a rotation about the z axis.

$$\begin{aligned} \hat{x}_b &= \cos\theta\hat{x} + \sin\theta\hat{y} \\ \hat{y}_b &= -\sin\theta\hat{x} + \cos\theta\hat{y} \\ \hat{z}_b &= \hat{z} \end{aligned} \tag{3.1}$$

The illustration shown in Figure (3.1) in addition to (3.1) describe the transformation of a set of axes $\begin{pmatrix} \hat{x} & \hat{y} & \hat{z} \end{pmatrix}$ to a second set of axes $\begin{pmatrix} \hat{x}_b & \hat{y}_b & \hat{z}_b \end{pmatrix}$. The equations given in (3.1) can be expressed in matrix form.

$$\begin{pmatrix} \hat{x}_b \\ \hat{y}_b \\ \hat{z}_b \end{pmatrix} = \begin{pmatrix} \cos\theta & \sin\theta & 0 \\ -\sin\theta & \cos\theta & 0 \\ 0 & 0 & 1 \end{pmatrix} \begin{pmatrix} \hat{x} \\ \hat{y} \\ \hat{z} \end{pmatrix} \tag{3.2}$$

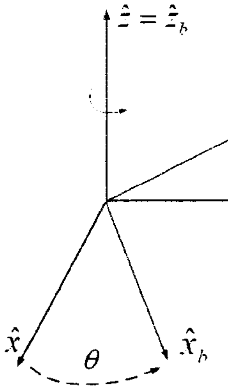

Figure 3.1: Rotation about the z axis

At this point, it is necessary to introduce notation for the direct cosine matrix.[1] Since rotation matrices describe a transformation between different frames, it is often useful to identify the original frame and the resulting frame.

$$\begin{array}{r} \textbf{resulting frame} \\ \textbf{origin frame} \end{array} \Uparrow {}^{b}_{o}R$$

We can obtain the direct cosine matrix representing a rotation about the $\hat{z}$ axis by an angle θ, which is given in (3.5). Similar arguments can be made for rotations about the $\hat{x}$ and $\hat{y}$ axis which yield the direct cosine matrices given in (3.3) and (3.4), respectively. Note that rotations can also occur on any axis, and not just on the orthogonal axes described here.

$$ {}^{b}_{o}R(\hat{x},\theta) = \begin{pmatrix} 1 & 0 & 0 \\ 0 & \cos\theta & \sin\theta \\ 0 & -\sin\theta & \cos\theta \end{pmatrix} \tag{3.3}$$

$$ {}^{b}_{o}R(\hat{y},\theta) = \begin{pmatrix} \cos\theta & 0 & -\sin\theta \\ 0 & 1 & 0 \\ \sin\theta & 0 & \cos\theta \end{pmatrix} \tag{3.4}$$

$$ {}^{b}_{o}R(\hat{z},\theta) = \begin{pmatrix} \cos\theta & \sin\theta & 0 \\ -\sin\theta & \cos\theta & 0 \\ 0 & 0 & 1 \end{pmatrix} \tag{3.5}$$

In general, any vector which is given with respect to one set of axes, can be found as a function of a second set of axes. The direct cosine matrix can be used to describe the transformation of a vector as shown by

$$u_B = {}^{B}_{A}R \; u_A \tag{3.6}$$

---

[1] Different conventions for rotations are often found depending on the author. This often creates some discrepancies between works especially with the relationship between R and R^T. Throughout this thesis, these differences will be addressed and care will be exercised to be specific as to which form is utilized.

For any rotation, if we take two arbitrary set of axes where frame $\{a\}$ is given with respect to the axes $(\ \hat{x}_a \quad \hat{y}_a \quad \hat{z}_a\ )$ and frame $\{b\}$ is given with respect to the axes $(\ \hat{x}_b \quad \hat{y}_b \quad \hat{z}_b\ )$, then the rotation matrix which describes the transformation from frame $\{a\}$ to frame $\{b\}$ is given by

$$^{b}_{a}R = (\ x' \quad y' \quad z'\ ) \tag{3.7}$$

where x', y', and z' are unit vectors which satisfy:

x': The coordinates of the axis $\hat{x}_a$ expressed in frame $\{b\}$.
y': The coordinates of the axis $\hat{y}_a$ expressed in frame $\{b\}$.
z': The coordinates of the axis $\hat{z}_a$ expressed in frame $\{b\}$.

Mathematically, this can be expressed as dot products of the unit vectors.

$$x' = \begin{pmatrix} \hat{x}_a \cdot \hat{x}_b \\ \hat{x}_a \cdot \hat{y}_b \\ \hat{x}_a \cdot \hat{z}_b \end{pmatrix} \qquad y' = \begin{pmatrix} \hat{y}_a \cdot \hat{x}_b \\ \hat{y}_a \cdot \hat{y}_b \\ \hat{y}_a \cdot \hat{z}_b \end{pmatrix} \qquad z' = \begin{pmatrix} \hat{z}_a \cdot \hat{x}_b \\ \hat{z}_a \cdot \hat{y}_b \\ \hat{z}_a \cdot \hat{z}_b \end{pmatrix} \tag{3.8}$$

Due to the relationship between a rotation matrix and an orthogonal set of axes in Euclidean space, it is included in a special family of matrices, or $\mathbb{R} \in SO(3)$, which is known as the special set of linear orthogonal equations in 3 dimensions. Due to the nature of this set, the rotation matrix has some unique properties.

$$\|R\| = 1 \tag{3.9}$$

$$R^{-1} = R^T \quad \Rightarrow \quad RR^T = R^T R = I \tag{3.10}$$

In terms of a transformation between frames:

$$^{B}_{A}R^T = {}^{B}_{A}R^{-1} = {}^{A}_{B}R \tag{3.11}$$

If any two rotation matrices, or matrices belonging to $SO(3)$, are multiplied, the product will also be a rotation matrix belonging to $SO(3)$. Consider the special case where the rotation matrix R is multiplied by its inverse, or transpose, resulting in the identity matrix, I. The identity matrix must then be a rotation matrix belonging to the set $SO(3)$. The identity matrix is a rotation matrix which describes a null rotation, or when two frames of reference are coincident.

Since rotation matrices must be orthogonal, problems can arise when using inertial sensors or in computer simulations where the obtained rotation matrix contains errors. These errors can be a result of noise, misalignment of sensors, or accumulative computational errors. Under these circumstances the obtained rotation matrix may not be perfectly orthogonal. The Gram-Schmidt Orthornormalization algorithm, which is discussed in [16], is an extension of the Gram-Schmidt Orthogonalization algorithm, that modifies a set of vectors to be perfectly orthogonal with respect to each other. In the case of the orthonormalization version of the algorithm, each vector is also modified to be of unit length.

3.2 Compositions of Rotation Matrices

There may be cases where an orientation may be described by multiple rotations. In physical systems, such as aircraft, the orientation of a frame of reference is also often represented using a composition of three rotations known as Euler angles. Since rotation matrices lack a commutative property, the order of matrix multiplication is important and is addressed here.

3.2.1 Rotations Referenced to Current Frames

Let R_1 denote a direct cosine matrix which gives the transformation **from** frame {A} **to** frame {B}. If an arbitrary vector exists in frame {A} with coordinates given by v_A, then the coordinates of this vector in frame {B}, or v_B is given by:

$$R_1 = {}^{B}_{A}R \tag{3.12}$$

$$v_B = R_1 \; v_A \tag{3.13}$$

In addition, let R_2 denote a rotation **from** frame {B}, or the current frame, **to** frame {C}.

$$R_2 = {}^{C}_{B}R \tag{3.14}$$

$$v_C = R_2 \; v_B \tag{3.15}$$

By simple substitution we can obtain a transformation directly from frame {A} to frame {C}. Note the order of the matrix multiplication. The transformation which occurred second, namely R_2, precedes the first rotation in the order of multiplication.

$$v_C \;=\; R_2 \; R_1 \; v_A \tag{3.16}$$

$$\begin{tikzcd}
\{A\} \arrow[r] & R_1 \arrow[r] & \{B\} \arrow[r] & R_2 \arrow[r] & \{C\}
\end{tikzcd}$$

$\longleftarrow$ Order of multiplication

Figure 3.2: Transformation from {A} to {C}

3.2.2 Rotations Referenced to Fixed Frames

The fixed frame of reference is usually the inertial frame. For this example frame {A} will be taken as the inertial frame. As in the previous example, let R_1 denote a rotation which gives the transformation from frame {A} to frame {B}.

$$R_1 = {}^{B}_{A}R \tag{3.17}$$

$$v_B = R_1 \; v_A \tag{3.18}$$

Let R_2 denote a rotation with respect to the **fixed** frame. After the first rotation the current frame of reference is frame {B}. The rotation R_2 cannot be used to rotate {B} to {C} since the rotation axis exists in frame {A} and is not defined in {B}. In order to rotate frame {B} we must temporarily rotate back to frame {A}, perform the rotation R_2, and then redo the temporary rotation. Consider the following diagram:

$$\{B\} \longrightarrow R_1^{-1} \longrightarrow \{A\} \longrightarrow R_2 \longrightarrow R_1 \longrightarrow \{C\}$$

$$\longleftarrow \text{ Order of multiplication}$$

Figure 3.3: Transformation from {B} to {C}

$$v_C = R_1 \; R_2 \; R_1^{-1} \; v_B \tag{3.19}$$

Using simple substitution the rotation from frame {A} to frame {C} is obtained. The matrices R_1 and R_1^{-1} combine resulting in the identity matrix. The result of the above transformation is the order of multiplication of the rotation matrices is the same as the order of occurrence.

$$v_C \;=\; R_1 \; R_2 \; R_1^{-1} \; R_1 \; v_A \;=\; R_1 \; R_2 \; v_A \tag{3.20}$$

Although the order of rotations is different for current and fixed frames, the figures (3.2) and (3.3) show that the order does not change. It is only through the cancelation of R_1 and R_1^{-1} which effectively reverses the order of multiplication.

3.3 Relationship Between the DCM and Vector of Rotation

The concept of a rotation can be considered to consist of a vector of rotation and an angle by which the vector is rotated. The vector can be thought to be rigidly attached to a body-fixed set of axes which is rotated with the vector. Figure (3.4) is an example of how the rotation of a set of axes is given using a vector and angle of rotation. This description of a rotation requires only four terms which is an improvement over the direct cosine matrix. Another form of representing rotations which uses only 4 terms is known as the quaternion and is the topic of interest in later sections.

Consider the direct cosine matrix which describes a rotation about the $\hat{x}$ axis, which was given in (3.3). A method was proposed in [21] which describes the rotation matrix using a arbitrary vector of rotation.

$${}^{b}_{o}R(\hat{x}, \theta) = \begin{pmatrix} 1 & 0 & 0 \\ 0 & \cos\theta & \sin\theta \\ 0 & -\sin\theta & \cos\theta \end{pmatrix} \tag{3.21}$$

To determine how a vector is transformed, or expressed in a different coordinate system, the direct cosine matrix is multiplied by a vector. The result is the vector expressed in the new coordinate system. Consider the matrix product of the direct cosine matrix and the three unit vectors

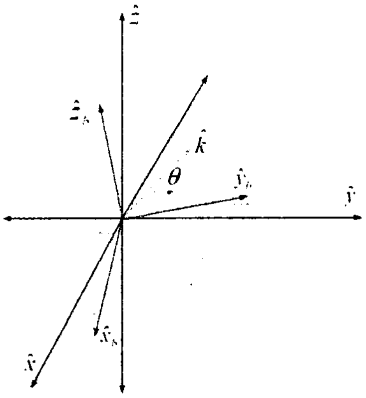

Figure 3.4: Rotation about vector $\hat{k}$ by an angle of θ

$$ {}^b_oR(\hat{x},\theta)\hat{x} = \hat{x} \tag{3.22}$$

$$ {}^b_oR(\hat{x},\theta)\hat{y} = \cos\theta\hat{y} - \sin\theta\hat{z} = \cos\theta\hat{y} - \sin\theta\,(\hat{x}\times\hat{y}) \tag{3.23}$$

$$ {}^b_oR(\hat{x},\theta)\hat{z} = \sin\theta\hat{y} + \cos\theta\hat{z} = \cos\theta\hat{z} - \sin\theta\,(\hat{x}\times\hat{z}) \tag{3.24}$$

Since the vector $\hat{x}$ is parallel to the axis of rotation it remains unchanged. Since the objective is to find the result for an arbitrary vector, it must be decomposed into parallel and perpendicular components taken with respect to any axis of rotation

$$ v = v_\perp(\hat{k}) + v_\parallel(\hat{k}) \tag{3.25}$$

$$ v_\parallel(\hat{k}) = \frac{\left(\hat{k}\cdot v\right)\hat{k}}{\|\hat{k}\|^2} = \frac{\hat{k}\hat{k}^T v}{\|\hat{k}\|^2} \tag{3.26}$$

$$ v_\perp(\hat{k}) = \frac{-\hat{k}\times\left(\hat{k}\times v\right)}{\|\hat{k}\|^2} = \frac{-S(\hat{k})^2 v}{\|\hat{k}\|^2} \tag{3.27}$$

Using the pattern observed by (3.22) through (3.24), a more general result for the transformation of a vector is given by

$$ {}^b_oR(\hat{k},\theta)v = v_\parallel + \cos\theta v_\perp - \sin\theta\left(\hat{k}\times v_\perp\right) \tag{3.28}$$

where $\hat{k}$ is the vector of rotation. Using (3.26) and (3.27) and assuming that the vector of rotation is a unit vector ($\|\hat{k}\|^2 = 1$) leads to:

$$ {}_o^bR(\hat{k},\theta)v = \hat{k}\hat{k}^T v - \cos\theta\, S(\hat{k})^2 v + \sin\theta\, S(\hat{k})^3 v \tag{3.29}$$

Since the term v is found in every term it can be removed resulting in a relation between the direct cosine matrix and the vector of rotation. This result is further simplified in light of (C.7) and (C.8) to obtain

$$ {}_o^bR(\hat{k},\theta) = I + (1-\cos\theta)S(\hat{k})^2 - \sin\theta\, S(\hat{k}) \tag{3.30}$$

3.4 The Quaternion

In general, a quaternion has the form given in (3.31), where p_o is the quaternion scalar, and p is the quaternion vector.

$$P = \begin{pmatrix} p_o \\ p \end{pmatrix} \qquad P \in \mathbb{R}^4 \quad p_o \in \mathbb{R} \quad p \in \mathbb{R}^3 \tag{3.31}$$

A description of the quaternion in terms of the set of imaginary quantities given by **i**, **j**, and **k** is given by [21] and [14]

$$P = p_o + p_1\mathbf{i} + p_2\mathbf{j} + p_3\mathbf{k} \qquad p_i \in \mathbb{R} \quad i = 0, ...3, \tag{3.32}$$

A special form of multiplication is used within this set of imaginary quantities, otherwise known as quaternion multiplication, which is defined by the '$\odot$' operator. Equations (3.33) through (3.37) give some basic fundamental properties of quaternion multiplication. Although quaternion multiplication is based on these properties, they are seldom required since the following operations can also be described using more common operations such as the dot and cross product.

$$a \odot \mathbf{h} = \mathbf{h} \odot a = a\mathbf{h} = \mathbf{h}a \qquad a \in \mathbb{R} \qquad \mathbf{h} = \mathbf{i}, \mathbf{j}, \mathbf{k} \tag{3.33}$$

$$\mathbf{h} \odot \mathbf{h} = -1 \qquad \mathbf{h} = \mathbf{i}, \mathbf{j}, \mathbf{k} \tag{3.34}$$

$$\mathbf{i} \odot \mathbf{j} = -\mathbf{j} \odot \mathbf{i} = \mathbf{k} \tag{3.35}$$

$$\mathbf{j} \odot \mathbf{k} = -\mathbf{k} \odot \mathbf{j} = \mathbf{i} \tag{3.36}$$

$$\mathbf{k} \odot \mathbf{i} = -\mathbf{i} \odot \mathbf{k} = \mathbf{j} \tag{3.37}$$

3.4.1 The Euler-Rodrigues Symmetric Parameters

A special family or subset of the quaternion commonly used to represent rotations is known as the Euler-Rodrigues symmetric parameters. Denoted by 'Q', the Euler-Rodrigues symmetric parameters utilizes a sine and cosine term and has a normalization constraint as shown by

$$ {}^{b}_{o}Q = \begin{pmatrix} q_o \\ q \end{pmatrix} = \begin{pmatrix} \cos(\theta/2) \\ \sin(\theta/2)\,\hat{k} \end{pmatrix} \quad Q \in \mathbb{R} \times \mathbb{R}^3 \quad |Q| = 1 \tag{3.38} $$

$$ q_o^2 + q^T q = 1 \tag{3.39} $$

where $\hat{k}$ denotes a unit vector in Euclidean space which is rotated by the angle θ. Using the new convention the relationship between the quaternion and the direct cosine matrix previously given by (3.30) is found as a function of the Euler-Rodrigues symmetric parameters. A transformation from the rotation matrix to the quaternion is also shown by (3.41), where the scalar component can be found from the normalization constraint of the quaternion.

$$ {}^{b}_{o}R(\hat{k},\theta) = I + 2S(q)^2 - 2q_o S(q) \tag{3.40} $$

$$ S(q) = \frac{1}{2\sqrt{1+\mathrm{trace}(R)}}(R^T - R) \tag{3.41} $$

Other expressions describing the relationship between the quaternion and the direct cosine matrix exist, for example (3.43). This expression is valid yet it is important to realize that for this form, the direct cosine matrix represents a rotation from frame $\{b\}$ to frame $\{o\}$, where the quaternion represents the opposite rotation which is from frame $\{o\}$ to frame $\{b\}$.

$$ {}^{b}_{o}Q = \begin{pmatrix} q_o \\ q \end{pmatrix} \tag{3.42} $$

$$ {}^{o}_{b}R(\hat{k},\theta) = {}^{b}_{o}R(\hat{k},\theta)^T = I + 2S(q)^2 + 2q_o S(q) \tag{3.43} $$

3.4.2 Negated Euler-Rodrigues Parameter

Negating the Euler-Rodrigues symmetric parameters is equivalent to increasing the angle of rotation by a value of 2π. When used to describe rotations, negating the quaternion has no effect and is effectively the same as the non-negated quaternion. This result is characteristic of the special subset, and does not apply for all quaternion.

$$ -Q = \begin{pmatrix} -q_o \\ -q \end{pmatrix} = \begin{pmatrix} -\cos(\theta/2) \\ -\sin(\theta/2)\,\hat{k} \end{pmatrix} = \begin{pmatrix} \cos((\theta+2\pi)/2) \\ \sin((\theta+2\pi)/2)\,\hat{k} \end{pmatrix} \tag{3.44} $$

$$ Q \sim -Q \tag{3.45} $$

3.4.3 Quaternion Multiplication

Quaternion multiplication can be used to combine two or more quaternions, particularly in the case where two or more rotations are used to describe the overall orientation of a moving body. Quaternion multiplication is also required to transform the coordinates of a vector from frame to frame. Rotation matrices are also multiplied by other matrices or vectors to perform these operations. Quaternion multiplication is much different than the linear algebra employed to multiply rotation matrices. One property that rotation matrix multiplication and quaternion multiplication share is the lack of a commutative property. Using the fundamental properties of the quaternion multiplication given by equations (3.33) through (3.37), a more practical description of the quaternion multiplication can be derived. For purposes of describing the quaternion multiplication, let both Q and P belong to the set of all quaternion

$$Q = \begin{pmatrix} q_o \\ q \end{pmatrix} \qquad P = \begin{pmatrix} p_o \\ p \end{pmatrix} \qquad Q, P \in \mathbb{R}^4 \tag{3.46}$$

where the quaternion product of these two quaternion is defined as

$$K = Q \odot P = (q_o + q_1\mathbf{i} + q_2\mathbf{j} + q_3\mathbf{k}) \odot (p_o + p_1\mathbf{i} + p_2\mathbf{j} + p_3\mathbf{k}) = \begin{pmatrix} k_o \\ k \end{pmatrix} \tag{3.47}$$

Since quaternion multiplication has associative and distributive properties the above operations can be performed term by term. To obtain a result for the quaternion multiplication the problem is separated into scalar terms, and vector terms. scalar terms will result from the product of the two quaternion scalars, and also when 2 similar imaginary terms are multiplied resulting in -1.

Scalar part:

$$k_o = q_o p_o - q_1 p_1 - q_2 p_2 - q_3 p_3 \quad = \quad q_o p_o - q^T p$$

Vector part:

$$k = q_o p + p_o q + (q_2 p_3 - q_3 p_2)\mathbf{i} + (q_3 p_1 - q_1 p_3)\mathbf{j} + (q_1 p_2 - q_2 p_1)\mathbf{k} = q_o p + p_o q + q \times p$$

Using the results obtained for the scalar and vector products of the quaternion multiplication, a more practical form is given by

$$Q \odot P = \begin{pmatrix} q_o p_o - \bar{q} \cdot p \\ q_o p + p_o q + q \times p \end{pmatrix} \tag{3.48}$$

Another form of quaternion multiplication is also commonly used and is given by

$$Q \otimes P = \begin{pmatrix} q_o p_o - q \cdot p \\ q_o p + p_o q - q \times p \end{pmatrix} \tag{3.49}$$

where the cross product is given as a negative term. The relationship between these two forms of quaternion multiplication is solely dependant on the order of multiplication

$$P \otimes Q = Q \odot P \tag{3.50}$$

which is the reason the quaternion violates the commutative property. Although the quaternion multiplication does not have a commutative property, it does have associative and distributive properties. The associative and distributive properties exist for all quaternion including the unit quaternion subset.

$$P \otimes (Q \otimes R) = (P \otimes Q) \otimes R = R \odot Q \odot P \qquad \forall P, Q, R \in \mathbb{R}^4 \tag{3.51}$$

$$P \otimes (Q + R) = P \otimes Q + P \otimes R = Q \odot P + R \odot P \qquad \forall P, Q, R \in \mathbb{R}^4 \tag{3.52}$$

The quaternion multiplication given by (3.48) is also equivalent to the form

$$Q \odot P \;=\; E(Q)\, P \tag{3.53}$$

where

$$E(Q) \;=\; \begin{pmatrix} q_o & -q^T \\ q & q_o I + S(q) \end{pmatrix} \qquad E \in \mathbb{R}^{4\times 4} \tag{3.54}$$

3.4.4 The Identity Quaternion

The identity quaternion, denoted by Q_I, is given by

$$Q_I = \begin{pmatrix} 1 \\ \mathbf{0} \end{pmatrix} \tag{3.55}$$

$$P \otimes Q_I = P \odot Q_I = P \qquad \forall P \in \mathbb{R}^4 \tag{3.56}$$

is analogous to the identity matrix in linear algebra, in the sense that it represents a null rotation. In reference to the Euler-Rodrigues symmetric parameters, the identity quaternion exists when two frames of reference are coincident in orientation. The identity quaternion can be observed as a rotation by $\theta = 0$ about an arbitrary vector $\hat{k}$, as shown by

$$Q_I = \begin{pmatrix} \cos(0) \\ \sin(0)\, \hat{k} \end{pmatrix} = \begin{pmatrix} 1 \\ \mathbf{0} \end{pmatrix} \tag{3.57}$$

3.4.5 Quaternion Inverse

The quaternion conjugate given by

$$P^\star = \begin{pmatrix} p_o \\ -p \end{pmatrix} \tag{3.58}$$

is used to obtain the quaternion inverse by

$$P^{-1} = \frac{P^\star}{\|P\|^2} = \frac{1}{\|P\|^2} \begin{pmatrix} p_o \\ -p \end{pmatrix} \tag{3.59}$$

where P belongs to the set of all quaternion. The result of the quaternion multiplication of any quaternion and its inverse is the identity quaternion Q_I, as shown by

$$P \otimes P^{-1} = P \odot P^{-1} = Q_I \tag{3.60}$$

In reference to the Euler-Rodrigues Symmetric Parameters, an operation for the inverse quaternion can be considered as a rotation of the vector $\hat{k}$ by the negated angle, or $-\theta$. Similarly, the inverse quaternion can be considered as the rotation of the negated vector, $-\hat{k}$, by the angle θ. Also, if a quaternion represents the rotation from frame {A} to frame {B}, then the inverse will represent the opposite rotation, or from frame {B} to frame {A}.

$${}^{B}_{A}Q^{-1} = {}^{A}_{B}Q \tag{3.61}$$

$$Q^{-1} = \begin{pmatrix} \cos(-\theta/2) \\ \sin(-\theta/2)\,\hat{k} \end{pmatrix} = \begin{pmatrix} q_o \\ -q \end{pmatrix} \tag{3.62}$$

3.4.6 Vector Transformation

In a system containing multiple frames of reference it is useful to be able to transform the coordinates of a given vector from frame to frame. Using rotation matrices, a transformed vector is easily obtained by the matrix product of the rotation matrix and the vector. If quaternion are used to represent orientation then vector transformation can be achieved by quaternion multiplication. Let ${}^{B}_{A}Q$ and ${}^{B}_{A}R$ represent the quaternion and direct cosine matrix, respectively, which describe the rotation from frame {A} to frame {B}. The objective is to transform the coordinates of a vector expressed in frame {A}, v_A, to be expressed in frame {B}. To perform this operation using quaternion multiplication, the vector is expressed as a quaternion with a zero angle of rotation. In general, a vector truncated with an extra preceding zero is denoted by Q_u as shown by

$$Q_u = \begin{pmatrix} 0 \\ u \end{pmatrix} \tag{3.63}$$

The transformed vector can be expressed using the direct cosine matrix

$$Q_{v_B} = \begin{pmatrix} 0 \\ v_B \end{pmatrix} = \begin{pmatrix} 0 \\ {}^{B}_{A}R\,v_A \end{pmatrix} \tag{3.64}$$

or equivalently, using quaternion multiplication

$$Q_{v_B} = {}^{B}_{A}P \otimes Q_{v_A} \otimes {}^{B}_{A}P^{-1} \qquad \forall P \in \{P = (p_o,\ p) \quad |p_o^2 + p^T p = 1\} \tag{3.65}$$

3.5 Compositions of Multiple Quaternion

The rotation or orientation of a body can be given as a set of multiple rotations, for example Euler angles. Multiple quaternion may also be required in systems with multiple frames of reference. Similar to the theory of multiple rotation matrices, this section describes how multiple quaternion can be combined to represent the overall orientation of a body. Since rotations can be defined as referenced to a current or fixed frame, these methods are addressed separately. For the purposes of describing rotations, the term quaternion is now used to describe the Euler-Rodrigues Symmetric Parameters.

3.5.1 Rotations referenced to current frames

Creating three frames of reference, frame {A}, {B}, and {C}, let the following quaternions represent the transformation between these frames. The rotations occur in order, where Q_1 represents the rotation from frame {A} to frame {B}, followed by the rotation Q_2 which represents the rotation from the current frame {B} to the final frame {C}.

$$Q_1 = {}^B_A Q \qquad Q_2 = {}^C_B Q \tag{3.66}$$

The quaternion which describes the overall rotation from frame {A} to frame {C} is a function of quaternion multiplication given by

$${}^C_A Q = Q_2 \otimes Q_1 = {}^C_B Q \otimes {}^B_A Q \tag{3.67}$$

Note that for the given form of quaternion multiplication, the order of multiplication is opposite to the order of occurrence. This is similar to the order of the rotation matrix multiplication for multiple frames. This is not the case for the other form for quaternion multiplication.

$${}^C_A Q = Q_1 \odot Q_2 = {}^B_A Q \odot {}^C_B Q \tag{3.68}$$

3.5.2 Rotations referenced to fixed frames

It is possible for a rotation to be given with respect to an inertial or fixed frame of reference. Using the three frames of reference previously defined, let Q_1 be a quaternion which gives the rotation from frame {A} to frame {B} referenced to frame {A}, followed by a rotation Q_2 which is also given with respect to frame {A}. After the first rotation Q_1 has been performed, the current frame of reference is frame {B}. Before the second rotation is performed, the current frame of reference must be changed to frame {A}, followed by the rotation Q_2, followed by a transformation from frame {A} to frame {B}. Both these transformations from frame {A} to frame {B}, and vice versa are given by the rotation Q_1. This is illustrated in figure (3.6).

$$Q_1 = {}^B_A Q \qquad Q_2 = {}^C_A Q \tag{3.69}$$

$$\{A\} \longrightarrow Q_1 \longrightarrow \{B\}$$

$\longleftarrow$ Order of multiplication

Figure 3.5: Transformation from {A} to {B}

$$\{B\} \longrightarrow Q_1^{-1} \longrightarrow \{A\} \longrightarrow Q_2 \longrightarrow Q_1 \longrightarrow \{C\}$$

$\longleftarrow$ Order of multiplication

Figure 3.6: Transformation from {B} to {C}

The overall transformation from frame {A} to frame {C} is given by (3.70).

$$\begin{aligned} {}^{C}_{A}Q &= Q_1 \otimes Q_2 \otimes Q_1^{-1} \otimes Q_1 \\ &= Q_1 \otimes Q_2 \end{aligned} \tag{3.70}$$

3.6 Euler Angles

A very common form of representing the orientation of a moving body are the Euler Angles. The Euler Angles use a combination of three subsequent rotations around the body fixed axes $\hat{x}_b$, $\hat{y}_b$, and $\hat{z}_b$. Three separate rotations are required since a moving body in space has three degrees of freedom. Since different combinations of Euler Angles are achieved by taking rotations about different axes, or in different order, there exists twelve different sets of Euler Angles. There are two subsets of the Euler angles, namely the symmetric and antisymmetric Euler angles, which are dependant on the axes of rotation. The angles of the three rotations are labeled as they occur in order by ψ, θ, and ϕ, respectively. The indices 1, 2, and 3 are used to denote the axes $\hat{x}_b$, $\hat{y}_b$, and $\hat{z}_b$, respectively. An example of the notation used to represent the Euler Angles using the direct cosine matrix is given in (3.71).

$$R_{132} = R(\hat{y},\phi)R(\hat{z},\theta)R(\hat{x},\psi) \tag{3.71}$$

For the example given by (3.71), the first rotation is taken about the $\hat{x}$ axis, followed by the rotation about the body fixed $\hat{z}$ and $\hat{y}$ axes. The rotation matrices are then multiplied in reverse order (see *Compositions of Multiple Rotations*). For the symmetric set of Euler Angles, one axis is used twice to represent the first and last rotation, where a different axis is used to represent the second rotation.

Symmetric Set:

$$\begin{array}{cc} R_{121} & R_{131} \\ R_{212} & R_{232} \\ R_{313} & R_{323} \end{array}$$

The 3-1-3 set of Euler angles is the most common form of the symmetric set. It is commonly used to represent spinning bodies, for example orbiting satellites or in quantum mechanics. The antisymmetric Euler angles use all three axes to represent rotations.

Antisymmetric Set:

$$\begin{array}{cc} R_{123} & R_{132} \\ R_{213} & R_{231} \\ R_{312} & R_{321} \end{array}$$

The 3-2-1 set of Euler angles is commonly used to describe the orientation of aircraft. This representation uses the well known terms *roll*, *pitch*, and *yaw*, to describe the angles ϕ, θ, and ψ, respectively.

3.6.1 The 3-2-1 Set of Euler Angles

From (3.71), the 3-2-1 set is formulated using direct cosine matrices or quaternion. The rotation matrix and quaternion given represent the rotation from the inertial frame to the body-fixed frame. Using this notation, the aircrafts roll, pitch and yaw are describe by the rotations ϕ, θ and ψ, respectively. Using this convention, the rotation matrix describing the overall rotation is given by

$$
{}_o^bR_{321} = R(\hat{x}_b,\phi)R(\hat{y}_b,\theta)R(\hat{z}_b,\psi) \tag{3.72}
$$

$$
= \begin{pmatrix} 1 & 0 & 0 \\ 0 & \cos\phi & \sin\phi \\ 0 & -\sin\phi & \cos\phi \end{pmatrix} \begin{pmatrix} \cos\theta & 0 & -\sin\theta \\ 0 & 1 & 0 \\ \sin\theta & 0 & \cos\theta \end{pmatrix} \begin{pmatrix} \cos\psi & \sin\psi & 0 \\ -\sin\psi & \cos\psi & 0 \\ 0 & 0 & 1 \end{pmatrix}
$$

By performing the above operations, a simplified expression giving the rotation from the inertial frame to the body-fixed frame is found as a function of the 3-2-1 set of Euler angles, where $c_\gamma = \cos\gamma$ and $s_\gamma = \sin\gamma$ for $\gamma = \phi, \theta, \psi$, and is given by

$$
{}_o^bR_{321} = \begin{pmatrix} c_\theta c_\psi & c_\theta s_\psi & -s_\theta \\ s_\phi s_\theta c_\psi - c_\phi s_\psi & s_\phi s_\theta s_\psi + c_\phi c_\psi & s_\phi c_\theta \\ c_\phi s_\theta c_\psi + s_\phi s_\psi & c_\phi s_\theta s_\psi - s_\phi c_\psi & c_\phi c_\theta \end{pmatrix} \tag{3.73}
$$

The Euler angles are commonly used since it is much easier to imagine the orientation of a body when given the values of roll, pitch and yaw. The direct cosine matrix and quaternion do not immediately give insight to the actual orientation. Another advantage to the Euler angles is that it is a minimal realization for the attitude of a moving body, requiring only three terms. The disadvantage is that there exists a singularity for when the pitch or $\theta = \pm\pi/2$. For this condition, usually where an aircraft is pointing straight up or down, the yaw and the roll are performed on the same axis of rotation. A singularity exists as a result since there is no unique solution for the yaw and roll. With exception to the singularity the Euler angles can be determined given a direct cosine matrix by the following equations

$$
\theta = \arcsin\left(-{}_o^bR_{13}\right) \tag{3.74}
$$

$$
\phi = atan2({}_o^bR_{23}, {}_o^bR_{33}) \qquad \cos\theta \neq 0 \tag{3.75}
$$

$$
\psi = atan2({}_o^bR_{12}, {}_o^bR_{11}) \qquad \cos\theta \neq 0 \tag{3.76}
$$

The notation ${}_o^bR$ is important since the conversion from Euler angles to the direct cosine matrix is sometimes given as ${}_b^oR$, where the cosine matrix gives the rotation from the body-fixed frame to the inertial frame and the Euler angles give the opposite rotation from the inertial frame to the body-fixed frame

$$
{}_b^oR = {}_o^bR^T = \begin{pmatrix} c_\theta c_\psi & s_\phi s_\theta c_\psi - c_\phi s_\psi & c_\phi s_\theta c_\psi + s_\phi s_\psi \\ c_\theta s_\psi & s_\phi s_\theta s_\psi + c_\phi c_\psi & s_\phi s_\theta c_\psi - c_\phi s_\psi \\ -s_\theta & s_\phi c_\theta & c_\phi c_\theta \end{pmatrix} \tag{3.77}
$$

$$
\theta = \arcsin\left(-{}_b^oR_{31}\right) \tag{3.78}
$$

$$\phi = atan2({}^o_bR_{32}, {}^o_bR_{33}) \qquad \cos\theta \neq 0 \tag{3.79}$$

$$\psi = atan2({}^o_bR_{21}, {}^o_bR_{11}) \qquad \cos\theta \neq 0 \tag{3.80}$$

A similar result is obtained by performing quaternion multiplication of the three separate rotations, where $c_{\gamma/2}$ and $s_{\gamma/2}$ denote $\cos(\gamma/2)$ and $\sin(\gamma/2)$, respectively, where $\gamma = \phi, \theta, \psi$, by

$${}^b_oQ_{321} = Q(\hat{x}_b, \phi) \otimes Q(\hat{y}_b, \theta) \otimes Q(\hat{z}_b, \psi) \tag{3.81}$$

$${}^b_oQ_{321} = \begin{pmatrix} \cos(\phi/2) \\ \sin(\phi/2) \\ 0 \\ 0 \end{pmatrix} \otimes \begin{pmatrix} \cos(\theta/2) \\ 0 \\ \sin(\theta/2) \\ 0 \end{pmatrix} \otimes \begin{pmatrix} \cos(\psi/2) \\ 0 \\ 0 \\ \sin(\psi/2) \end{pmatrix} \tag{3.82}$$

$$= [\cos(\psi/2) + \sin(\psi/2)\,\mathbf{k}] \odot [\cos(\theta/2) + \sin(\theta/2)\,\mathbf{j}] \odot [\cos(\phi/2) + \sin(\phi/2)\,\mathbf{i}]$$

$${}^b_oQ_{321} = \begin{pmatrix} q_o \\ q \end{pmatrix} = \begin{pmatrix} c_{\phi/2}c_{\theta/2}c_{\psi/2} + s_{\phi/2}s_{\theta/2}s_{\psi/2} \\ s_{\phi/2}c_{\theta/2}c_{\psi/2} - c_{\phi/2}s_{\theta/2}s_{\psi/2} \\ c_{\phi/2}s_{\theta/2}c_{\psi/2} + s_{\phi/2}c_{\theta/2}s_{\psi/2} \\ c_{\phi/2}c_{\theta/2}s_{\psi/2} - s_{\phi/2}s_{\theta/2}c_{\psi/2} \end{pmatrix} \tag{3.83}$$

$$\theta = \arcsin(2(q_oq_2 - q_3q_1)) \tag{3.84}$$

$$\phi = atan2(q_3 + q_1, q_o - q_2) - atan2(q_3 - q_1, q_o + q_2) \qquad \cos\theta \neq 0 \tag{3.85}$$

$$\psi = atan2(q_3 + q_1, q_o - q_2) + atan2(q_3 - q_1, q_o + q_2) \qquad \cos\theta \neq 0 \tag{3.86}$$

3.7 Attitude Kinematics

The direct cosine matrix and the quaternion are useful in describing the instantaneous orientation of a moving body. Since these methods are only valid for a single point in time, alone they do not provide the ability to describe the continuous motion of a moving body. A method which is based on the work in [21] is proposed which gives first order differential equations representing the continuous motion of the orientation of a moving body. These differential equations are given as functions of the direct cosine matrix and the quaternion.

3.7.1 Direct Cosine Matrices

Recall the relationship between the direct cosine matrix and a vector of rotation which is given by

$$ {}^b_oR(\hat{k},\theta) = I + (1-\cos\theta)S(\hat{k})^2 - \sin\theta\, S(\hat{k}) \tag{3.87} $$

Subsequent to the given rotation, ${}^b_oR$, an infinitesimal rotation, $\Phi(t+\Delta t)$, is proposed which describes the change in the direct cosine matrix over the infinitesimal interval of time, Δt

$$ {}^b_oR(t+\Delta t) = \Phi(t+\Delta t){}^b_oR(t) \tag{3.88} $$

Since $\Phi(t+\Delta t)$ is a rotation, it can be described by a certain vector of rotation, and a infinitesimal angle of rotation $\Delta\theta$. Since the angle $\Delta\theta$ is infinitesimally small, approximations to the trigonometric terms can be applied, or $\sin\Delta\theta \approx \Delta\theta$, and $\cos\Delta\theta \approx 1$. In light of (3.87) and the small angle approximations, $\Phi(t+\Delta t)$ is given by

$$ \Phi(t+\Delta t) = I - \Delta\theta S(\hat{k}) = I - S(\xi) \tag{3.89} $$

$$ \xi = \Delta\theta\hat{k} \tag{3.90} $$

The term $\xi = \Delta\theta\hat{k}$, which describes a vector of rotation by a certain angle, is closely related to the angular rate of change of the moving body with respect to time

$$ \Omega = \lim_{\Delta t\to 0} \frac{\xi}{\Delta t} \tag{3.91} $$

The vector Ω describes the angular rate of change of the moving body with respect to time, otherwise known as the body referenced angular velocity. It is taken with respect to the body-fixed frame since $\Phi(t+\Delta t)$ was originally described as a rotation referenced to the body-fixed frame. Since Ω is a vector, it can also be described in the inertial frame by using the direct cosine matrix, R. The angular velocity of a moving body with respect to the inertial frame is given by Ω_o. Using the given conventions, the time rate of change of the direct cosine matrix is found from basic principals

$$ \Omega = {}^b_oR\Omega_o \tag{3.92} $$

$$ \frac{d}{dt}\left({}^b_oR\right) = \lim_{\Delta t\to 0} \frac{{}^b_oR(t+\Delta t) - {}^b_oR(t)}{\Delta t} \tag{3.93} $$

Using the result given by (3.89), we have

$$ {}^b_o\dot{R} = \lim_{\Delta t\to 0} -S\left(\frac{\xi}{\Delta t}\right){}^b_oR \tag{3.94} $$

$$ {}^b_o\dot{R} = -S(\Omega){}^b_oR \tag{3.95} $$

To determine an expression for the inverse rotation, ${}^o_bR$, or the rotation from the body-fixed frame to the inertial frame, the transpose is performed on (3.88). Since each term in (3.88) is a rotation, the transpose is equivalent to the inverse

$$ {}^o_bR(t+\Delta t) = {}^b_oR(t+\Delta t) = {}^o_bR(t)\Phi(t+\Delta t)^T \tag{3.96}$$

$$\Phi(t+\Delta t)^T = I + S(\xi) \tag{3.97}$$

$$ {}^o_b\dot{R} = {}^o_bRS(\Omega) \tag{3.98}$$

This can be used to prove that the transformation between ${}^b_o\dot{R}$ and ${}^o_b\dot{R}$ is given by the transpose as shown by

$$ {}^o_b\dot{R} = {}^b_o\dot{R}^T \tag{3.99}$$

The above differential equations are all given as a function of the body-fixed angular velocity vector, Ω_b. To determine differential equations with respect to the inertial-based angular velocity vector, Ω_o, the relationship given by (3.92) is used with a property of the skew-symmetric matrix given by

$$S\left(\left(M^T\right)^{-1}u\right) = \frac{1}{|M|}MS(u)M^T \tag{3.100}$$

The above property is given for an arbitrary square matrix M, and a arbitrary three-dimensional vector u. For rotation matrices, this property is simplified as follows

$$S(Ru) = RS(u)R^T \tag{3.101}$$

Using the expressions given by (3.92), (3.101), (3.95) and (3.98), new differential equations are found which are given with respect to the inertial-based angular velocity

$$ {}^b_o\dot{R} = -{}^b_oRS(\Omega_o) \tag{3.102}$$

$$ {}^o_b\dot{R} = S(\Omega_o){}^o_bR \tag{3.103}$$

3.7.2 Euler-Rodrigues Symmetric Parameters

A similar approach used for the direct cosine matrix can be applied to the Euler-Rodrigues Symmetric set of the quaternion, where $\Theta(t+\Delta t)$ is a quaternion which describes the infinitesimal change in the quaternion ${}^b_oQ(t)$ over an infinitesimal time interval Δt. The quaternion describing the orientation after the interval Δt, denoted by ${}^b_oQ(t+\Delta t)$ can be found as a result of quaternion multiplication.

$$ {}^b_oQ(t+\Delta t) = \Theta(t+\Delta t) \otimes {}^b_oQ(t) \tag{3.104}$$

From the definition of the Euler-Rodrigues symmetric parameters and the small angle approximations the quaternion $\Theta(t+\Delta t)$ is given by (3.105).

$$\Theta(t+\Delta t) = \begin{pmatrix} 1 \\ \Delta\theta/2\hat{k} \end{pmatrix} = \begin{pmatrix} 1 \\ \xi/2 \end{pmatrix} \tag{3.105}$$

The change in orientation over the interval Δt can be found using the distributive property of the quaternion

$$\begin{aligned} {}^b_oQ(t+\Delta t) - {}^b_oQ(t) &= (\Theta(t+\Delta t) - Q_I) \otimes Q(t) \\ &= \frac{1}{2}\begin{pmatrix} 0 \\ \xi \end{pmatrix} \otimes Q(t) \end{aligned} \tag{3.106}$$

The time rate of change of the quaternion is then found from basic principals by

$$\frac{d}{dt}{}^b_oQ = \lim_{\Delta t \to 0}\left(\frac{{}^b_oQ(t+\Delta t) - {}^b_oQ(t)}{\Delta t}\right) \tag{3.107}$$

$${}^b_o\dot{Q} = \frac{1}{2}Q_\Omega \otimes {}^b_oQ \tag{3.108}$$

$$Q_\Omega = \begin{pmatrix} 0 \\ \Omega \end{pmatrix} \tag{3.109}$$

To determine a differential equation describing the rotation from the body-fixed frame to the inertial frame, consider the diagram given by Figure (3.7).

$$\{t+\Delta t\} \longrightarrow \Theta^{-1} \longrightarrow \{t\} \longrightarrow {}^o_bQ \longrightarrow \{o\}$$

$\longleftarrow$ Order of multiplication

Figure 3.7: Transformation from body-fixed frame to inertial frame

As described in the compositions of multiple quaternions section, the order of operations for quaternion multiplication can be determined from figure (3.7), which is used to obtain

$${}^o_bQ(t+\Delta t) = {}^o_bQ(t) \otimes \Theta^{-1} \tag{3.110}$$

$$\Theta^{-1} = \begin{pmatrix} 1 \\ -\xi \end{pmatrix} \tag{3.111}$$

Using the same process described previously, the differential equation which is based on the rotation from the body-fixed frame to the inertial frame is given

$${}^o_b\dot{Q} = -\frac{1}{2}{}^o_bQ \otimes Q_\Omega \tag{3.112}$$

The obtained differential equations are all given with respect to the body-fixed angular velocity vector. To determine differential equations which are given with respect to the inertial-based angular velocity vector a transformation is used which is given by

$$Q_{\Omega_b} = {}^b_oQ \otimes Q_{\Omega_o} \otimes {}^b_oQ^{-1} \tag{3.113}$$

$$
\begin{aligned}
{}^{o}_{b}\dot{Q} &= -\frac{1}{2}\,{}^{o}_{b}Q \otimes {}^{b}_{o}Q \otimes Q_{\Omega_o} \otimes {}^{b}_{o}Q^{-1} \\
{}^{o}_{b}\dot{Q} &= -\frac{1}{2} Q_{\Omega_o} \otimes {}^{o}_{b}Q \qquad (3.114)
\end{aligned}
$$

Similarly,

$$
{}^{b}_{o}\dot{Q} = \frac{1}{2}\,{}^{b}_{o}Q \otimes Q_{\Omega_o} \qquad (3.115)
$$

Chapter 4

Ducted Fan Model

In order to develop model-based control laws for the ducted fan system, a system model is required which describes the linear and rotational motion of the vehicle using a set of non-linear continuous differential equations. The Newton-Euler method is used which gives the motion of a vehicle by analytically describing all the forces and torques which are applied to a rigid body. The aerodynamic theory previously discussed provides reasonable approximations to the thrust produced as well as the forces acting on the control ailerons. Other torques, which are not intuitive, occur due to multiple simultaneous rotations of the rigid body about different axes. These torques, otherwise known as gyroscopic torques, are derived in the next section. All forces are described in either the inertial or body-fixed frame using the theory outlined in the attitude representation section.

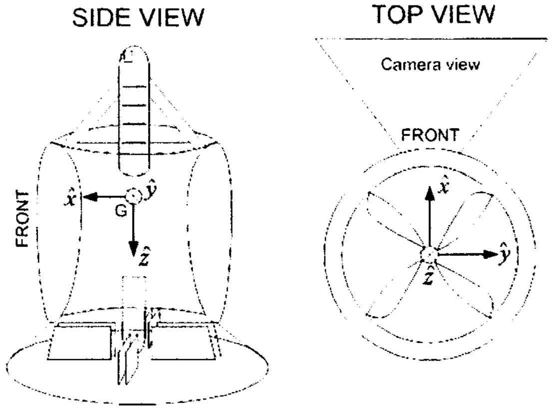

Figure 4.1: Body-Fixed Axes

The differential equations which describe the rotational motion of the aircraft are also obtained by the theory outlined in the attitude kinematics section. In order to describe the system forces, it is useful at this point to create a set of axes for the inertial frame and the body-fixed frame. Figure 4.1 describes the body-fixed axes which are rigidly attached to the aircraft center of mass, G. The center of gravity is ideally located somewhere between the two rotors which is likely the case due to the upper and lower distribution of the heavy electronics, for example batteries and motors. The body-fixed axes are established by directing the x-axis towards the front of the aircraft and the z-axis pointing downward in the direction of the thrust. The body-fixed frame is then completed by taking the y-axis towards the right side of the aircraft. The inertial frame is chosen by taking the x-axis towards magnetic north and the z-axis pointing downward towards the center of the earth. The y-axis then points in an Eastern direction.

4.1 Definition of Previously Used Terms

The following is a summary of some of the previously defined terms which will be used to formulate a system model.

p : inertial-referenced system position
v : inertial-referenced system velocity
m : mass of the system
Ω : body referenced angular velocity
I_b : body referenced system inertia tensor
ω_d : rotor differential speed ($\omega_d = \omega_1 - \omega_2$)
ω_1 : angular velocity of rotor 1 with positive (CCW) rotation
ω_2 : angular velocity of rotor 2 with negative (CW) rotation
Q_1 : drag experienced by rotor with velocity ω_1
Q_2 : drag experienced by rotor with velocity ω_2
I_r : rotor body-referenced z-axis moment of inertia
R : rotor radius
A : rotor disk area ($A = \pi R^2$)
θ_{75} : rotor blade pitch at 3/4 radius
σ : rotor solidity (ratio of total blade area to rotor disk area)
a_d : ratio of duct exit area to rotor disk area ($a_d = A_d/A$)
a : change in aileron lift coefficient wrt α ($a = dC_l/d\alpha$)
b : width of control aileron along the body-referenced x or y axis
c : control aileron chord or height along body-referenced z axis
G : center of mass
l : distance along body-referenced z axis from G to aileron center of pressure
d : distance along body-referenced x or y axis from G to aileron center of pressure

4.2 Rotational Kinematics

The dynamic motion of the aircraft can be modeled by applying all external forces and torques to the center of mass. Using Newton's laws the translational and rotational dynamics are found as a result of the external forces and torques, respectively. This section deals with the internal and external torques applied to the aircraft. Since we have a body of mass which is not symmetrical with respect to all axis multiple simultaneous rotations of the body can produce torques known as gyroscopic torques. In addition to the rotation of the body, the rotors are also rotating at high angular velocities in order to generate the thrust. The simultaneous rotation of the body and the rotors will also cause gyroscopic torques that can be determined using the principle of angular momentum variation [23]. This method states that all changes in the angular momentum of a body is caused by and is equal to all applied external torques. The angular momentum and external torques viewed from the inertial frame of reference are denoted by M_o and τ_o, respectively. In general the angular momentum is the product of the inertia tensor, I, and the angular velocity vector, Ω

$$M = I\Omega \tag{4.1}$$

$$\tau_o = \frac{d}{dt}(M_o) = \frac{d}{dt}(I_o\Omega_o) \tag{4.2}$$

For the given model, the external torques are the control effort τ_a, the aerodynamic drag on the rotor τ_Q, and a disturbance torque τ_d. The angular velocity of the rotor which has a positive (CCW) rotation is given by ω_1, which is opposed by the negative (CW) rotation of the second rotor which has an angular velocity given by ω_2. Using this convention the external torques modeled in the body-fixed frame is given by (

$$\tau_b = \tau_a + \tau_Q + \tau_d = \begin{pmatrix} \tau_x \\ \tau_y \\ \tau_z \end{pmatrix} + \begin{pmatrix} 0 \\ 0 \\ Q_2 - Q_1 \end{pmatrix} + \tau_d \tag{4.3}$$

where Q_1 and Q_2 are the aerodynamic drag of the positively and negatively rotating rotors, respectively. The inertia tensor I_o describes the distribution of mass in the aircraft. If the aircraft is rotating with respect to the inertial frame then this inertia tensor will change with time. In order to find the time rate of change of this inertia tensor the body-fixed inertia tensor can be used which is constant. A general expression for the body-fixed inertia tensor is

$$I_b = \begin{pmatrix} I_{xx} & I_{xy} & I_{xz} \\ I_{yx} & I_{yy} & I_{yz} \\ I_{zx} & I_{zy} & I_{zz} \end{pmatrix} \tag{4.4}$$

This expression can be simplified such that the inertia tensor is a diagonal matrix given the body is symmetric and is modeled about the center of mass. Note that the inertia tensor, I_b, is determined with respect to the body fixed frame. The inertia tensor described in the body-fixed frame can be described in the inertial frame using a direct cosine matrix which describes the rotation between frames. Let the rotation matrix given by

$$R = {}^{b}_{o}R \tag{4.5}$$

describe the rotation **from** the inertial frame **to** the body fixed frame. The inertial frame based inertia tensor can be described as a function of the body fixed inertia tensor

$$I_o = R^T I_b R \tag{4.6}$$

In order to describe the contribution of the rotors rotation to the angular momentum, the problem is separated into the three vector components. In this model the mass of the rotors are included in the body-fixed inertia tensor. Two extra terms are added to the $\hat{z}$ component to include the momentum associated with the rotor angular velocity and the scalar moment of inertia, I_r.

$$\begin{aligned} M_b \cdot \hat{x} &= I_{xx}\omega_x + I_{xy}\omega_y + I_{xz}\omega_z && (4.7) \\ M_b \cdot \hat{y} &= I_{yx}\omega_x + I_{yy}\omega_y + I_{yz}\omega_z && (4.8) \\ M_b \cdot \hat{z} &= I_{zx}\omega_x + I_{zy}\omega_y + I_{zz}\omega_z + I_r\omega_1 - I_r\omega_2 && (4.9) \end{aligned}$$

For convenience, the difference of the rotor velocities is represented using

$$\omega_d = \omega_1 - \omega_2 \tag{4.10}$$

$$M_b = I_b\Omega + I_r\omega_d\hat{z} \tag{4.11}$$

The angular momentum modeled in the inertial frame is modified to include the momentum of the rotor

$$M_o = I_o\Omega_o + I_r\omega_d\hat{z}_o \tag{4.12}$$

where $\hat{z}_o$ is the vector $\hat{z}$ transformed from the body-fixed frame to the inertial frame. Using the inertia tensor transformation given in (4.6) and the rotation R given in (4.5) to transform the vector associated with the rotor momentum, we obtain a new expression for the inertial based angular momentum

$$M_o = R^T I_b R\Omega_o + R^T I_r\omega_d\hat{z} \tag{4.13}$$

$$\tau_o = \frac{d}{dt}(M_o) = \frac{d}{dt}\left(R^T I_b R\Omega_o + R^T I_r\omega_d\hat{z})\right) \tag{4.14}$$

Recall the time derivative of a direct cosine matrix

$$\dot{R} = {}^b_o\dot{R} = -S(\Omega){}^b_oR \tag{4.15}$$

$$\dot{R}^T = {}^b_o\dot{R}^T = {}^b_oR^T S(\Omega) \tag{4.16}$$

Using the above descriptions for the derivative of the cosine matrix and application of the chain rule yields the result

$$\tau_o = R^T\Omega \times I_b\Omega + R^T I_b\dot{\Omega} + R^T(\Omega \times \hat{z}) I_r\omega_d + R^T I_r\dot{\omega}_d\hat{z} \tag{4.17}$$

The external applied torques expressed in the body-fixed frame is found by multiplying the above result by the cosine matrix R to obtain

$$\tau_b = \Omega \times I_b\Omega + I_b\dot{\Omega} + (\Omega \times \hat{z}) I_r\omega_d + I_r\dot{\omega}_d\hat{z} \tag{4.18}$$

Using the result given by (4.18) the differential equation describing the rotational kinematics is obtained.

$$I_b\dot{\Omega} = -\Omega \times I_b\Omega - I_r(\Omega \times \hat{z})\omega_d - I_r\dot{\omega}_d\hat{z} - (Q_1 - Q_2)\hat{z} + \tau_a + \tau_d \tag{4.19}$$

4.3 The Control Inputs F_a and τ_a

The system control, with exception to the thrust, T, and differential speed, ω_d, is generated by four independently controlled ailerons at the duct exit. Each aileron will produce lift or force which is orthogonal to the direction of airflow. This force also creates a moment with respect to the center of gravity, G. To analytically describe these forces and torques the ailerons must be identified with respect to the body-fixed axes previously described.

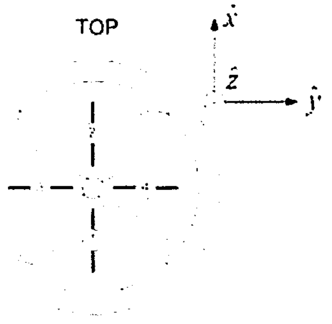

Figure 4.2: Ducted Fan Control Ailerons – Top View

The four ailerons are numbered as shown in Figure 4.2 with ailerons 1 and 2 are located on the x-axis, and ailerons 3 and 4 located on the y-axis. Figure 4.3 gives a more detailed illustration of control ailerons 1 and 2, where ailerons 3 and 4 are described by figure 4.4. The aerodynamic center of the aileron is dependant on the location of the airfoil flap if flapped airfoils are used. For non-flapped airfoils the aerodynamic center is located at a quarter of the chord length. For both flapped and non-flapped airfoil, the location of the aerodynamic center is located at some point in the center of the aileron span which is located on the x-axis for ailerons 1 and 2, or y-axis for ailerons 3 and 4. The vectors describing the locations of ailerons 1 through 4 with respect to the aircraft center of mass are given by

$$\begin{pmatrix} r_1 \\ r_2 \\ r_3 \\ r_4 \end{pmatrix} = \begin{pmatrix} -d & 0 & l \\ d & 0 & l \\ 0 & -d & l \\ 0 & d & l \end{pmatrix} \tag{4.20}$$

where each vector is decomposed into a length l along the z-axis and a width d along the x-axis or y-axis. The control aileron angle of attack is defined as the angle between the body-fixed z-axis and the aileron chord, taken about the x-axis for ailerons 1 and 2, or y-axis for ailerons 3 and 4. The angle of attack for ailerons 1 through 4 is given by α_1 through α_4, respectively. The force on control surfaces 1 through 4 are given by

$$\begin{pmatrix} F_1 \\ F_2 \\ F_3 \\ F_4 \end{pmatrix} = k_L T \begin{pmatrix} \alpha_1 \hat{y} \\ \alpha_2 \hat{y} \\ -\alpha_3 \hat{x} \\ -\alpha_4 \hat{x} \end{pmatrix} \tag{4.21}$$

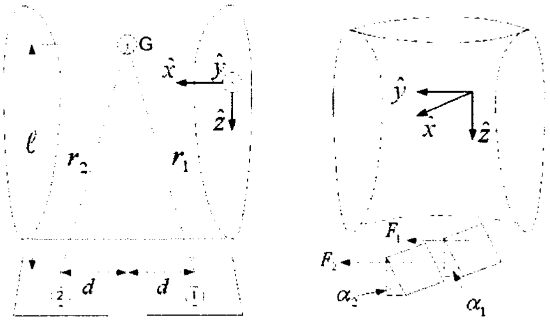

Figure 4.3: Control Ailerons 1 and 2

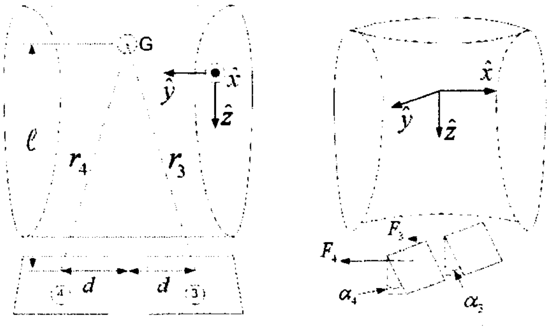

Figure 4.4: Control Ailerons 3 and 4

which is used to determine the net torque for all of the control surfaces

$$F_a = \begin{pmatrix} -k_L T(\alpha_3 + \alpha_4) \\ k_L T(\alpha_1 + \alpha_2) \\ 0 \end{pmatrix} = k_L T \begin{pmatrix} 0 & 0 & -1 & -1 \\ 1 & 1 & 0 & 0 \\ 0 & 0 & 0 & 0 \end{pmatrix} \begin{pmatrix} \alpha_1 \\ \alpha_2 \\ \alpha_3 \\ \alpha_4 \end{pmatrix} \tag{4.22}$$

In general, the torque resulting from a force acting on a lever arm is given by (4.23). Each aileron will generate a torque, denoted by τ_i for $i = 1, 2, 3, 4$, about the aircraft center of mass. These torques are obtained from (4.23) and the distances from the aircraft center of mass to the aileron aerodynamic center, given previously by r_1 through r_4

$$\tau = r \times F \tag{4.23}$$

$$\tau_i = r_i \times F_i \qquad i = 1, 2, 3, 4 \tag{4.24}$$

$$\begin{aligned}\tau_1 &= k_L T\alpha_1 \begin{pmatrix} -l & 0 & -d \end{pmatrix}^T \\ \tau_2 &= k_L T\alpha_2 \begin{pmatrix} -l & 0 & d \end{pmatrix}^T \\ \tau_3 &= k_L T\alpha_3 \begin{pmatrix} 0 & -l & -d \end{pmatrix}^T \\ \tau_4 &= k_L T\alpha_4 \begin{pmatrix} 0 & -l & d \end{pmatrix}^T\end{aligned} \tag{4.25}$$

The individual torques τ_1 through τ_4 are grouped with respect to the body-fixed axes to give the applied torque

$$\tau_a = k_L T \begin{pmatrix} -l & -l & 0 & 0 \\ 0 & 0 & -l & -l \\ -d & d & -d & d \end{pmatrix} \begin{pmatrix} \alpha_1 \\ \alpha_2 \\ \alpha_3 \\ \alpha_4 \end{pmatrix} \tag{4.26}$$

A relationship between τ_a and F_a is given by

$$F_a = -\frac{1}{l} S(\hat{z})\tau_a \tag{4.27}$$

4.4 Aileron Force Analysis

In order to determine the forced exerted by the control surfaces, the airflow velocity at the duct exit is required. The airflow is dependant on the system weight and vertical speed. Since the system will be operated at low velocities, or hover, we assume the vertical velocity is negligible. Therefore, for a state of hover the relationship between the system thrust and the exit airflow velocity is given by

$$v_e = \sqrt{\frac{T}{\rho A a_d}} \tag{4.28}$$

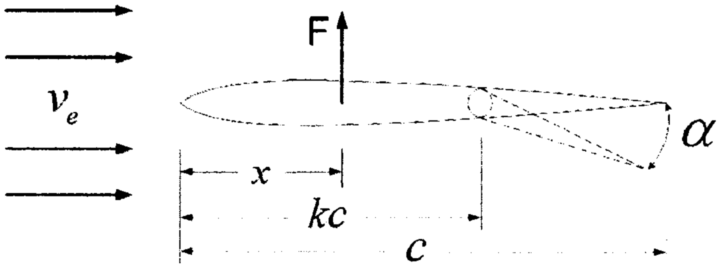

Figure 4.5: Flapped Airfoil

Since the system vertical velocity is very low in comparison to the airflow velocity, we assume the value of thrust is equal to the system weight. Using the values given in Table A.1 and assuming a 15% loss in velocity due to friction and rotation losses,

$$v_e \approx 14.3m/s \tag{4.29}$$

For this system a flapped airfoil is used as shown by Figure (4.5). The leading part of the airflow has a fixed angle of attack, or $\alpha = 0$. The dimensions for the airfoil are given in Table A.1. The literature also suggests a 15.6% loss in the lift coefficient, which yields,

$$c_l \approx 4.44\alpha \tag{4.30}$$

$$x = 0.3391c \tag{4.31}$$

Therefore, the force generated by a control surface (2 ailerons) is given by

$$\begin{aligned} F &= c_l \rho b c v^2 \\ &\approx 14.65\,\alpha N \end{aligned} \tag{4.32}$$

This results in the applied torque as a function of α given by

$$\tau = \Phi\alpha \tag{4.33}$$

$$\Phi = \begin{pmatrix} -2.605 & -2.605 & 0 & 0 \\ 0 & 0 & -2.605 & -2.605 \\ -1.861 & 1.861 & -1.861 & 1.861 \end{pmatrix} \tag{4.34}$$

4.4.1 Properties of Air at Standard Conditions

The standard conditions of air given at sea level and at 298K, or 25^oC. Some physical properties of air are given below in addition to the speed of sound.

$$\rho = 1.205kg/m^3 \tag{4.35}$$

$$\mu = 1.862 \times 10^{-5} kg(ms)^{-1} \tag{4.36}$$

$$v_{sound} = 340.29m/s \tag{4.37}$$

4.5 Servo-Angle Determination

Having obtained the desired torques from the control law, a method is required to determine the angle for each control surface. Due to the redundancy in the control actuators [1], an infinite number of solutions exist for the servo angles. Therefore, a solution which optimizes the control effort is investigated. A general expression for the applied torque τ in terms of the aileron angle α is given by

$$\tau = \Phi\alpha \tag{4.38}$$

where $\alpha = (\alpha_1 ... \alpha_4)^T$ and the matrix Φ was previously given by

---

[1] There are 6 actuators in total which can provide a torque on the z axis, specifically the four control surfaces in addition to the two main rotors. Two actuators each are used to create a torque on the x and y axes.

$$\Phi = k_L T \begin{pmatrix} -l & -l & 0 & 0 \\ 0 & 0 & -l & -l \\ -d & d & -d & d \end{pmatrix} \tag{4.39}$$

Consider the cost function that is designed to minimize the aileron angle α and the difference between the definition of the applied torque from (4.38) and the actual torque τ using the Langrangian multiplier λ, given by

$$J = \tfrac{1}{2}\alpha^T P \alpha + \lambda^T (\tau - \Phi\alpha) \qquad \lambda \in \mathbb{R}^3 \tag{4.40}$$

where $P = P^T > 0$. Taking the partial derivatives of the cost function reveals

$$\frac{\partial}{\partial \alpha} J = P\alpha - \Phi^T \lambda \tag{4.41}$$

$$\frac{\partial}{\partial \lambda} J = \tau - \Phi\alpha \tag{4.42}$$

To find the minimum of the cost function we set (4.41) and (4.42) to zero. From (4.41) we obtain $\alpha = P^{-1}\Phi^T\lambda$, which is substituted into (4.42) to obtain

$$\tau = \Phi P^{-1} \Phi^T \lambda \tag{4.43}$$

$$\lambda = \left(\Phi P^{-1} \Phi^T\right)^{-1} \tau \tag{4.44}$$

$$\alpha = P^{-1}\Phi^T \left(\Phi P^{-1} \Phi^T\right)^{-1} \tau \tag{4.45}$$

Effectively, this algorithm evenly distributes the control effort equally over the four control surfaces. A choice of $P = I_{4\times4}$ is used since for a given control effort we want the control effort to be divided equally over the control actuators. A yaw effort is distributed over four control surfaces, where the pitch and roll effort is distributed over the two associated control surfaces. This is not an ideal solution since it is desirable to place a constraint on the yaw control effort. For example, if the aircraft yaw is far away from the desired yaw, a large control effort is used for the yaw causing control saturation. For this reason, it would be desirable to find a cost function which has the ability to place more weight on the pitch and roll efforts rather than the yaw. In practice, saturation was used on the yaw control effort signal to avoid actuator saturation.

4.6 External Forces

As previously mentioned, there are two sources of external airflow around the duct resulting in external forces. These sources are the wind and the airflow due to the motion of the duct. Due to the unpredictable nature of wind it cannot be included in the system model. For unknown forces, an interesting approach has been presented by [18]. This method develops an observer to estimate all the unknown aerodynamic forces, in addition to estimating the value ε which gives the distance from the system center of gravity to where the estimated force is applied. The estimated force over the distance ε effectively estimates the unknown aerodynamic moments which are experienced by the system. Regardless of whether this observer is implemented, using the force vector F_d and the scalar distance from the center of gravity along the z-axis, ε, is an effective way to model all external disturbance forces and torques together as one disturbance. Figure 4.6 illustrates the disturbance force F_d acting on the system at the point given by ε.

The angular acceleration of the system was previously derived and is given by (4.19), where τ_d was given as a disturbance torque. Since this disturbance torque is a function of the disturbance force F_d, a relationship between the force and torque is given by

$$\tau_d = \varepsilon\hat{z} \times F_d = \varepsilon S(\hat{z})F_d \tag{4.46}$$

The torque τ_d and force F_d are both given with respect to the body-fixed frame. Due to the symmetry of the system, the disturbance force F_d is assumed to act on a point located on the body-referenced z-axis. The distance from this point to the center of mass is given by ε. The disturbance force and the lever arm ε are time-varying values such that all external forces and moments acting on the system are collectively given by F_d and τ_d, respectively.

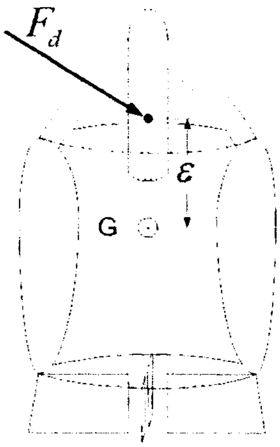

Figure 4.6: Grouping of All External Aerodynamic Forces and Moments

4.6.1 Aerodynamic Drag

Since the accelerometers are affected by linear accelerations of the system, it can be useful to model external forces which limit the motion of the system. As discussed in section 2.6.1, a model for the aerodynamic drag over the duct is given by

$$F_{aero} = \frac{1}{2}\rho c d C_d v^2 \tag{4.47}$$

where c is the duct chord, d is the duct diameter, and C_d is the drag coefficient which was found from [1] to be approximately equal to 1.2. If the aerodynamic drag is due to the motion of the system then the horizontal component of the body referenced system velocity is given by

$$v_{xy} = \begin{pmatrix} 1 & 0 & 0 \\ 0 & 1 & 0 \\ 0 & 0 & 0 \end{pmatrix} Rv \tag{4.48}$$

where v is the inertial referenced system velocity, and $R = {}^b_oR$. From this velocity a model of the aerodynamic drag expressed in the body-fixed frame is given by

$$F_{aero} = -0.16|v_{xy}|v_{xy} \tag{4.49}$$

where the duct diameter and chord were taken as $19in$ and $18in$, respectively. Although this model is very approximate, it can be useful for simulating the performance of the closed-loop system. It is assumed that F_{aero} acts evenly over the center of gravity and does not generate any moment on the system.

4.7 Final System Model

The final dynamic model is a set of first-order non-linear differential equations. The linear acceleration of the system is given by the sum of all the forces which are applied to the system. Since the forces are given with respect to the body-fixed frame, transformations must be utilized to express these forces in the inertial frame of reference.

4.7.1 Direct Cosine Matrix Model

Let R denote the direct cosine matrix which describes the transformation from the inertial frame to the body fixed frame.

$$R = {}^b_oR \tag{4.50}$$

The forces exerted on the body are the forces applied by the control ailerons, F_a, the rotor thrust T which points in the negative $\hat{z}$ direction, the disturbance force F_d, and the force due to gravity. All forces with exception to gravity, are expressed in the body-fixed frame which must be transformed to the inertial frame. The net force acting on the aircraft, expressed in the inertial frame, is given as

$$\sum F = mg\hat{z} - TR^T\hat{z} - \frac{1}{l}R^TS(\hat{z})\tau_a + R^TF_d + R^TF_{aero} \tag{4.51}$$

Recall from (3.95) the continuous time derivative of the direct cosine matrix given by (4.50) with respect to the body-fixed angular velocity Ω_b. The resulting set of differential equations are given below

$$\begin{aligned} \dot{p} &= v && (4.52) \\ m\dot{v} &= mg\hat{z} - TR^T\hat{z} - \frac{1}{l}R^TS(\hat{z})\tau_a + R^TF_d + R^TF_{aero} && (4.53) \\ I_b\dot{\Omega} &= -\Omega \times I_b\Omega - I_r(\Omega \times \hat{z})\omega_d - I_r\dot{\omega}_d\hat{z} - (Q_1 - Q_2)\hat{z} + \tau_a + \varepsilon\hat{z} \times F_d && (4.54) \\ \dot{R} &= -S(\Omega)R && (4.55) \end{aligned}$$

4.7.2 Quaternion Model

Let Q give the Euler Rodrigues symmetric parameter which describes the rotation from the inertial frame to the body-fixed frame. Recall the continuous time derivative of the quaternion given by

$$Q = {}^b_oQ = (q_o,\ q) \tag{4.56}$$

A direct cosine matrix is still utilized to perform the vector transformation. This direct cosine matrix can be expressed as a function of the quaternion, as shown by

$$R = {}^b_oR = I + 2S(q)^2 - 2q_oS(q) \tag{4.57}$$

$$\begin{aligned}
\dot{p} &= v && (4.58)\\
m\dot{v} &= mg\hat{z} - TR^T\hat{z} - \frac{1}{l}R^TS(\hat{z})\tau_a + R^TF_d + R^TF_{aero} && (4.59)\\
I_b\dot{\Omega} &= -\Omega \times I_b\Omega - I_r\left(\Omega \times \hat{z}\right)\omega_d - I_r\dot{\omega}_d\hat{z} - \left(Q_1 - Q_2\right)\hat{z} + \tau_a + \varepsilon\hat{z} \times F_d && (4.60)\\
\dot{Q} &= \frac{1}{2}Q \odot Q_\Omega && (4.61)
\end{aligned}$$

$$Q_\Omega = (0,\ \Omega) \tag{4.62}$$

4.7.3 Simplified Model

If the rotors are controlled such that the differential speed ω_d is zero, no disturbances are present, and the drag experienced by both rotors are the same, then a simplified model is obtained which is given below.

For $\omega_d = 0$, $Q_1 = Q_2$, and $F_d = \mathbf{0}$, the simplified model is given by

$$\begin{aligned}
\dot{p} &= v && (4.63)\\
m\dot{v} &= mg\hat{z} - TR^T\hat{z} - \frac{1}{l}R^TS(\hat{z})\tau_a + R^TF_{aero} && (4.64)\\
I_b\dot{\Omega} &= -\Omega \times I_b\Omega + \tau_a && (4.65)\\
\dot{R} &= -S(\Omega)R && (4.66)
\end{aligned}$$

Alternatively the quaternion can be used to represent the system orientation

$$\dot{Q} = \tfrac{1}{2}Q \odot Q_\Omega \tag{4.67}$$

Chapter 5

Attitude Estimation

The three types of sensors focused on in this thesis are accelerometers, magnetometers, and gyroscopes. Each sensor is triaxial having the capability to measure on the three orthogonal axes. Each of the three sensors has a role in estimating the system's attitude, however, the gyroscope is implemented differently from the accelerometers and magnetometers. The accelerometers and magnetometers are used to give body-fixed vector observations of the earth's gravity and magnetic field, respectively. The gyroscopes are used to obtain the body-fixed angular velocity of the aircraft. Since the gyroscope signals are related to the rate of change of the system attitude, integration is required to obtain estimates of the system attitude. The accelerometer and magnetometer signals are proportional to the system attitude and therefore do not require integration which overcomes the fundamental flaw of the gyroscopes. Still, the accelerometers and magnetometers are not without their own sources of error. Due to the unknown characteristics of the sensors, or the dynamics of the system, all of the sensors can be flawed. To address these inaccuracies all three sensors are utilized with the proposed estimation algorithms to obtain improved estimates of the system attitude.

5.1 Gyroscopes

Ideally, the gyroscopes would be used to measure the system body-fixed angular velocity Ω. However, in addition to Ω the gyroscope signals are affected by sensor bias, b, and noise, n_g. A model commonly used which addresses these factors is given by

$$\Omega_g = \Omega + b + n_g \tag{5.1}$$

In practice, gyroscope sensors have physical limitations such as bandwidth, and therefore have lowpass characteristics. Due to the presence of noise low-pass filters are often implemented either in hardware or software further deteriorating the accuracy of the sensor. A second gyroscope model is given by

$$\Omega_g(s) = \frac{1}{\tau s + 1}\mathcal{L}[\Omega(t) + b + n_g] \tag{5.2}$$

which includes a first-order representation of these low-pass characteristics, where τ is the time-constant of the low-pass filter.

In an effort to overcome the gyroscope bias problem, the gyroscope signals can be easily measured while the system is at rest. Still, since these signals are integrated even the smallest amount of bias will cause the attitude estimates to drift, especially over longer flight times. This practice also assumes that the gyro bias is constant, when it is actually time varying, and most often also varies with ambient temperature.

5.2 Accelerometers

Accelerometers are used to measure gravitational force to obtain a vector observation of gravity in the body-fixed frame. Since gravity in the inertial frame is known the accelerometer can be used to obtain 2 of the 3 degrees of freedom of the system attitude. However, in addition to measuring the force due to gravity, the accelerometers inherently measure other system forces, for example the force due to linear accelerations of the sensor which cannot be distinguished from the gravity vector. These forces can result from linear acceleration of the system as well as system rotational velocity and rotational acceleration when the sensor is not located at the system center of mass. A model which accounts for the linear accelerations of the sensor $\dot{v}_s$, sensor bias b_y, and sensor noise n_y, is given by

$$y = {}^b_oR\left(\hat{z} - \frac{1}{g}\dot{v}_s\right) + b_y + n_y \tag{5.3}$$

When the sensor is not located at the system center of mass, rotational motion also causes acceleration of the accelerometer. This is demonstrated by Figure (5.1) which illustrates a rotating rigid body. The point p is rigidly attached to the body, and is assumed to be located on the body-fixed z axis. This is similar to the physical position of the IMU in the ducted-fan system. Note that the position of the IMU expressed in the inertial frame of reference is given by

$$p_s = p_{CM} + {}^o_bRd\hat{z} \tag{5.4}$$

as a function of the position of the system center of mass p_{CM}. The velocity and acceleration of the IMU due to the system linear translation and rotational movement is given by

$$v_s = v_{CM} + {}^o_bRS\left(\Omega_b\right)d\hat{z} \tag{5.5}$$

$$\dot{v}_s = \dot{v}_{CM} + {}^o_bRS\left(\Omega_b\right)^2 d\hat{z} + {}^o_bRS\left(\dot{\Omega}_b\right)d\hat{z} \tag{5.6}$$

Since the rotation matrix now gives the transformation from the body-fixed frame to the inertial frame, the time derivative is now expressed by ${}^o_b\dot{R} = {}^o_bRS\left(\Omega\right)$. Equation (5.6) contains three terms which contribute to the acceleration of the IMU. The first term is the acceleration due to the linear translation of the system, and the second and third term are known as the centripetal and transverse accelerations, respectively. These accelerations all affect the quality of the accelerometer signals. To reduce the effect of the transverse and centrifugal forces, it is desirable to place the accelerometer as close as possible to the system center of mass. Often, approximations are made which assume that system accelerations are small. Under these conditions in addition to knowledge of the accelerometer bias through measurement and neglecting noise, a simplified model of the accelerometer signal is given by

$$y = {}^b_oR\hat{z} \tag{5.7}$$

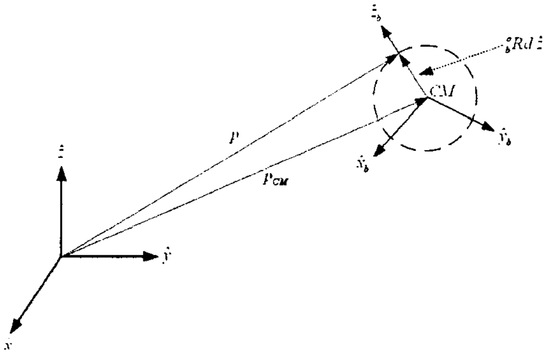

Figure 5.1: Rotating Rigid Body

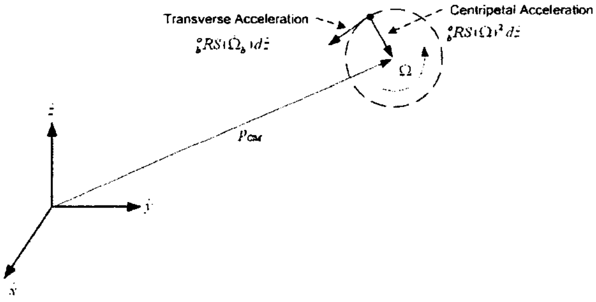

Figure 5.2: Acceleration due to Rotation

5.3 Magnetometers

Since accelerometers can only obtain the pitch and roll of the system, an additional vector observation must be obtained which is orthogonal to the gravity vector. Since the earth's magnetic field has a component which is orthogonal to the gravity vector, it can be used to obtain a measurement for the system yaw, ψ. Unlike the accelerometers, the magnetometers are not affected by system forces. They are, however, affected by magnetic fields which are created due to the electric current supplied to system electronics or electric motors, as well as other magnetic fields created by environmental surroundings such as buildings. The quality of the magnetometer signals can be improved by measuring the relationship between the motor control effort and the resulting perturbing magnetic field. This value can be subsequently removed from the sensor measurements. However, the magnetometer signals tend to be noisy in nature which deteriorates measurement reliability. A magnetometer model is given by

$$m = {}^b_oRh + f\left(T\right) + b_m + n_m \tag{5.8}$$

which is given as a function of sensor bias b_m, sensor noise n_m, the surrounding environmental magnetic field h, and the effect due to the electric motors $f\left(T\right)$. Similar to the accelerometer, by measuring and removing the sensor bias and effect due to electric motors and neglecting noise, a simplified model is given where h is the magnetic field of the surrounding environment by

$$m = {}^b_oRh \tag{5.9}$$

5.3.1 Angular Velocity and the Euler Angles

Since Euler-Angles are often used to represent aircraft orientation, a method shown by equations 5.10 and 5.11 was presented in [21] which shows the relationship between the $3-2-1$ asymmetric set of Euler angles and the body-reference angular velocity. Since $|E| = \cos\theta$ it is clear that a singularity exists when $\theta = \pi/2$.

$$\Omega \;=\; E\begin{pmatrix} \dot{\phi} \\ \dot{\theta} \\ \dot{\psi} \end{pmatrix} \tag{5.10}$$

$$E = \begin{pmatrix} 1 & 0 & -\sin\theta \\ 0 & \cos\phi & \sin\phi\cos\theta \\ 0 & -\sin\phi & \cos\phi\cos\theta \end{pmatrix} \tag{5.11}$$

$$E^{-1} = \left(\frac{1}{\cos\theta}\right)\begin{pmatrix} \cos\theta & \sin\phi\sin\theta & \cos\phi\sin\theta \\ 0 & \cos\phi\cos\theta & -\sin\phi\cos\theta \\ 0 & \sin\phi & \cos\phi \end{pmatrix} \tag{5.12}$$

Provided that $\theta \neq \pi/2$, the euler angles can be obtained from integration of the angular velocity and the transformation given by E.

5.4 Attitude Estimation from Vector Observations

Due to the problems associated with attitude estimation using the gyroscope signals, it is advantageous to obtain a method for attitude determination which does not involve the integration of flawed signals. Using the accelerometers and magnetometers body referenced vector observations of the earth's gravity and magnetic field can be used to provide estimates of the system attitude.

Consider the simplified model of the accelerometer signal. From here, it is assumed that the magnetometer and accelerometer signals are normalized, or $\|m\| = \|y\| = 1$. In light of (3.73), the accelerometer can be used to obtain estimates of two of the three Euler Angles,

$$y = R\hat{z} = \begin{pmatrix} -\sin\theta \\ \sin\phi\cos\theta \\ \cos\phi\cos\theta \end{pmatrix} \tag{5.13}$$

$$\theta = -\arcsin y_1 \tag{5.14}$$

$$\phi = \arctan 2\,(y_2, y_3) \tag{5.15}$$

where arctan 2 is the four-quadrant arctangent. To obtain the third Euler angle the magnetometer is used. In general, the surrounding magnetic field will have a vertical component and a horizontal component which is tangent to the earth's surface. Arbitrarily it can be assumed that the horizontal component of the magnetic field is aligned with the inertial x axis, then we can say that $h \in span\,(x, y)$, or $h = (h_x,\ 0,\ h_z)$. In the body-fixed frame the magnetic field vector is expressed as

$$Rh = h_x \begin{pmatrix} R_{11} \\ R_{21} \\ R_{31} \end{pmatrix} + h_z y \tag{5.16}$$

Using this result, if the values of the magnetic field are known, the first column of the rotation matrix can be obtained. Since the value of the surrounding magnetic field may not be known, or may change if the system is placed in a different environment, an algorithm which does not require knowledge of the magnetic field is desired. This type of algorithm, which was investigated by [18], uses Gram-Schmidt orthonormalization. Using this method, the component of the magnetometer signal which is parallel to the accelerometer signal is obtained. Recall equation (5.17), which gives the component of v which is parallel to u. From (5.17), the vertical component of the magnetic field can be found, as follows

$$v_{\parallel}(u) = \frac{u^T v u}{\|u\|} \tag{5.17}$$

$$y^T m = h_z \tag{5.18}$$

By removing the component of the magnetometer signal which is parallel to the accelerometer signal and normalizing, the first column of the rotation matrix is obtained. The second column of the rotation matrix is then obtained by taking the vector cross product of the third and first column, as shown by (5.19), since $y \times \alpha y = 0$ where $\alpha \in R$. From the relationship between the rotation matrix and the Euler angles, the third angle is obtained by

$$ {}^b_o\bar{R} = \begin{pmatrix} \frac{m - y^T m y}{\|m - y^T m y\|} & \frac{y \times m}{\|m - y^T m y\|} & y \end{pmatrix} \tag{5.19}$$

$$\psi = \arctan 2\left(R_{12}, R_{11}\right) \tag{5.20}$$

Finally, the quaternion $\bar{Q}$ is obtained from the euler angles using

$$\bar{Q} = \begin{pmatrix} c_{\phi/2}c_{\theta/2}c_{\psi/2} + s_{\phi/2}s_{\theta/2}s_{\psi/2} \\ s_{\phi/2}c_{\theta/2}c_{\psi/2} - c_{\phi/2}s_{\theta/2}s_{\psi/2} \\ c_{\phi/2}s_{\theta/2}c_{\psi/2} + s_{\phi/2}c_{\theta/2}s_{\psi/2} \\ c_{\phi/2}c_{\theta/2}s_{\psi/2} - s_{\phi/2}s_{\theta/2}c_{\psi/2} \end{pmatrix} \tag{5.21}$$

5.5 Estimation Algorithms

In [27], different estimation algorithms are presented which combine the gyroscope signals with the accelerometers and magnetometers. The first algorithm requires the knowledge of the actual system attitude through Q which is not ideal. Algorithms 2 and 3 provide estimates for the gyroscope bias using measurements obtained with low-pass sensors. If an estimator is developed where $\lim_{t\to\infty} \hat{b} = b$, then at some point the gyroscope signal becomes more accurate, resulting in improved attitude estimates from integration of the gyroscope signals. However, due to the nonlinearities associated with the system, obtaining the bias alone does not guarantee convergence of the attitude estimates to the actual attitude. Therefore, in addition to the bias estimate, an additional input to the attitude observer is required to guarantee convergence. One approach to this problem involves complementary filtering of the gyroscope, accelerometer, and magnetometer signals. The complementary filter approach is suitable since the gyroscope signal is reliable at high frequencies, since the gyro bias has a constant value, and the accelerometer and magnetometer signals are reliable at low frequencies, when the system accelerations are small. Still, the complementary filter is enhanced due to estimation algorithms 2 and 3.

5.5.1 Algorithm 1

A bias and attitude observer is proposed in [27], which uses the gyroscope measurements in addition to the quaternion. Consider the following estimator

$$\begin{aligned}\dot{\hat{Q}} &= \tfrac{1}{2}\hat{Q}\odot Q_\beta \\ \beta &= \Omega_g - \hat{b} + \Gamma_1\tilde{q} \\ \dot{\hat{b}} &= -\Gamma_2\tilde{q}\end{aligned} \tag{5.22}$$

where $\Gamma_{\{1,2\}} = \Gamma_{\{1,2\}}^T > 0$, $Q_\beta = (0,\ \beta)$, $\Omega_g = \Omega + b$, and

$$\tilde{Q} = \begin{pmatrix} \tilde{q}_o \\ \tilde{q} \end{pmatrix} = \hat{Q}^{-1}\odot Q \tag{5.23}$$

then $\lim\limits_{t\to\infty} \hat{b} = b$ and $\lim\limits_{t\to\infty} \hat{Q} = Q$.

Proof: Consider the following Lyapunov function candidate

$$\begin{aligned}V &= (1-\tilde{q}_o)^2 + \tilde{q}^T\tilde{q} + \tfrac{1}{2}\tilde{b}^T\Gamma_2^{-1}\tilde{b} \\ &= 2\,(1-\tilde{q}_o) + \tfrac{1}{2}\tilde{b}^T\Gamma_2^{-1}\tilde{b}\end{aligned} \tag{5.24}$$

where $\tilde{b} = \hat{b} - b$ and the gyroscope bias is assumed to be varying slowly with time, or $\dot{b} \approx 0$. The derivative with respect to time of 5.24 is then given by

$$\dot{V} = -2\dot{\tilde{q}}_o + \tilde{b}^T\Gamma_2^{-1}\dot{\tilde{b}} \tag{5.25}$$

Given that $\hat{Q} = {}^b_o\hat{Q}$, then $\hat{Q}^{-1} = {}^o_bQ$. The required time derivative of $\tilde{Q}$ can be derived from (3.112).

$$\tfrac{d}{dt}\hat{Q}^{-1} = -\tfrac{1}{2}Q_\beta\odot\hat{Q}^{-1} \tag{5.26}$$

$$\begin{aligned}\dot{\tilde{Q}} &= \dot{\hat{Q}}^{-1}\odot Q + \hat{Q}^{-1}\odot\dot{Q} \\ &= \tfrac{1}{2}\begin{pmatrix} \tilde{q}^T(\beta-\Omega) \\ \tilde{q}_o(\Omega-\beta) + S(\tilde{q})(\Omega+\beta)\end{pmatrix}\end{aligned} \tag{5.27}$$

In light of (5.27), the time derivative of the Lyapunov function is given by (5.28). Under the estimation law given by (5.22), we obtain

$$\dot{V} = -\tilde{q}^T(\beta - \Omega_g + b) + \tilde{b}^T\Gamma_2^{-1}\dot{\hat{b}} \tag{5.28}$$

$$\dot{V} = -\tilde{q}^T\Gamma_1\tilde{q} \tag{5.29}$$

From (5.29) we can conclude that $\tilde{q}_o$, $\tilde{q}$ and $\tilde{b}$ are bounded. To show that (5.29) is uniformly continuous a sufficient and necessary condition is that it's derivative is bounded. Consider the second derivative of the Lyapunov function given by

$$\ddot{V} = -\Gamma_1\left(S(\tilde{q})\left(2\Omega - \tilde{b} + \Gamma_2\tilde{q}\right) - \tilde{q}_o\left(\tilde{b} + \Gamma_2\tilde{q}\right)\right) \tag{5.30}$$

Since we know $\tilde{q}_o$, $\tilde{q}$, and $\hat{b}$ are bounded, and we assume Ω to be bounded, then (5.30) is also bounded, and hence invoking Barbalat's lemma, one can conclude that $\lim\limits_{t\to\infty}\tilde{q} = 0$. This implies that $\lim\limits_{t\to\infty}\tilde{q}_o = \pm 1$. Also, since $\ddot{\tilde{Q}}$ is bounded, then $\lim\limits_{t\to\infty} \dot{\tilde{Q}} = 0$, which implies that $\lim\limits_{t\to\infty} \Omega = \beta$. Therefore, $\lim\limits_{t\to\infty} \hat{b} = b$, and the bias observer converges to the actual value of the gyroscope bias.

In practice since the actual quaterion Q is not available, if the system accelerations are small, or $\bar{Q} \approx Q$, then the above estimator can be implemented where $\tilde{Q} = \hat{Q}^{-1} \odot \bar{Q}$. Under the above estimation law, the estimate $\hat{Q}$ will converge to the quaternion obtained from vector measurements. When the system accelerations are small, then $\bar{Q} \approx Q$, and the attitude observer converges to the actual attitude.

5.5.2 Algorithm 2

Previously, it was assumed that the quaternion obtained from vector observations is ideal, when actually these measurements are affected by noise, system accelerations and dynamics attributed to the low pass characteristics of the sensors. In addition to the physical limitations on sensor bandwidth, low-pass filters are often implemented in hardware or software for noise filtering. To include these dynamics in the attitude estimates from vector observations, consider (5.31), where the traditional equation for the quaternion derivative is given. To model the low-pass dynamics, the following model is used by [27]

$$\dot{\bar{Q}} = \tfrac{1}{2}\bar{Q} \odot \bar{\Omega} \tag{5.31}$$

where $\bar{\Omega}$ is given by

$$\dot{\bar{\Omega}} = -A\bar{\Omega} + A\Omega \tag{5.32}$$

From (5.31) we can obtain the *virtual* angular velocity as follows

$$\bar{\Omega} = 2\bar{Q}^{-1} \odot \dot{\bar{Q}} \tag{5.33}$$

where $[\dot{\bar{Q}}] = s[Q]$. In practice $\dot{\bar{Q}}$ can be obtained from $\bar{Q}$ using the following filtered derivative

$$\dot{\bar{Q}}(s) \approx \frac{s}{\tau s + 1}\bar{Q} \tag{5.34}$$

As shown in [27], an observer for gyroscope bias is given by

$$\dot{\hat{\bar{\Omega}}} = -A\hat{\bar{\Omega}} + A\left(\Omega_g - \hat{b}\right) \tag{5.35}$$

$$\dot{\hat{b}} = -\Gamma\tilde{\Omega} \tag{5.36}$$

$$\tilde{\Omega} = \bar{\Omega} - \hat{\bar{\Omega}} \tag{5.37}$$

Using this estimation law, it can be shown that $\lim\limits_{t\to\infty} \tilde{b} = 0$, and $\lim\limits_{t\to\infty} \tilde{\Omega} = 0$.

Proof: Consider the following Lyapunov candidate

$$V = \tfrac{1}{2}\tilde{b}^T\Gamma^{-1}\tilde{b} + \tfrac{1}{2}\tilde{\Omega}^T A^{-1}\tilde{\Omega} \tag{5.38}$$

where

$$\tilde{b} \;=\; \hat{b} - b \tag{5.39}$$

The time derivative of the Lyapunov candidate is then given by

$$\dot{V} \;=\; \tilde{b}^T\Gamma^{-1}\dot{\hat{b}} + \tilde{\Omega}^T A^{-1}\dot{\tilde{\Omega}} \tag{5.40}$$

Taking the time derivative of (5.37) we obtain

$$\dot{\tilde{\Omega}} \;=\; -A\tilde{\Omega} + A\tilde{b} \tag{5.41}$$

Hence

$$\dot{V} \;=\; \tilde{b}^T\Gamma^{-1}\dot{\hat{b}} - \tilde{\Omega}^T\tilde{\Omega} + \tilde{\Omega}^T\tilde{b} \tag{5.42}$$

From the estimation law given by (5.36)

$$\dot{V} \;=\; \tilde{\Omega}^T\left(\Omega_g - \hat{b} - \bar{\Omega} - A^{-1}\dot{\hat{\bar{\Omega}}}\right) \tag{5.43}$$

$$\dot{V} \;=\; -\tilde{\Omega}^T\tilde{\Omega} \tag{5.44}$$

which implies that $\tilde{b}$ and $\tilde{\Omega}$ are both bounded. Furthermore, since $\ddot{\tilde{\Omega}}$ is bounded then $\lim\limits_{t\to\infty}\dot{\tilde{\Omega}} = 0$ which implies that $\lim\limits_{t\to\infty}\tilde{b} = 0$.

5.5.3 Algorithm 3

In the case where the dynamics given by A are unknown, the following estimator has been proposed in [27]

$$\dot{\hat{\bar{\Omega}}} \;=\; -\bar{A}\hat{\bar{\Omega}} + \bar{A}\left(\Omega_g - \hat{b}\right) + M\left(t\right)\hat{\theta} \tag{5.45}$$

$$\dot{\hat{b}} \;=\; -\Gamma\tilde{\Omega} \tag{5.46}$$

$$\dot{\hat{\theta}} \;=\; \bar{\Gamma}M(t)\tilde{\Omega} \tag{5.47}$$

where $\tilde{\Omega} = \bar{\Omega} - \hat{\bar{\Omega}}$ and

$$M(t) \;=\; diag\left(m_1 \quad m_2 \quad m_3\right)^T \tag{5.48}$$

where the vector

$$m = \left(m_1 \quad m_2 \quad m_3\right)^T = \Omega_g - \hat{\bar{\Omega}} - \hat{b} \tag{5.49}$$

Provided a persistency of excitation condition is satisfied it can be shown that $\tilde{\Omega}$, $\tilde{b}$, and $\tilde{\theta}$ converge exponentially to zero.

Proof: Consider the following Lyapunov function candidate

$$V = \tfrac{1}{2}\tilde{b}^T A\Gamma^{-1}\tilde{b} + \tfrac{1}{2}\tilde{\theta}^T\bar{\Gamma}^{-1}\tilde{\theta} + \tfrac{1}{2}\tilde{\Omega}^T\tilde{\Omega} \tag{5.50}$$

Also, $\tilde{b} = \hat{b} - b$ and $\tilde{\theta} = \hat{\theta} - \theta$, where the vector θ contains the diagonal components of the matrix

$$\Delta A = A - \bar{A} \tag{5.51}$$

The time derivative of the above Lyapunov function is then given by

$$\dot{V} = \tilde{b}^T A\Gamma^{-1}\dot{\tilde{b}} + \tilde{\theta}^T\bar{\Gamma}^{-1}\dot{\tilde{\theta}} + \tilde{\Omega}^T\dot{\tilde{\Omega}} \tag{5.52}$$

Since we assume that the gyro bias as well as A and $\bar{A}$ are constant, then $\dot{b} = 0$ and $\dot{\theta} = 0$, and in light of (5.41) the Lyapunov time derivative becomes

$$\begin{aligned} \dot{V} = {} & \left(\hat{b} - b\right)^T A\Gamma^{-1}\dot{\hat{b}} - b^T A\tilde{\Omega} \\ & + \tilde{\theta}^T\bar{\Gamma}^{-1}\dot{\hat{\theta}} + \tilde{\Omega}^T\left(A\Omega_g - A\bar{\Omega} - \dot{\hat{\bar{\Omega}}}\right) \end{aligned} \tag{5.53}$$

which is simplified in light of (5.45) and (5.46) to obtain

$$\dot{V} = -\tilde{\Omega}^T\bar{A}\tilde{\Omega} \tag{5.54}$$

From (5.54) we can conclude that $\tilde{b}$, $\tilde{\theta}$, and $\tilde{\Omega}$ are bounded. Furthermore, if the persistency of excitation condition (32) in [27] is satisfied, then $\tilde{b}$, $\tilde{\theta}$, and $\tilde{\Omega}$ converge exponentially to zero. As a result we can conclude that $\lim_{t\to\infty}\hat{\bar{\Omega}} = \bar{\Omega}$, $\lim_{t\to\infty}\hat{b} = b$ and $\lim_{t\to\infty}\hat{\theta} = \theta$, (see [27] for proof).

5.5.4 Complementary Filter

In order to implement the gyroscope signals in addition to the accelerometers and magnetometers, a complementary filter can be used to fuse the signals together to obtain accurate estimates of the system attitude, [27]. Since the gyroscope bias is a constant value, the signal is more reliable at high frequencies. When the system accelerations are small, then the accelerometers are more accurate in measuring the direction of gravity. Therefore, it is desirable to obtain the low-frequency components of the quaternion $\bar{Q}$, since $\bar{Q} \approx Q$ at low frequencies and low system accelerations. To determine a suitable input for the low-pass portion of the complementary filter, consider the Lyapunov function candidate given by

$$\begin{aligned} V &= (1 - q_o)^2 + \tilde{q}^T\tilde{q} \\ &= 2\left(1 - \tilde{q}_o\right) \end{aligned} \tag{5.55}$$

where

$$\begin{aligned} \tilde{Q} &= (\tilde{q}_o,\ \tilde{q}) \\ &= \hat{Q}^{-1} \odot \bar{Q} \end{aligned} \tag{5.56}$$

The time derivative of (5.55) is given by

$$\begin{aligned} \dot{V} &= -2\dot{\tilde{q}}_o \\ &= -\tilde{q}^T\left(\beta - \bar{\Omega}\right) \end{aligned} \tag{5.57}$$

since

$$\dot{\tilde{q}}_o = \tfrac{1}{2}\tilde{q}^T(\beta - \bar{\Omega})$$

In light of (5.57) choosing $\beta = \bar{\Omega} + \Gamma\tilde{q}$ where $\Gamma > 0$, a negative definite result is given by

$$\dot{V} = -\tilde{q}^T\Gamma\tilde{q} \tag{5.58}$$

Since $\ddot{V}$ is bounded, then we can conclude that $\lim_{t\to\infty} \tilde{q} = 0$. Using this topology, an attitude observer is given by (5.59) and (5.60) which uses a complementary filter, where $F_1(s) + F_2(s) = 1$. Furthermore, rather than estimating the quaternion directly, the input to the observer is the virtual angular velocity corresponding to $\hat{Q}$. This ensures that the unit-norm constraint of the quaternion is always satisfied.

$$\dot{\hat{Q}} = \tfrac{1}{2}\hat{Q} \odot Q_\beta \tag{5.59}$$

$$\beta = F_1\left(\Omega_g - \hat{b}\right) + F_2\left(\bar{\Omega} + \Gamma\tilde{q}\right) \tag{5.60}$$

The filters F_1 and F_2 are second order filters of the form

$$F_1(s) = \frac{s^2 + 2\xi\omega_n s}{s^2 + 2\xi\omega_n s + \omega_n^2} \tag{5.61}$$

$$F_2(s) = \frac{\omega_n^2}{s^2 + 2\xi\omega_n s + \omega_n^2} \tag{5.62}$$

where the filter damping ratio is chosen as $\xi = 2^{-1/2}$ and ω_n is the cutoff frequency of the filters.

Chapter 6

Control Design

For attitude stabilization the primary challenge is obtaining accurate estimates of the system attitude. Provided that these estimates are accurate, then a PD type of control can be implemented to stabilize the aircraft. It is well known that many mechanical systems can be controlled using this type of feedback. Other authors have included the compensation of other system dynamics, (for example gyroscopic torques [26], or the inertia tensor [25]). Including these compensating terms can improve the overall performance of the system, yet is not a necessary condition for system stability. Also, in practice, simple control laws are sometimes preferred over the implementation of complex feedback. For the PD control, the input to the proportional feedback is the vector part of the quaternion, where the input to the derivative feedback is the system angular velocity.

6.1 Set-Point Control

A set-point type of control is implemented to allow a pilot to specify a desired system attitude. The feedback control then acts to stabilize the system to the desired attitude. This allows the aircraft to be directed by a pilot while the aircraft performs the necessary stabilizing action. Therefore, a new quaternion defined as the *error* quaternion describes the difference between the desired attitude and the estimated attitude, as given by

$$\begin{aligned} Q^e &:= (q_{eo},\, q_e) \\ &= \left(Q^d\right)^{-1} \odot \hat{Q} \end{aligned} \tag{6.1}$$

where the desired quaternion

$$Q^d = \begin{pmatrix} q_{do} \\ q_d \end{pmatrix} \tag{6.2}$$

is obtained using (3.83) from the pilot specified Euler angles given by

$$\eta_d = \begin{pmatrix} \phi_d & \theta_d & \psi_d \end{pmatrix}^T \tag{6.3}$$

To determine the control input consider the Lypaunov function candidate

$$\begin{aligned} V &= \alpha\left(q_e^T q_e + (q_{eo}-1)^2\right) + \tfrac{1}{2}\Omega^T I_b \Omega \\ &= 2\alpha(1-q_{eo}) + \tfrac{1}{2}\Omega^T I_b \Omega \end{aligned} \tag{6.4}$$

$$\dot{V} = -2\alpha\dot{q}_{eo} + \Omega^T I_b \dot{\Omega} \tag{6.5}$$

For this system the set-point input is assumed to be a constant value resulting in the derivative of the error quaternion given by (6.6). For tracking controllers, see [29] and [25]. Also, assume the general dynamic equation of a rigid body given by (6.7).

$$\dot{q}_{eo} = -q_e^T \Omega \tag{6.6}$$

$$I_b\dot{\Omega} = -\Omega \times I_b \Omega + \tau \tag{6.7}$$

$$\dot{V} = q_e^T \Omega + \Omega^T \tau \tag{6.8}$$

Using the given control law the Lyapunov time derivative becomes

$$\tau = -\alpha q_e - \Gamma\Omega \tag{6.9}$$

$$\dot{V} = -\Omega^T \Gamma \Omega \tag{6.10}$$

6.2 PD Control

Since an observer is implemented for the gyroscope bias, the controller previously mentioned can be improved by removing the estimated gyro bias from the velocity measurement.

$$\tau = -\alpha q_e - \Gamma\left(\Omega_g - \hat{b}\right) \tag{6.11}$$

The feedback structure is shown in Figure (8.14), where ω and γ are the desired angular velocity for the two motors and the desired servo angle, respectively.

6.3 Desired Yaw Implementation

The pilot input contains four independent channels. Two of these channels are used for the desired roll and pitch, where a third channel is used for the desired throttle. The fourth channel is used as an input for the yaw. When the pilot joysticks are centered, a null value is used for the desired pitch and roll. However, it may be desired to operate the aircraft with a yaw position other than the null position. For example, if we desire the aircraft to point in a certain fixed direction other than the null direction due to the surrounding magnetic field, it is not desirable for the pilot to constantly send the desired yaw signal. As as result, the desired yaw is obtained by integrating the pilot input signal using the following differential equation

$$\dot{R}_{\psi_d} = -S\left(\Omega_\psi\right) R_{\psi_d} \tag{6.12}$$

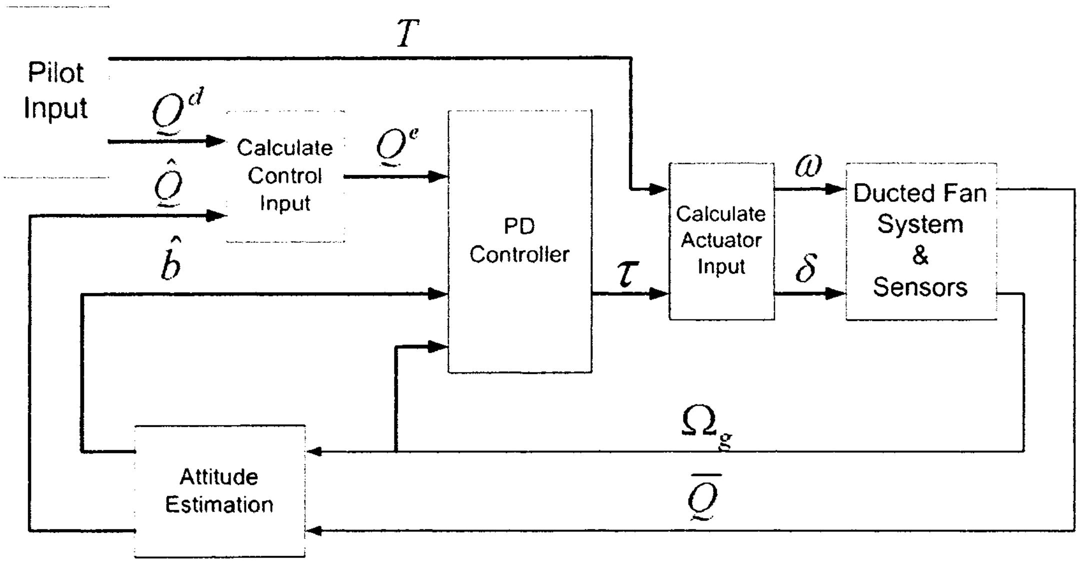

Figure 6.1: Feedback Control Block Diagram

where

$$\Omega_\psi = (0 \quad 0 \quad u)^T \tag{6.13}$$

To avoid drift, a dead-zone is applied to the pilot input

$$u = \begin{cases} 0 & |u| < k \\ u & |u| \geq k \end{cases} \tag{6.14}$$

Due to the nature of the direct cosine matrix, the resulting desired yaw signal will be bounded for any pilot input signal. Furthermore, the signal also contains *wrapping* characteristics when extracting the desired yaw Euler angle from the rotation matrix (see appendix), or $-\pi \leq \psi \leq \pi$. For example, the aircraft could rotate about the yaw axis indefinitely without causing saturation of the yaw signal.

Chapter 7

Simulations

7.1 Ideal Model

A series of simulations are performed for the three algorithms using an ideal system model. A PD controller is implemented for the attitude stabilization.

Ideal System Model:

$$\dot{Q} = \frac{1}{2} Q \odot Q_{\Omega} \tag{7.1}$$

$$I_b \dot{\Omega} = -I_b \times I_b \Omega + \tau \tag{7.2}$$

Set-Point Control:

$$\tau = -\alpha q_e - \Gamma \left(\Omega_g - \hat{b} \right) \tag{7.3}$$

$$Q^e = \left(Q^d \right)^{-1} \odot \hat{Q} \tag{7.4}$$

Sensor Model:

$$\dot{\bar{Q}} = \frac{1}{2} \bar{Q} \odot Q_{\bar{\Omega}} \tag{7.5}$$

$$\dot{\bar{\Omega}} = -A\bar{\Omega} + A\Omega \tag{7.6}$$

$$\Omega_g = \Omega + b \tag{7.7}$$

$$\dot{\hat{Q}} = \frac{1}{2} \hat{Q} \odot Q_{\beta} \tag{7.8}$$

$$\beta = \Omega_g - \hat{b} + \Gamma_1 \tilde{q} \tag{7.9}$$

$$\dot{\hat{b}} = -\Gamma_2 \tilde{q} \tag{7.10}$$

$$\tilde{Q} = \hat{Q}^{-1} \odot \bar{Q} \tag{7.11}$$

Parameter	Value
Low Pass Filter Characteristics	$A = 20\pi I_{3\times3}$
Proportional Control Gain	$\alpha = 20$
Derivative Control Gain	$\Gamma = 5$
Attitude Initial Conditions	$Q(0) = Q_I$
Gyroscope Bias	$b = (0.5,\ -1.5,\ 1)\,\mathrm{deg}/s$
Desired Attitude	$\eta_d = (10,\ -10,\ 30)\,\mathrm{deg}\quad @\ t = 2s$
System Inertia Tensor	$I_b = \begin{pmatrix} 0.5 & 0 & 0 \\ 0 & 0.5 & 0 \\ 0 & 0 & 0.25 \end{pmatrix}$
Complementary Filter Dampening Ratio	$\psi = 2^{-1/2}$
Complementary Filter Cutoff Frequency	$\omega_n = 2\pi\ (1\ \mathrm{Hz})$

Table 7.1: System Simulation Parameters

Parameter	Value
Initial Conditions	$\hat{Q}(0) = Q_I$
	$\hat{b}(0) = 0_{3\times1}$
Observer Gains	$\Gamma_1 = 5I_{3\times3}$
	$\Gamma_2 = 10I_{3\times3}$

Table 7.2: Algorithm 1 Simulation Parameters

7.1.1 Algorithm 2

The bias and angular velocity observer outlined in algorithm 2 are used with a complementary filter to develop estimates of the system attitude. The bias and attitude estimates are used by the PD controller, as previously mentioned.

Observer:

$$\dot{\hat{\bar{\Omega}}} = -A\hat{\bar{\Omega}} + A\left(\Omega_g - \hat{b}\right) \tag{7.12}$$

$$\dot{\hat{b}} = -\Gamma_1\tilde{\Omega} \tag{7.13}$$

$$\tilde{\Omega} = \bar{\Omega} - \hat{\bar{\Omega}} \tag{7.14}$$

Filtered Derivative:

$$\dot{\bar{Q}}(s) = \frac{s}{\tau_f s + 1}\bar{Q} \tag{7.15}$$

$$\bar{\Omega} = 2\bar{Q}^{-1} \odot \dot{\bar{Q}} \tag{7.16}$$

Complementary Filter:

$$
\begin{aligned}
\dot{\hat{Q}} &= \frac{1}{2}\hat{Q} \odot Q_\beta && (7.17)\\
\beta(s) &= F_1(s)\left(\Omega_g - \hat{b}\right) + F_2(s)\left(\bar{\Omega} + \Gamma_2\tilde{q}\right) && (7.18)\\
\tilde{Q} &= \hat{Q}^{-1} \odot \bar{Q} && (7.19)\\
& && (7.20)
\end{aligned}
$$

Parameter	Value
Initial Conditions	$\hat{Q}(0) = Q_I$ $\hat{b}(0) = \mathbf{0}_{3\times1}$ $\hat{\bar{\Omega}}(0) = \mathbf{0}_{3\times1}$
Observer Gains	$\Gamma_1 = I_{3\times3}$ $\Gamma_2 = 0.5I_{3\times3}$
Filtered Derivative Time Constant	$\tau_f = 0.01$

Table 7.3: Algorithm 2 Simulation Parameters

Observer:

$$
\begin{aligned}
\dot{\hat{\bar{\Omega}}} &= -\bar{A}\hat{\bar{\Omega}} + \bar{A}\left(\Omega_g - \hat{b}\right) + M(t)\tilde{\Omega} && (7.21)\\
\dot{\hat{b}} &= -\Gamma_1\tilde{\Omega} && (7.22)\\
\dot{\hat{\theta}} &= \bar{\Gamma}M(t)\tilde{\Omega} && (7.23)\\
\tilde{\Omega} &= \bar{\Omega} - \hat{\bar{\Omega}} && (7.24)\\
M(t) &= diag\left(m_1,\ m_2,\ m_3\right) && (7.25)\\
& && (7.26)
\end{aligned}
$$

where

$$\Omega_g - \hat{\bar{\Omega}} - \hat{b} = (m_1,\ m_2,\ m_3) \qquad (7.27)$$

7.2 Effect of Linear Accelerations

A simulation is performed to show how the linear accelerations can negatively affect the attitude estimates. The linear accelerations directly affect the accelerometer signal by the following

$$y = \frac{R\left(g\hat{z} - \dot{v}\right)}{\left\|R\left(g\hat{z} - \dot{v}\right)\right\|} \qquad (7.28)$$

Parameter	Value
Initial Conditions	$\hat{Q}(0) = Q_I$ $\hat{b}(0) = \mathbf{0}_{3\times 1}$ $\hat{\bar{\Omega}}(0) = \mathbf{0}_{3\times 1}$ $\hat{\theta}(0) = \mathbf{0}_{3\times 1}$
Observer Gains	$\Gamma_1 = 2I_{3\times 3}$ $\Gamma_2 = 0.5I_{3\times 3}$ $\bar{\Gamma} = 50I_{3\times 3}$ $\bar{A} = 5I_{3\times 3}$

Table 7.4: Algorithm 3 Simulation Parameters

where $\dot{v}$ is the inertial-referenced system acceleration. The previous description of the system aerodynamic drag is an under-prediction of the actual aerodynamic forces acting on the system. However, without performing wind-tunnel tests, it is very difficult to accurately describe these aerodynamic forces. Since the system aerodynamic drag helps to reduce system accelerations, an under-prediction leads to simulation results where the system is difficult to stabilize. In the absence of an accurate aerodynamic model, the ratio k of the system acceleration is applied to the accelerometer

$$y = \frac{R\left(g\hat{z} - k\dot{v}\right)}{\left\|R\left(g\hat{z} - k\dot{v}\right)\right\|} \tag{7.29}$$

Since the system yaw dynamics are different from the pitch and roll, it was useful to have the ability to have a different value of proportional gain. Although, the theory suggests that the proportional gain should be a constant, simulation and experimental results both proved that system stability could be improved by using different values of proportional gain for the three different elements of the quaternion making α a 3×3 matrix. In an attempt to keep the system accelerations small, the set-point control input was applied through a first-order low-pass filter with a cut-off frequency of $f = 0.05$Hz.

Parameter	Value
Initial Conditions	$\hat{Q}(0) = Q_I$ $\hat{b}(0) = \mathbf{0}_{3\times 1}$
Observer Gains	$\Gamma_1 = 2I_{3\times 3}$ $\Gamma_2 = 0.1I_{3\times 3}$
Proportional Control Gain	$\alpha = 20$
Derivative Control Gain	$\Gamma = \begin{pmatrix} 4 & 0 & 0 \\ 0 & 4 & 0 \\ 0 & 0 & 8 \end{pmatrix}$

Table 7.5: Algorithm 1 With Linear Acceleration Simulation Parameters

Parameter	Value
Initial Conditions	$\hat{Q}(0) = Q_I$ $\hat{b}(0) = \mathbf{0}_{3\times 1}$ $\hat{\Omega}(0) = \mathbf{0}_{3\times 1}$
Observer Gains	$\Gamma_1 = \begin{pmatrix} 0.4 & 0 & 0 \\ 0 & 0.4 & 0 \\ 0 & 0 & 0.04 \end{pmatrix}$ $\Gamma_2 = \begin{pmatrix} 0.5 & 0 & 0 \\ 0 & 0.5 & 0 \\ 0 & 0 & 2.5 \end{pmatrix}$
Proportional Control Gain	$\alpha = \begin{pmatrix} 20 & 0 & 0 \\ 0 & 20 & 0 \\ 0 & 0 & 1 \end{pmatrix}$
Derivative Control Gain	$\Gamma = \begin{pmatrix} 4 & 0 & 0 \\ 0 & 4 & 0 \\ 0 & 0 & 8 \end{pmatrix}$
Filtered Derivative Time Constant	$\tau_f = 0.02$

Table 7.6: Algorithm 2 With Linear Acceleration Simulation Parameters

7.2.1 Discussion

Figures (7.1) through (7.13) demonstrate that all of the algorithms result in a stable closed loop system under ideal conditions. For algorithms 1 and 2, the simulations show that the resulting system attitude for the closed loop system is overdamped, where the results for algorithm 3 show a slightly underdamped system. Since the bias estimate is included in the velocity portion of the PD controller, the bias observer gain can have an effect on the closed loop performance. Figure (7.10) shows a larger deviation of the bias estimates which contributes to the overshoot of the system attitude for algorithm 3. Figures (7.14) through (7.33) show the negative effect of linear accelerations on the attitude estimates. Although in simulation the linear acceleration was attenuated by a factor of 0.5, this value can be increased by obtaining a more accurate model of the system aerodynamic drag.

Parameter	Value
Initial Conditions	$\hat{Q}(0) = Q_I$ $\hat{b}(0) = \mathbf{0}_{3\times1}$ $\hat{\bar{\Omega}}(0) = \mathbf{0}_{3\times1}$ $\hat{\theta}(0) = \mathbf{0}_{3\times1}$
Observer Gains	$\Gamma_1 = 0.1I_{3\times3}$ $\bar{A} = 0.1I_{3\times3}$ $\bar{\Gamma} = 0.5I_{3\times3}$ $\Gamma_2 = \begin{pmatrix} 0.5 & 0 & 0 \\ 0 & 0.5 & 0 \\ 0 & 0 & 2.5 \end{pmatrix}$
Proportional Control Gain	$\alpha = \begin{pmatrix} 20 & 0 & 0 \\ 0 & 20 & 0 \\ 0 & 0 & 1 \end{pmatrix}$
Derivative Control Gain	$\Gamma = \begin{pmatrix} 4 & 0 & 0 \\ 0 & 4 & 0 \\ 0 & 0 & 8 \end{pmatrix}$
Filtered Derivative Time Constant	$\tau_f = 0.02$

Table 7.7: Algorithm 3 With Linear Acceleration Simulation Parameters

Algorithm 1 Simulation Results

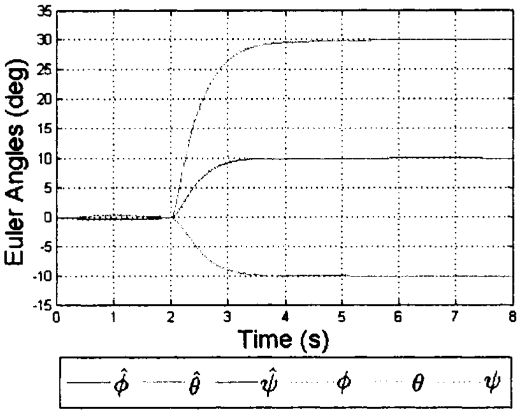

Figure 7.1: Estimated System Attitude

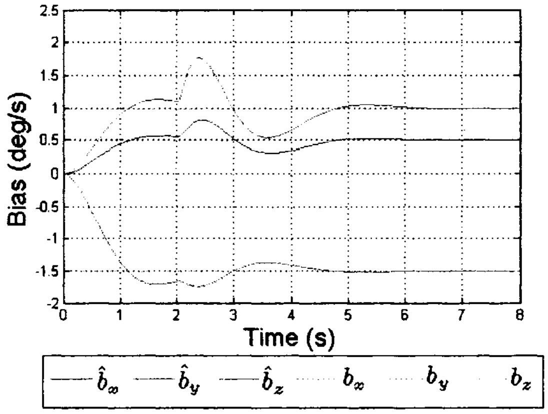

Figure 7.2: Estimated Bias

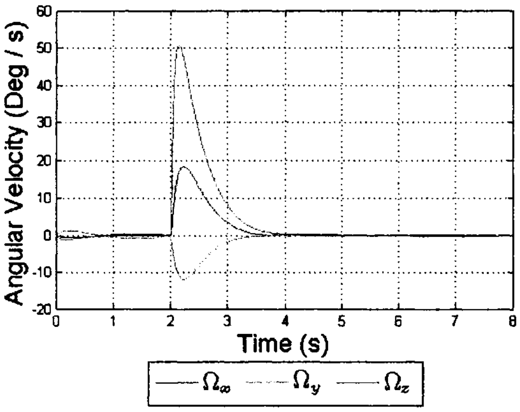

Figure 7.3: System Angular Velocity

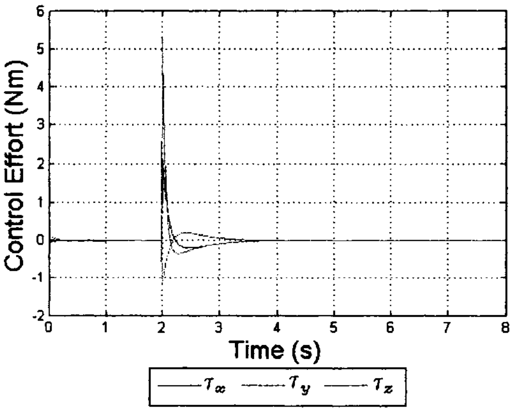

Figure 7.4: System Control Effort

Algorithm 2 Simulation Results

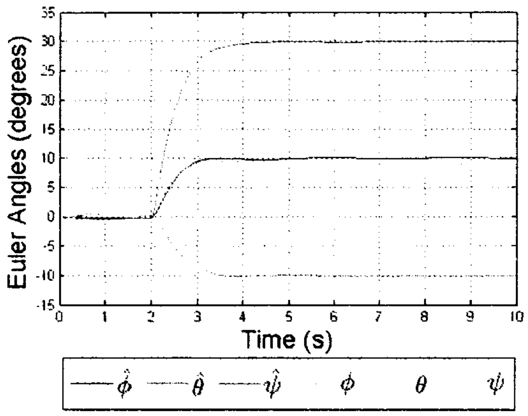

Figure 7.5: System Attitude

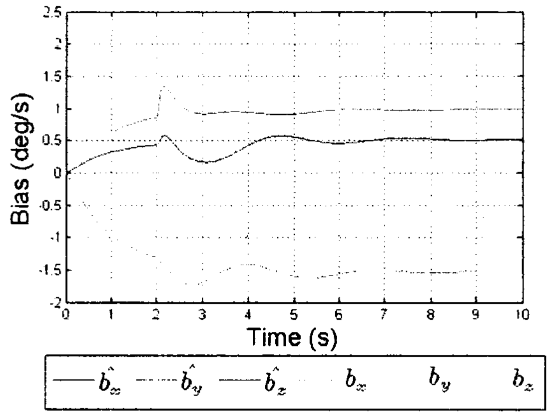

Figure 7.6: System Bias

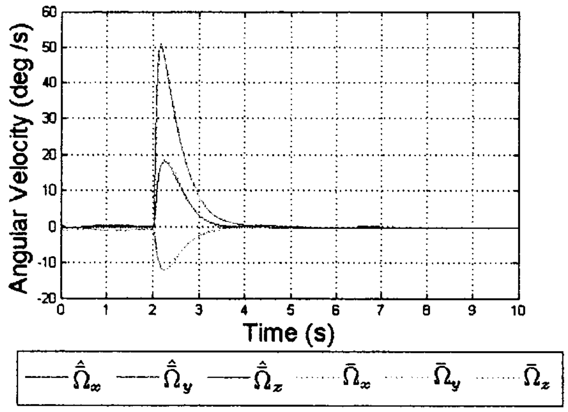

Figure 7.7: System Angular Velocity

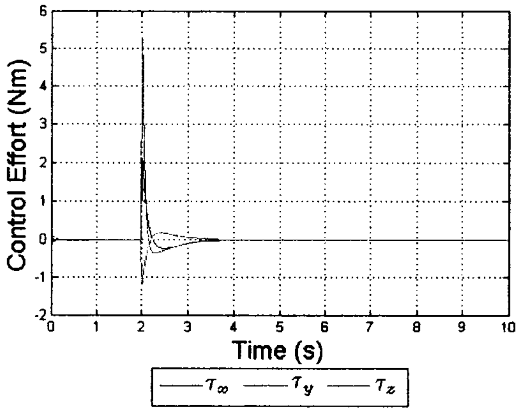

Figure 7.8: System Control Effort

Algorithm 3 Simulation Results

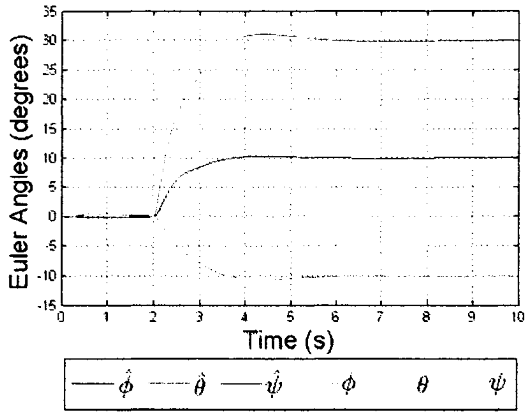

Figure 7.9: Estimated System Attitude

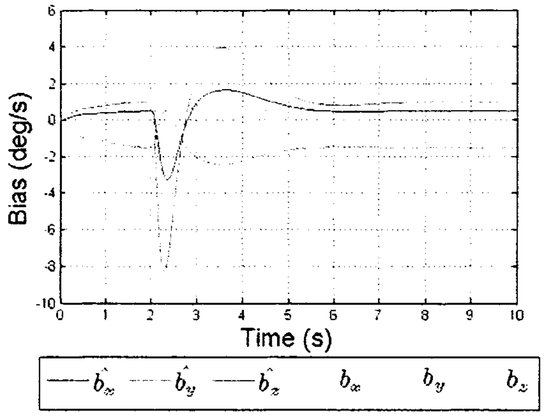

Figure 7.10: Estimated Bias

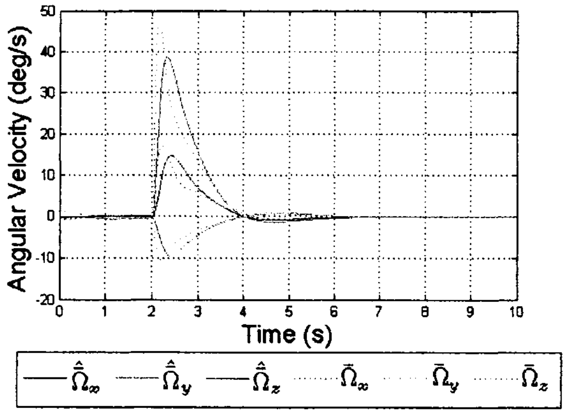

Figure 7.11: Angular Velocity Observer

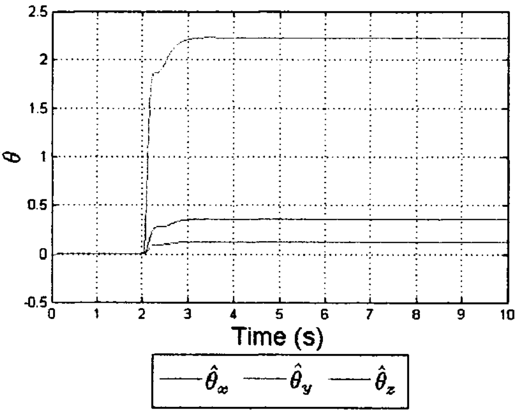

Figure 7.12: Low Pass Char. Observer

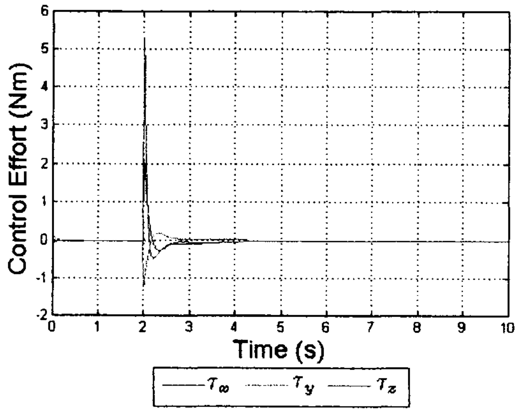

Figure 7.13: Control Effort

Algorithm 1 with Linear Acceleration Simulation Results

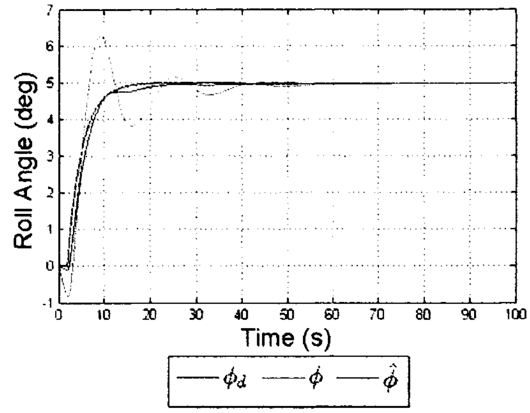

Figure 7.14: System Roll

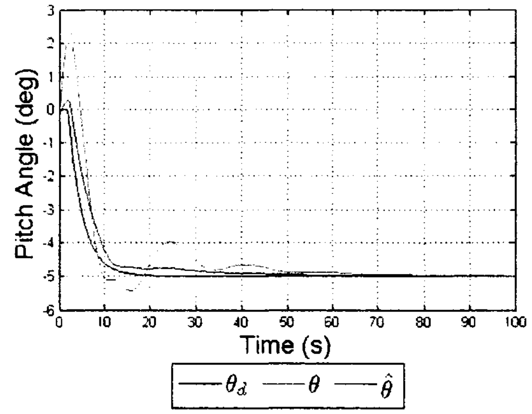

Figure 7.15: System Pitch

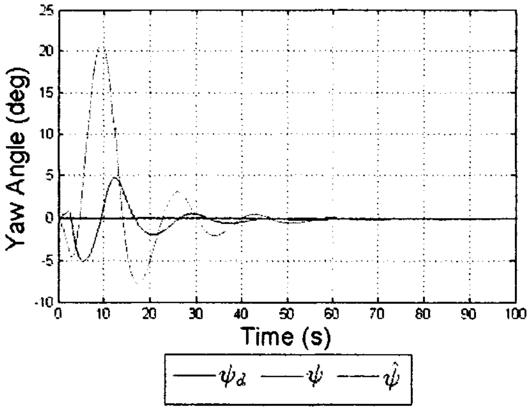

Figure 7.16: System Yaw

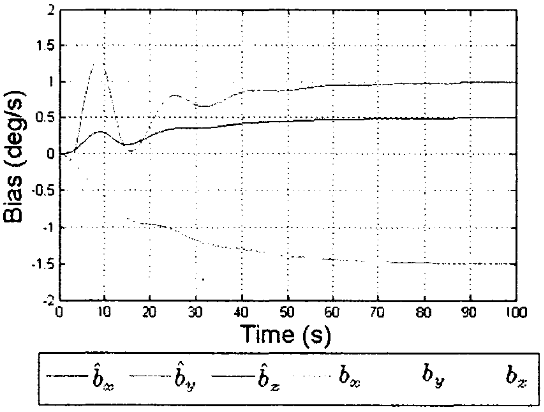

Figure 7.17: System Bias

Algorithm 2 with Linear Acceleration Simulation Results

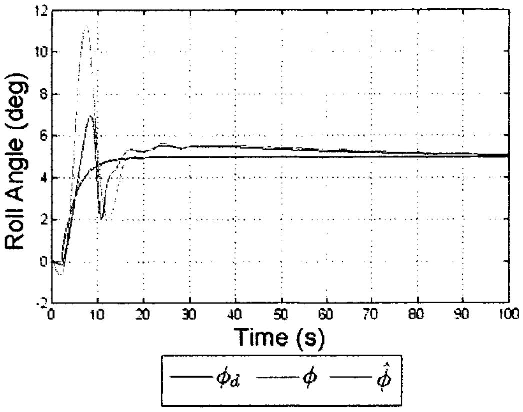

Figure 7.18: System Roll

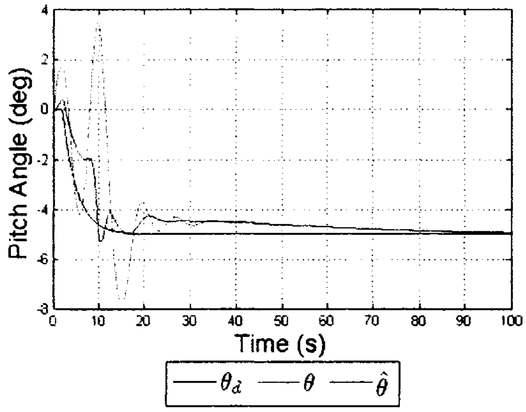

Figure 7.19: System Pitch

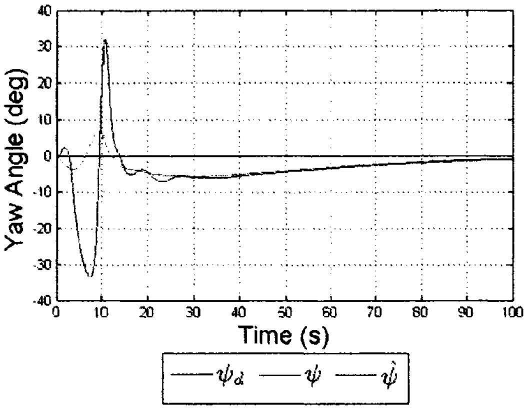

Figure 7.20: System Yaw

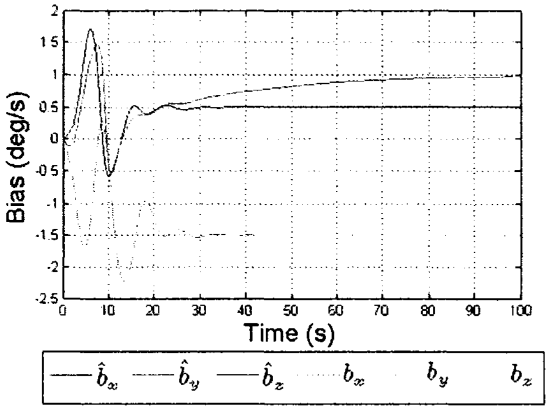

Figure 7.21: System Bias

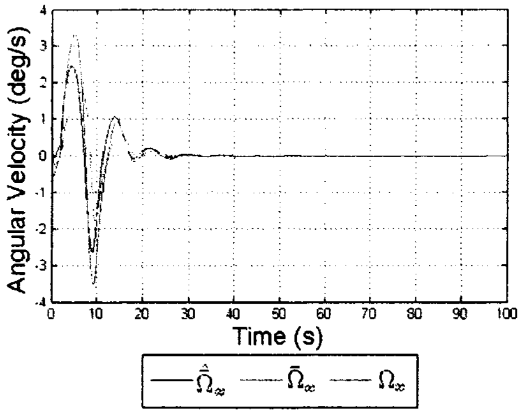

Figure 7.22: Angular Velocity x

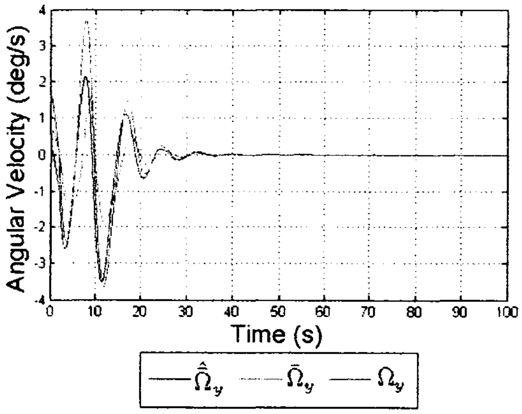

Figure 7.23: Angular Velocity y

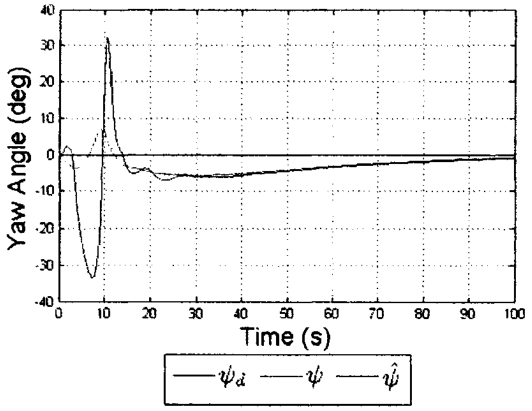

Figure 7.24: Angular Velocity z

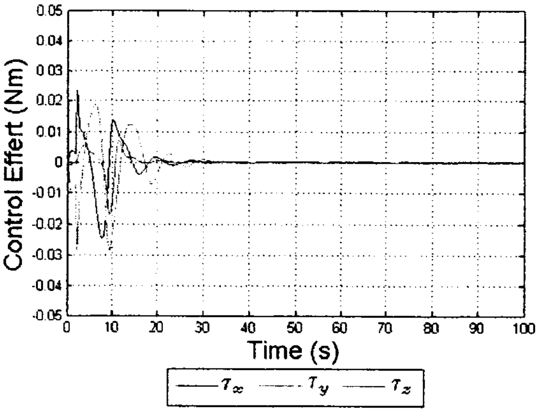

Figure 7.25: System Control Effort

Algorithm 3 with Linear Acceleration Simulation Results

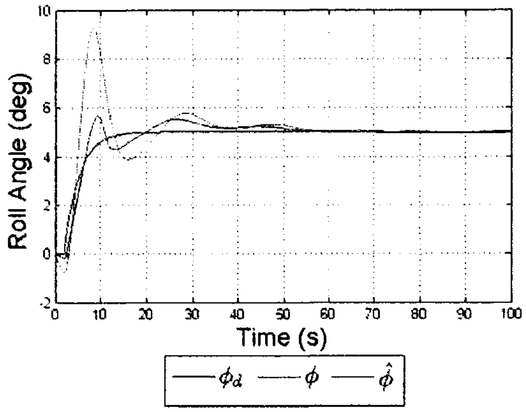

Figure 7.26: System Roll

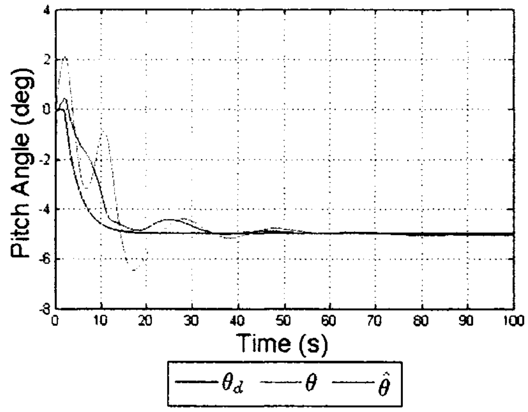

Figure 7.27: System Pitch

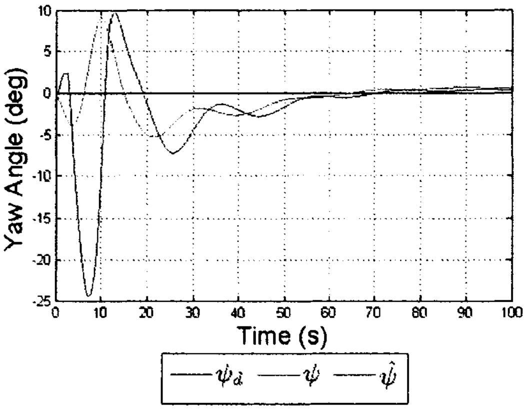

Figure 7.28: System Yaw

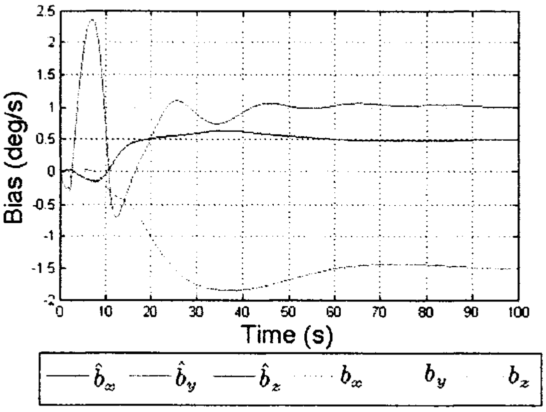

Figure 7.29: System Bias

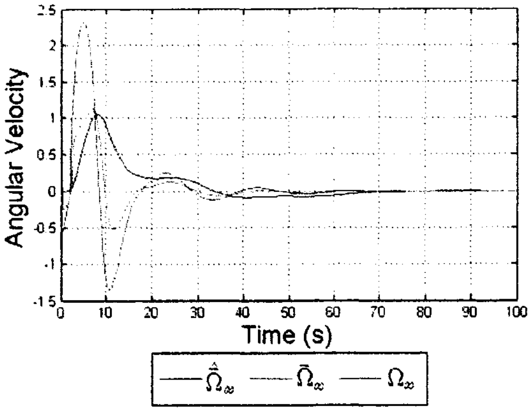

Figure 7.30: Angular Velocity x

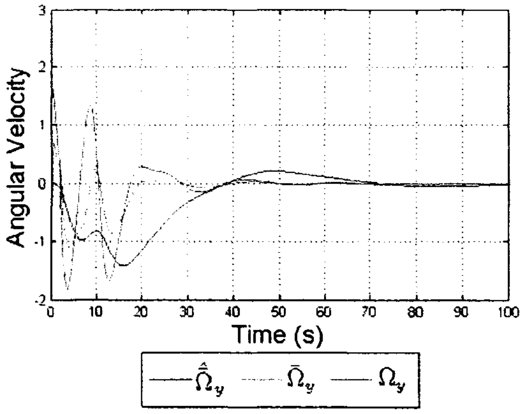

Figure 7.31: Angular Velocity y

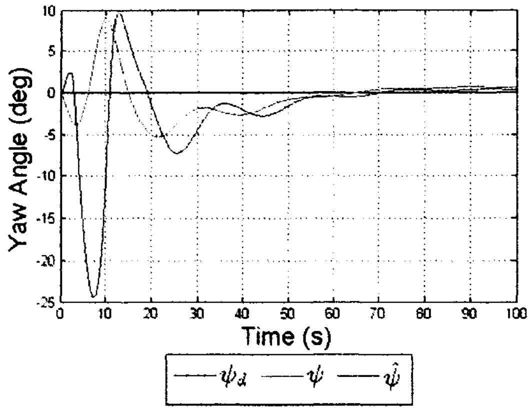

Figure 7.32: Angular Velocity z

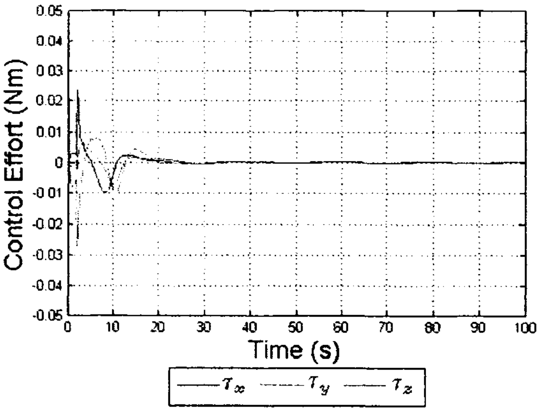

Figure 7.33: System Control Effort

Chapter 8

Experimental Results

A prototype aircraft was developed in order to test the theory discussed in this thesis. The design criterion was to implement a fully autonomous system with the required power sources and embedded circuitry necessary for stand-alone operation. Other systems, for example [26] and [18], have been implemented where the control signals were sent to the aircraft via a fixed or wireless link, however, for this system a fully embedded solution was investigated.

8.1 System Prototype

Since this system contains two rotors, two separate motors, batteries and motor controllers were used. Also, since these components had to be placed near each other, structures at the top and bottom of the aircraft were required to hold the devices. These structures are called the nose and tail cone, respectively. The primary structure, or super-structure, of this system is the duct itself, which includes motor mounts and connections to the upper and lower system structures. The duct was also used to route wiring to and from the nose and tail cone. To provide the control effort, control surfaces were built and located at the exit of the duct. This section gives a description of these system components.

8.1.1 Shroud or Annular Airfoil

The system structure is separated into the shroud or duct itself, the nose cone, and the tail cone. The system power plant was primarily considered for a maximum system weight of $12lbs$. The conclusion of these considerations opted for a rotor diameter of 14 inches. The shroud, which is shown by figure (8.1), was fabricated using rigid foam. The foam was professionally milled to create the contours of the duct as well as the tolerances required for the rotor on the inner section, which can be seen in Figure (8.2). The inside section of the duct was also designed to increase in diameter towards the exit of the duct in order to enhance thrust augmentation. After machining the sections of the shroud, holes for the motor mount shafts were drilled with high precision at exactly 120^o apart. The motor mount shafts were manufactured from $3/8''$ carbon fiber tubing, which were permanently implanted within the duct using water-based contact cement. The motor-mount shafts are connected to the motor mounts using 2 screws. However, since drilling holes in carbon fiber dramatically degrades the structural integrity of the carbon fiber tube, the ends of the carbon fiber tube were filled with wooden doweling and adhesive. The motor mounts, being the only part made of metal, were fabricated from aluminum using a computer numerically controlled (CNC) mill, to ensure the motor and rotor were perfectly centered.

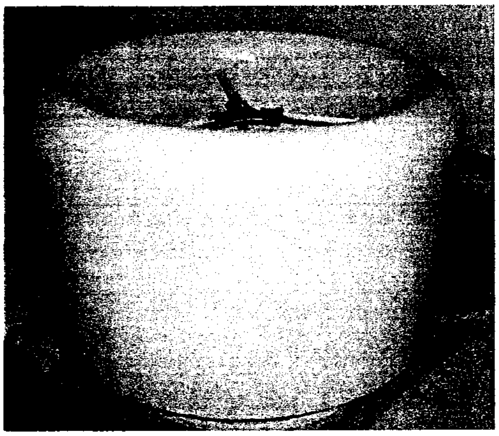

Figure 8.1: System Shroud

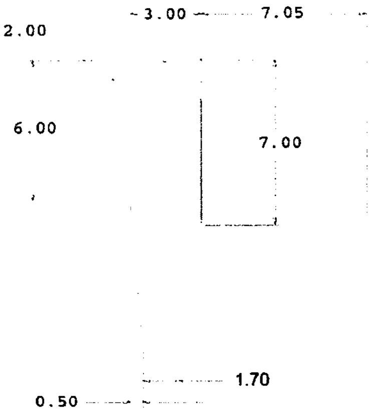

Figure 8.2: Shroud Dimensions

Ideally, composite materials would be used to manufacture the duct. Since these materials were not readily available, rigid foam was chosen for it's lightweight characteristics. This material is also able to absorb an impact from a blunt object, since the foam will deform easily. However, rigid foam tends to puncture and crack very easily, especially when a collision with a sharper object occurs. In order to improve the structural rigidity, a fine fiberglass cloth was applied with a 2-part epoxy adhesive. Since the adhesive came in contact with the foam, it was important that an epoxy-type adhesive was used rather than the traditional fiberglass resin. Traditional fiberglass resin is a solvent based product, and would quickly react with the foam resulting in a rapid deterioration and deformation of the foam. For this reason, care was chosen with all materials that came in contact with the foam, for example paint. After application of the fiberglass cloth, the duct was sanded, and finally covered in a coat of water-based paint. Two symmetrically placed holes were drilled on each side of the duct to allow for wiring. These holes were drilled on an angle near the top of the duct to allow for the connection of a tube to the nose cone for system wiring. Finally, slots were cut into the bottom of the shroud to allow mounting of the control surfaces and the landing ring.

8.1.2 Control Surfaces, Landing Ring, and Tail Cone

In order to produce the torque required to stabilize the aircraft, a system of ailerons, or wings, is required which are called the control surfaces. These ailerons are positioned at the exit of the duct. Each aileron, which is shown by Figure (2.1), was fabricated from balsa in addition to plywood when extra strength was required. Four independently actuated pairs of ailerons were mounted to a base support located at the exit of the shroud. The base support is also shaped like an airfoil to create a *flapped airfoil* as discussed previously in section (2.3.1. A plastic laminating film was used to cover the control surfaces. This laminating film contains an adhesive on one side and is applied using heat. Each aileron has an effective area of $11 sq.in$ which is smaller than the actual physical area since a portion of the aileron is shielded by the wall of the shroud.

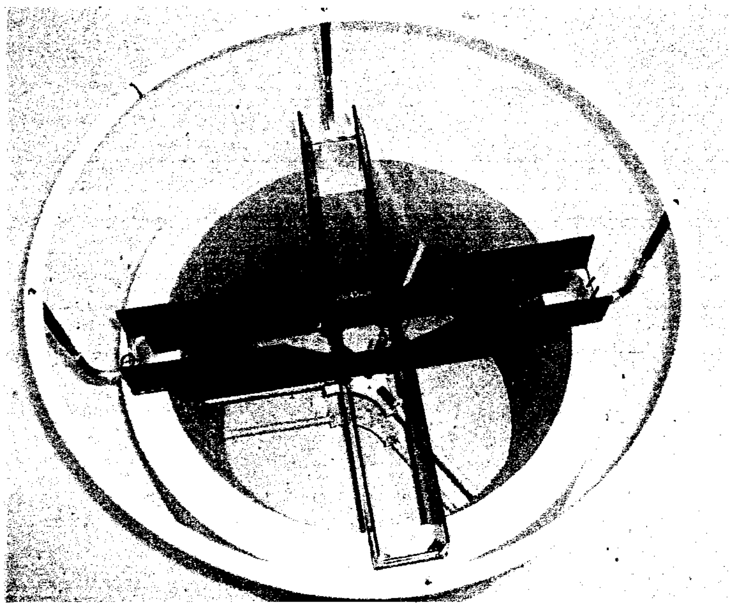

Figure 8.3: Control Surfaces and Landing Ring

Each pair of ailerons are actuated by a HiTec® HS-81 micro servo, which has a rated stall torque of $42oz - in$ and a maximum speed of 110 rpm. The servo is connected to the ailerons via a plastic ball-joint as well as metal and plastic linkages as shown by (8.4). The control surfaces also act as a mounting point for four spring loaded legs which are attached to a circular plastic landing ring. The spring loaded legs are made from carbon fiber tubing which mate with an aluminum rod which was machined using a lathe. The legs are mounted to the control surfaces via a hole drilled into the shroud. This hole was fitted with a plastic grommet to protect the shroud and to distribute the forces applied by the legs over a larger area. A tail cone section made from balsa wood was added to house the lower battery, servo power supply, and the lower motor controller. The tail cone was also built using balsa wood.

8.1.3 Nose Cone

A structure was required to house the required power sources and electronics required to operate the system prototype. This structure was designed to sit above the duct on the center axis of the aircraft to maintain symmetry and balance. A series of initial prototypes finally led to the design of a nose cone as illustrated in Figures (8.6) and (8.7). The nose cone structure was fabricated from ABS plastic using a rapid prototyping 3-dimensional printer. This device is programmed to build 3-dimensional structures by depositing drops of ABS plastic layer by layer. This is not a perfect final solution for the nose cone structure since a stronger structure would be better suited for an aircraft. However, this was a good solution for the prototype since all components are mounted neatly and accurately. This is especially important since misplaced heavy components, such as the battery, will affect system balance and performance.

The nose cone contains most of the system electronics. Since the battery and electronic speed controller

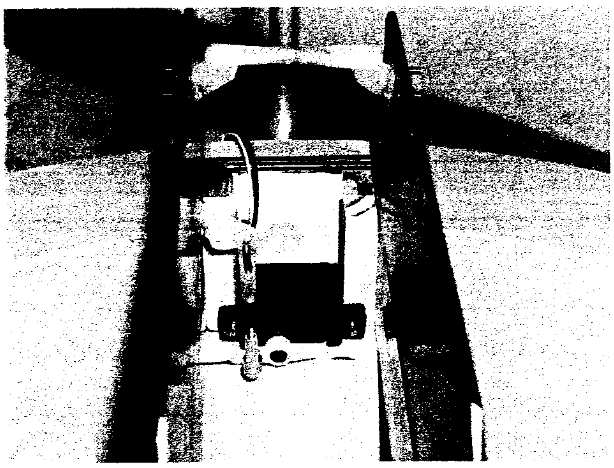

Figure 8.4: Servo Linkages

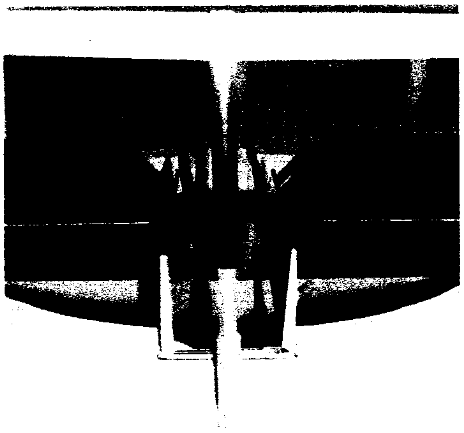

Figure 8.5: Spring Loaded Legs

(ESC) for the upper motor should be placed close to the motor, they were also placed within the nose cone. As shown in Figure (8.7), the nose cone houses the system digital signal processor, interface electronics, RF receiver, and all sensors required for the attitude stabilization which are contained in the inertial measurement unit.

8.1.4 System Power Plant

Careful consideration was taken when choosing the components for the system power plant. The power plant consists of the main batteries, motors, motor controllers, and the rotors. The choice of components all originated from the maximum system weight constraint of 12 lbs. Since the remote controlled aircraft hobby industry is very active, the technology behind related motors, batteries, and other electronics in this field has drastically progressed. As a result, a wide selection of high performance components are readily available. Currently, the two types of motors often used are either powered electrically, or by liquid fuel. Since this system prototype will most often be used in a laboratory environment with limited ventilation, the electric option was chosen. However, aircraft powered by a liquid fuel would offer longer flight times. In liquid fueled ducted fan aircraft, the duct also usually serves as the fuel tank.

From the weight constraint the motor chosen was the Plettenberg Orbit 25-12 outrunner motor, as shown in Figure (8.8). The term 'outrunner' refers to the fact that the motor exterior armature rotates around a fixed inner stator. This motor, which is manufactured in Germany, is highly efficient and has a maximum speed of 25,000 rpm. An optional cooling fan was also ordered with the motor. Since this motor is a three-phase brushless motor, a three-phase motor controller is required. The MGM Compro 8024-3 HELI in a programmable three-phase electronic speed controller (ESC) which has a current rating of 80A continuous and 100A peak.

As shown in Figure (8.10), the motors and rotors are mounted in opposite directions. Since the rotors must rotate in opposite directions, two different types of rotors were used. The upper rotor is a *pusher* type

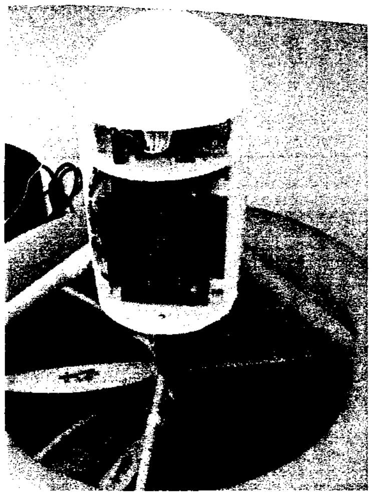

Figure 8.6: Nose Cone

of propeller, since it pushes against the motor. The lower rotor is a *tractor* propeller, which is the type used most often with aircraft. Other than the opposite pitch, the two propellers are identical. Initially, two Zinger® wooden 14 × 6 propellers were used. Future work will involve the investigation of different rotors, for example rotors made from nylon and composite materials, as well as rotors with multiple blades.

A high performance battery is required due to the powerful motors. Lithium polymer batteries were used due to their high current capability and since they are much lighter than other traditional non-lithium batteries. The batteries used were the Thunder Power ® 6-cell 4.2Ah lithium-polymer batteries, which are capable of supplying a continuous current of 63A, and a peak current of 100A. One disadvantage associated with the use of lithium batteries is that caution is required when charging or discharging the batteries. For a 6-cell battery the no-load voltage should never exceed the range of 19.8V to 25.2V (3.3V min / 4.2V max per cell). Over-discharging lithium batteries can result in deterioration of battery life and reduced capacity. Over-charging the lithium batteries can result in internal failure resulting in violent combustion. As a result, only chargers which are meant to be used with Lithium batteries should be used. Also, since the batteries contain multiple cells in series and parallel, the individual cell voltages must be kept equal. To accomplish this, good lithium batteries have extra connections known as balancing tabs which connect to the battery charger or to a separate balancer. For the batteries used in this system, the manufacturer recommended the Thunder Power TP1010C charger and TP210V balancer.

8.1.5 Low Voltage Power Supply

A number of different electronics are contained in the system which require different source voltages. The control surface servos, RF receiver, DSP, and interface electronics require a 5V input. However, the servos introduce excessive noise and transients on the 5V rail which affect the other electronics. Since the main batteries have a voltage of at least 20V, the use of linear regulators would require excessive heat sinking due to the large voltage drop and power dissipation within the regulator. Switching regulators could be used to

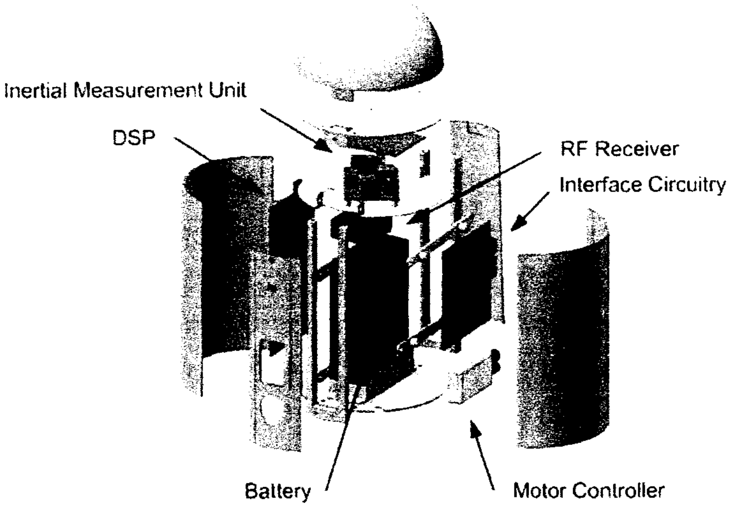

Figure 8.7: Nose Cone - Exploded View

eliminate the power dissipation problem. However, the noise associated with these types of power supplies affects the system electronics like the DSP and the analog sensors. To overcome this problem, a switching regulator and a linear regulator with a third low-voltage battery was used. The switching regulator was used with the lower main battery to supply 5V to the control surface servos. A separate Lithium 3-cell 800mAh battery was used with a linear regulator to power the DSP, RF receiver, IMU, the interface electronics, and the ESC's since they require a 5V rail in addition to the main battery.

8.1.6 Digital Signal Processor

A flexible and powerful solution for real-time implementation. To accommodate the constant system changes experienced with a prototype, a DSP which is easily programmed was preferred. The DSP is required to receive signals from a pilot operated transmitter, monitor the analog sensors, and provide control signals to the system motors and servos, all while processing the control and estimation algorithms.

After some investigation, a Texas Instruments C2000 family DSP was chosen. To aid in the prototype process, the R2812 eZdsp development board was used. This board is manufactured by Spectrum Digital using the TI TMS320C2000 R2812 chip. The development kit was also chosen due to it's compatibility with Mathworks Embedded Target software. This software offers automatic code generation, which uses Real Time workshop and fixed-point Simulink to program the DSP. The code is generated based on the Simulink model where additional DSP Simulink blocks are provided to automatically program all of the DSP peripherals such as analog-digital converter, capture inputs, PWM outputs, general purpose IO, and communication platforms such as CAN networks and serial ports. The DSP operates at 150MHz, with a peripheral clock of 75MHz, allowing the DSP to perform all of the required tasks while maintaining a fast control loop sampling time. For this system a sampling time of 1ms was used.

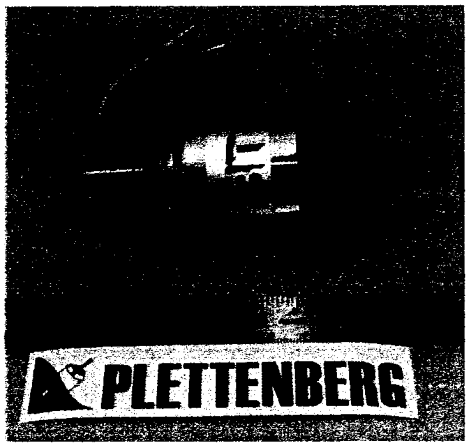

Figure 8.8: Plettenberg Orbit 25-12 Motor

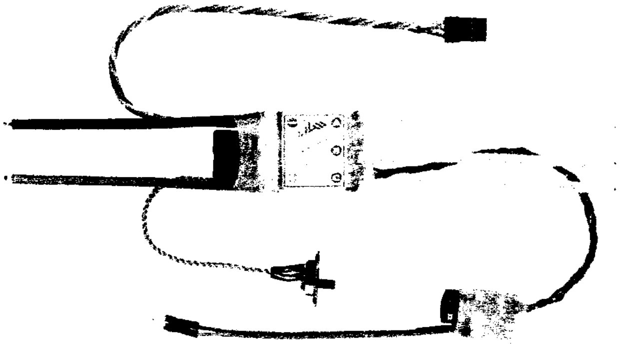

Figure 8.9: MGM Compro 8024-3 HELI ESC

The eZdsp development boards are offered with either the 'F' or 'R' version of the C2812 chip. The main differences of the two processors are related to the type of internal RAM used, where the 'R' version has faster internal RAM at the expense of having no internal flash memory. Although the 'F' version of the chip is easier to implement stand alone applications due to the fact that it uses flash memory, the 'R' version can still be programmed for stand alone operation by using the on-board 256k EEPROM. The 'R' version of the chip was chosen due to the larger EEPROM memory and since it connects to the host computer via USB.

While using the USB interface, a real-time connection can be made from MATLAB to the DSP through the TI Code Composer Studio (CCS) platform. This is useful for troubleshooting and obtaining data for any signal within the programmed DSP. While operating in stand-alone mode when the USB communication is disabled, the DSP can communicate to the host using one of the other communication platforms such as the CAN bus or through one of the two available serial ports.

8.1.7 Inertial Measurement Unit

The inertial measurement unit is the sensor assembly which includes the accelerometers, magnetometers and gyroscopes. The IMU is mounted in the nose cone near the top of the system. The ideal location for the IMU is at the system center of gravity, to minimize the centrifugal and transverse accelerations due to rotational motion. However, placing the IMU near the top of the system reduces the effect of perturbing magnetic fields due to the ESC and upper motor. In fact, due to the sensitivity of the magnetic sensor, a bias measurement and calibration must be performed to measure the effect of static magnetic fields due to electronics such as the linear regulator.

The accelerometer and gyroscope are both IMEMS (Integrated Micro-Electromechanical Systems) sensors from Analog Devices Inc. (ADI). An ADXL330 $\pm 2g$ triaxial accelerometer and three ADXRS300 $\pm 300^\circ/s$ single-axis gyroscopes were used. Since the gyroscope is a single axis sensor, three are used in the IMU which are mounted on orthogonal axes using right-angled sockets. These sensors are unique since moving mechanical systems are all contained within an integrated circuit on the substrate level. The IMEMS gyroscope measures the rate of rotation by the coriolis force, which is experienced by linear translation of a

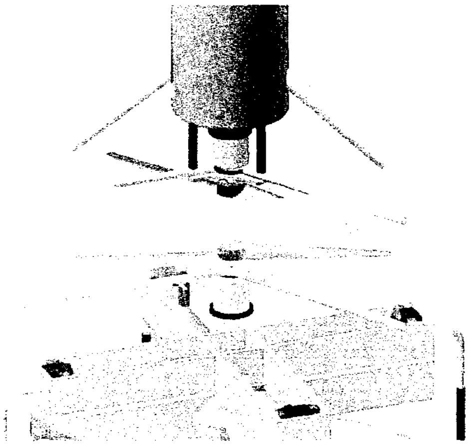

Figure 8.10: Motor Orientation

mass within a rotating frame of reference. To illustrate this effect consider Figure (8.12). For the IMEMS gyroscope, a resonating mass is used on the substrate, which oscillates back and forth on one axis. When the entire arrangement experiences a rotation, the linear motion of the resonating mass causes a coriolis force. Capacitive sensors are used to sense the movement of the resonating mass due to the coriolis force. Since the mass is resonating at a high frequency, then the resulting movement due to the coriolis effect will also be an alternating signal, where the amplitude of the signal corresponds to the rate of rotation. Since linear accelerations of the sensor would not produce an alternating signal, these sensors can distinguish between rotational and linear motion. The accelerometers operate on the same principal as the gyroscopes except without the resonating mass, using the capacitive sensors to detect motion due to any sensor accelerations.

The Honeywell HMC2003 triaxial magnetometer was used for the magnetic reference. For each axis, this sensor uses a magneto-resistive bridge to sense magnetic fields up to 2 Gauss, with a rated bandwidth of 2kHz. Since the sensitivity and bias of the magnetic sensor can vary, especially when the sensor is exposed to strong magnetic fields, the sensor contains reset circuitry. This circuitry pulses the sensor with a domain-realigning magnetic field from an externally supplied current source to ensure sensor bias and sensitivity remain constant.

8.1.8 Interface Circuitry

The interface circuitry has a number of different tasks involving signal conditioning of the sensors, and communication with the servos and motors. Although the DSP development board requires 5V, the R2812 DSP is a 3.3V device which is powered using an onboard regulator. Since the gyroscope and magnetometer require larger supply voltages, some signal conditioning is performed to change the bias of these signals. Also, a gain is implemented on magnetometer signals to boost the weak surrounding magnetic field measurement. For future work a significant improvement would be to use sensors with digital outputs or use ADC's located close to the analog sensors, since noise and transients can be coupled to the signals when long wires are used, especially in the presence of gain.

In addition to the analog signal conditioning, the interface circuitry is used to communicate with the servos

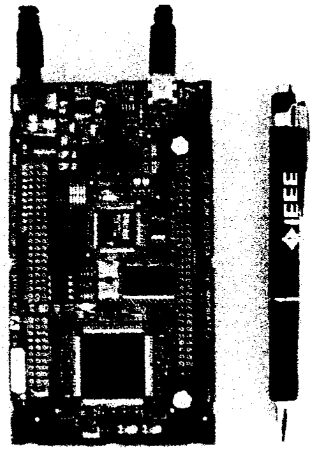

Figure 8.11: Spectrum Digital R2812 eZdsp Development Board

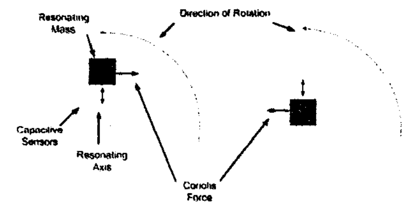

Figure 8.12: IMEMS Gyro Theory of Operation

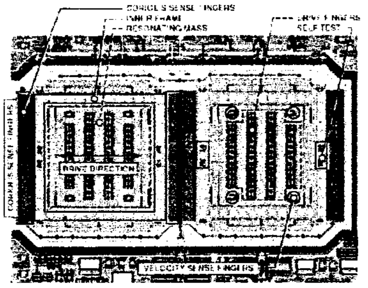

Figure 8.13: IMEMS Gyroscope - Substrate (curtesy of ADI)

and electronic speed controllers since the DSP is too fast for these electronics. The remote controlled aircraft industry commonly use pulse-width modulated signals which operate around 50Hz. Since the DSP PWM outputs are designed to control motors directly through an H-bridge, the minimum obtainable PWM frequency is just over 1kHz. Therefore, the interface circuitry has the ability to read 6 PWM signals operating at 1250Hz, which it then converts to signals operating at 50Hz for the ESCs and servos.

The extra electronics also provides an extra level of redundancy over the DSP alone. Emergency stop inputs, fault detection, and IMU resetting signals are all performed by the interface electronics. These functions are performed by two Microchip dsPIC30F4011 digital signal processors operating at a frequency of 30MHz. These extra DSP's also receive the pilot inputs and can operate the system in open-loop. This is useful for system testing and prototyping to ensure the system is functioning properly before allowing the main DSP to take control of the system.

8.2 Experimental Data

An experimental test using the developed prototype was performed. Due to the presence of noise, several filters were used as shown in Figure (8.14). In addition to the filters, saturation was applied to the control effort to limit the movement of the control surfaces. It is apparent from the experimental results that a significant amount of noise is present in the system. This can be attributed partly to the analog sensors. Despite the noise, the results show a correlation between the desired and estimated attitude for the system. The desired attitude shown was obtained from a pilot input which attempted to minimize the linear motion of the system. Due to physical limitations of the aircraft surroundings, larger deviations in attitude was not possible.

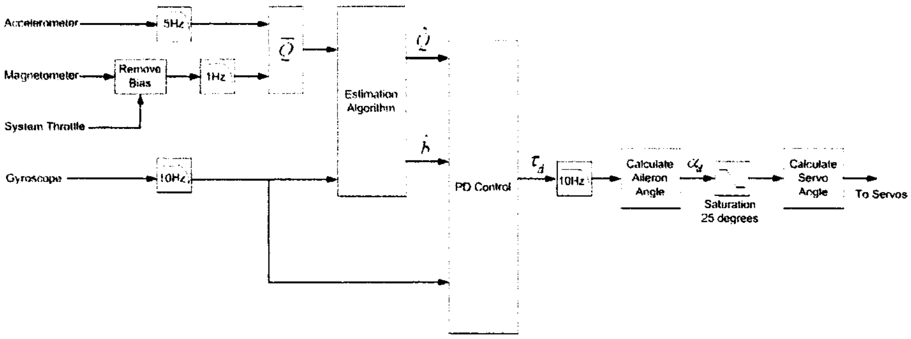

Figure 8.14: Estimation and Filtering Block Diagram

Parameter	Value
Proportional Control Gain	$\alpha = \begin{pmatrix} 25 & 0 & 0 \\ 0 & 25 & 0 \\ 0 & 0 & 6.25 \end{pmatrix}$
Derivative Control Gain	$\Gamma = \begin{pmatrix} 2.5 & 0 & 0 \\ 0 & 2.5 & 0 \\ 0 & 0 & 0.5 \end{pmatrix}$
Initial Conditions	$\hat{Q}(0) = Q_I$ $\hat{b}(0) = 0_{3\times 1}$
Observer Gains	$\Gamma_1 = 3I_{3\times 3}$ $\Gamma_2 = 0.5I_{3\times 3}$

Table 8.1: Experimental Results – Control and Estimation Parameters

Experimental Results

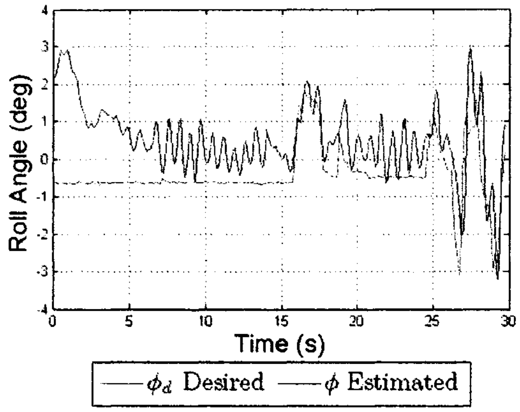

Figure 8.15: System Roll

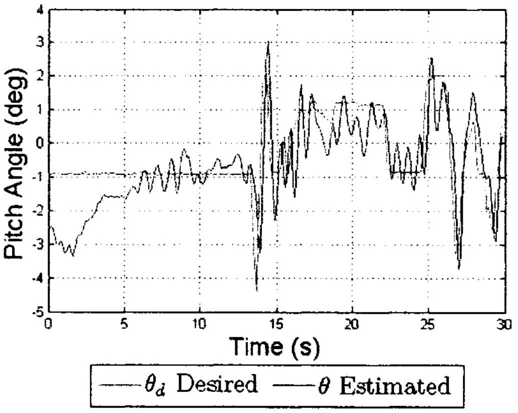

Figure 8.16: System Pitch

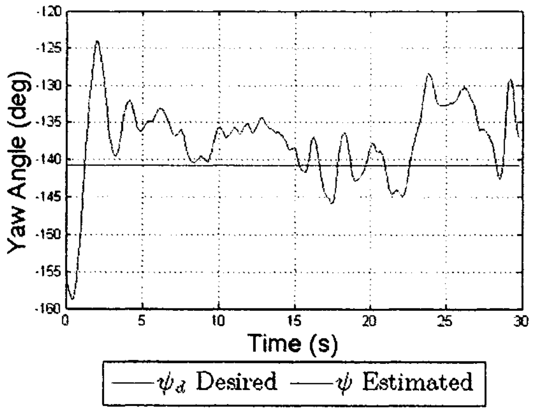

Figure 8.17: System Yaw

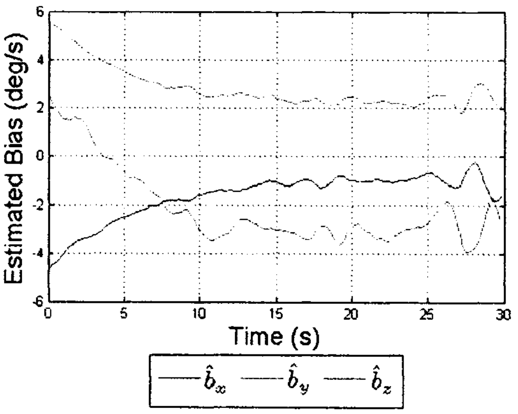

Figure 8.18: Aileron 1 Desired Angle

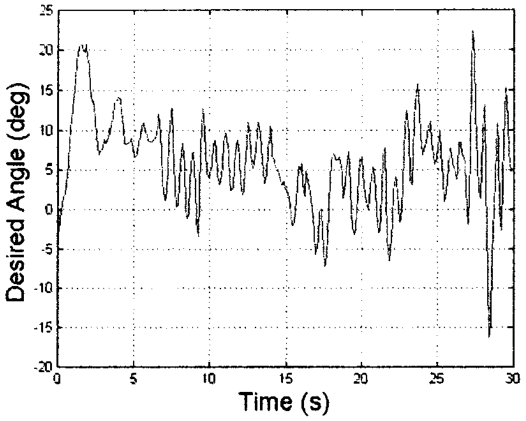

Figure 8.19: Aileron 1 Desired Angle

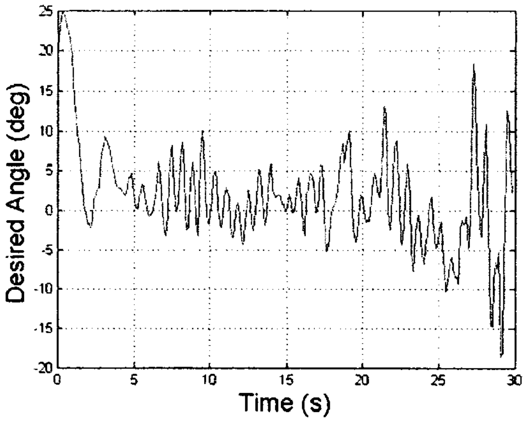

Figure 8.20: Aileron 2 Desired Angle

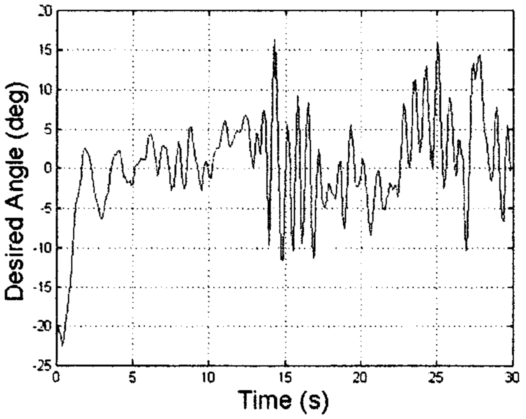

Figure 8.21: Aileron 3 Desired Angle

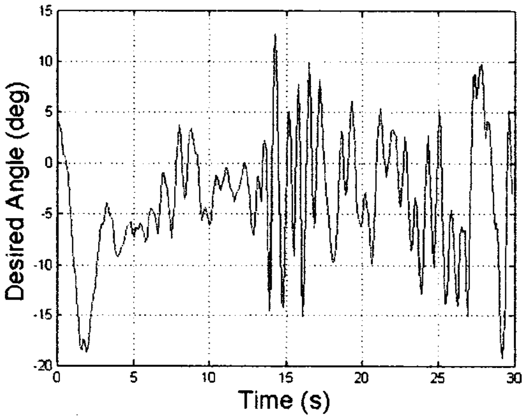

Figure 8.22: Aileron 4 Desired Angle

Chapter 9

Conclusion

Remotely operated unmanned aircraft has been the focus of many researchers due to the increasing number of applications which they are suited for. Both manned and unmanned aircraft can be either fixed-wing, vertical take-off and landing (VTOL), or a combination of the two. Hovering aircraft are better suited for a number of applications since they can remain in a stationary position. Some of these applications could include surveillance, surveying, search and rescue, infrastructure inspection (for example bridges), aerial photography, atmospheric measurements, or any application where human presence may be unsafe. Unmanned aircraft can be directly operated by a pilot using a wireless link. However, it is desirable to develop aircraft which are autonomous requiring less input from a pilot. As a result, virtually anyone could fly these aircraft with little to no training since the aircraft is able to operate itself.

The ducted fan VTOL aircraft is considered since it offers a level of safety over traditional helicopters. Furthermore, it can be more compact since a helicopter tail and tail rotor are not required due to two counter-rotating propellers, or by the use of control surfaces to counter the rotor torque. The ducted fan can also offer additional thrust when compared to the unshrouded rotors, since the duct reduces rotor loss and improves efficiency.

An aerodynamic analysis was performed to study the airflow within and outside the duct to quantitatively describe (where possible) the forces and torques acting on the system. The aerodynamic analysis includes the airflow moving through the duct, the force generated by the system control surfaces, as well as the thrust generated by the rotor blades. In order to describe the system attitude, a thorough description of attitude representation is given which includes direct cosine matrices, Euler angles, and the unit quaternion. Using the description of system forces obtained from the aerodynamic analysis, and the attitude representation, a complete derivation of a system dynamic model is given which includes gyroscopic torques of the system and rotor blades, as well as the effect of unequal rotor velocities and external disturbances.

The primary challenge of developing an autonomous attitude stabilizing controller, is to obtain reasonably accurate estimates of the system attitude. To accomplish this task a number of inertial sensors are used. Gyroscopes are used since this signal is directly linked to the rate of change of the system attitude. Alone the gyroscope signals are not reliable since unknown initial conditions and sensor bias cause estimation error and drift of the attitude estimates over time. Another way to obtain attitude estimates is by vector observation. Accelerometers and magnetometers are used to obtain body-fixed vectors of the earth's gravity and magnetic fields, in order to obtain estimates of the system attitude. Since the accelerometers are affected by system accelerations, and the magnetometers by other magnetic fields, these estimates are also flawed.

To overcome these problems, a number of estimation algorithms are discussed which were presented in [27]. These estimation algorithms use all three sensors to obtain enhanced estimates of the system attitude.

Having obtained accurate estimates of the system attitude, a PD control was implemented with a set-point input. The proportional part of the control input is the vector portion of an *error* quaternion. The gyroscope signal is used as an input for the derivative portion of the PD control. In the case where the gyroscope bias is estimated, this value is subtracted from the gyroscope signal.

A number of simulations are given which demonstrate the effectiveness of the estimation algorithms in a closed-loop system using the PD control. Simulations are also given to show the difficulties involved when other system dynamics and disturbances are introduced. The most difficult problem to overcome is due to the effect of linear accelerations on the accelerometer signals. Since the duct aerodynamic drag limits the system accelerations, it is useful to attempt to model this force to generate realistic simulations. Without including the aerodynamic drag, the simulations suggest that the system is very difficult to stabilize and is very sensitive to disturbances and changes in control gains. This can be challenging since it is difficult to predict the aerodynamic drag of the system without the use of wind tunnel testing.

A system prototype which was developed is presented. This system contains all of the required electronics to create an autonomous system, which includes a Texas Instruments DSP, inertial sensors, and power sources. The system prototype is used to provide experimental results of the theory discussed in this thesis.

One future system modification involves sensor signal conditioning. Currently, analog sensors are used which are affected by noise. Since the magnetometer signals also require gain, the signal accuracy is further reduced. An improvement would include digital sensors, or the use of an ADC near the analog sensors which would communicate to the DSP via serial communication. Also, by using an additional sensor to measure the system altitude, the pilot would not be required to control the throttle which would offer an extra degree of autonomy.

Other work could involve using the global positioning system (GPS) to obtain the systems position. Therefore, the current attitude stabilizing aircraft could be extended to have position control. Since the bandwidth of GPS devices is usually small, another interesting area of research would involve the use of a camera to improve the estimation of the system position and orientation. This could be especially useful in environments where GPS is unavailable, for example indoors. Multiple proximity sensors could also be implemented to improve the position control or to facilitate obstacle avoidance. Each of these improvements would enable the system to operate more and more without the direction of an operator.

Appendix A

System Physical Characteristics

A.1 System Parameters

Description	Parameter	Value
System Mass	m	$4.313kg$
Rotor Radius	R	$0.1778m$
Rotor Disk Area	A	$0.09931m^2$
Duct Exit Area	A_e	$0.1233m^2$
Duct Exit Area Ratio	a_d	1.24
Aileron Lift Coefficient Slope	a	5.3 (2π ideal)
Aileron Span	b	$0.1413m$
Flapped Airfoil Chord	c	$0.09464m$
Flapped Airfoil Hingepoint	k	0.4697
Vertical Distance from COG to Aileron COP	l	$0.1778m$
Horizontal Distance from COG to Aileron COP	d	$0.1270m$

Appendix B

Summary of Attitude Representation

B.1 Attitude Kinematics

B.1.1 Rotation Matrix

$$ {}^{b}_{o}\dot{R} = -S(\Omega)\,{}^{b}_{o}R \tag{B.1}$$

$$ {}^{b}_{o}\dot{R} = -{}^{b}_{o}R\,S(\Omega_o) \tag{B.2}$$

$$ {}^{o}_{b}\dot{R} = {}^{o}_{b}R\,S(\Omega) \tag{B.3}$$

$$ {}^{o}_{b}\dot{R} = S(\Omega_o)\,{}^{o}_{b}R \tag{B.4}$$

B.1.2 Quaternion

$$ {}^{b}_{o}\dot{Q} = \frac{1}{2}\,{}^{b}_{o}Q \odot Q_{\Omega} \tag{B.5}$$

$$ {}^{b}_{o}\dot{Q} = \frac{1}{2}Q_{\Omega_o} \odot {}^{b}_{o}Q \tag{B.6}$$

$$ {}^{o}_{b}\dot{Q} = -\frac{1}{2}Q_{\Omega} \odot {}^{o}_{b}Q \tag{B.7}$$

$$ {}^{o}_{b}\dot{Q} = -\frac{1}{2}\,{}^{o}_{b}Q \odot Q_{\Omega_o} \tag{B.8}$$

B.2 Transformations

B.2.1 Rotation Matrix and Euler Angles

$$ {}^{b}_{o}R_{321} = \begin{pmatrix} c_\theta c_\psi & c_\theta s_\psi & -s_\theta \\ s_\phi s_\theta c_\psi - c_\phi s_\psi & s_\phi s_\theta s_\psi + c_\phi c_\psi & s_\phi c_\theta \\ c_\phi s_\theta c_\psi + s_\phi s_\psi & c_\phi s_\theta s_\psi - s_\phi c_\psi & c_\phi c_\theta \end{pmatrix} \tag{B.9} $$

$$ \theta = \arcsin\left(-{}^{b}_{o}R_{13}\right) \tag{B.10} $$

$$ \phi = atan2({}^{b}_{o}R_{23}, {}^{b}_{o}R_{33}) \qquad \cos\theta \neq 0 \tag{B.11} $$

$$ \psi = atan2({}^{b}_{o}R_{12}, {}^{b}_{o}R_{11}) \qquad \cos\theta \neq 0 \tag{B.12} $$

B.2.2 Quaternion and Euler Angles

$$ {}^{b}_{o}Q_{321} = \begin{pmatrix} q_o \\ q \end{pmatrix} = \begin{pmatrix} c_{\phi/2}c_{\theta/2}c_{\psi/2} + s_{\phi/2}s_{\theta/2}s_{\psi/2} \\ s_{\phi/2}c_{\theta/2}c_{\psi/2} - c_{\phi/2}s_{\theta/2}s_{\psi/2} \\ c_{\phi/2}s_{\theta/2}c_{\psi/2} + s_{\phi/2}c_{\theta/2}s_{\psi/2} \\ c_{\phi/2}c_{\theta/2}s_{\psi/2} - s_{\phi/2}s_{\theta/2}c_{\psi/2} \end{pmatrix} \tag{B.13} $$

$$ \theta = \arcsin\left(2\left(q_o q_2 - q_3 q_1\right)\right) \tag{B.14} $$

$$ \phi = atan2\left(q_3 + q_1, q_o - q_2\right) - atan2\left(q_3 - q_1, q_o + q_2\right) \qquad \cos\theta \neq 0 \tag{B.15} $$

$$ \psi = atan2\left(q_3 + q_1, q_o - q_2\right) + atan2\left(q_3 - q_1, q_o + q_2\right) \qquad \cos\theta \neq 0 \tag{B.16} $$

B.2.3 Rotation Matrix and Quaternion

$$ {}^{b}_{o}R = I + 2S(q)^2 - 2q_o S(q) \qquad Q = {}^{b}_{o}Q \tag{B.17} $$

$$ S(q) = \frac{1}{2\sqrt{1 + \mathrm{trace}(R)}}\left(R^T - R\right) \tag{B.18} $$

For equation (B.18), a singularity exists if trace$(R) = -1$. One example where this singularity can occur is if the DCM represents a rotation about the z-axis by an angle of π. To avoid this type of phenomena a strategic method for obtaining the quaternion from the DCM is presented. The proposed method is free of singularities and also ensures the scalar part of the quaternion is always positive. If the scalar part of the quaternion is always positive, this establishes a bound on the angle of rotation, γ, to be always within $\pm\pi$.

The proposed algorithm is comprised of four different methods for obtaining the quaternion. Each method requires the division of a quaternion term. As a result each method contains singularities when the quaternion term divisor approaches zero. For all singularities, at least one of the four proposed methods will contain a singularity free result.

Let:

$$\alpha_1 = 1 + R_{11} + R_{22} + R_{33} \tag{B.19}$$

$$\alpha_2 = 1 + R_{11} - R_{22} - R_{33} \tag{B.20}$$

$$\alpha_3 = 1 - R_{11} + R_{22} - R_{33} \tag{B.21}$$

$$\alpha_4 = 1 - R_{11} - R_{22} + R_{33} \tag{B.22}$$

Singularities exist in the transformation from DCM to quaternion where $\alpha_i = 0$. For all singularities at least one of the expressions will contain a non-zero term. To avoid the singularity and to obtain greatest numerical accuracy the expression containing the largest value is selected.

Case 1: $\alpha_1 \geq \alpha_i, \quad i = 2, 3, 4$

$$q_0 = \frac{1}{2}\sqrt{\alpha_1} \tag{B.23}$$

$$q_1 = \frac{1}{4q_0}(R_{23} - R_{32}) \tag{B.24}$$

$$q_2 = \frac{1}{4q_0}(R_{31} - R_{13}) \tag{B.25}$$

$$q_3 = \frac{1}{4q_0}(R_{12} - R_{21}) \tag{B.26}$$

Case 2: $\alpha_2 > \alpha_i, \quad i = 1, 3, 4$

$$q_1 = \pm\frac{1}{2}\sqrt{\alpha_2} \tag{B.27}$$

$$q_0 = \frac{1}{4q_1}(R_{23} - R_{32}) \tag{B.28}$$

$$q_2 = \frac{1}{4q_1}(R_{12} + R_{21}) \tag{B.29}$$

$$q_3 = \frac{1}{4q_1}(R_{13} + R_{31}) \tag{B.30}$$

Case 3: $\alpha_3 > \alpha_i, \quad i = 1, 2, 4$

$$q_2 = \pm\frac{1}{2}\sqrt{\alpha_3} \tag{B.31}$$

$$q_0 = \frac{1}{4q_2}\left(R_{31} - R_{13}\right) \tag{B.32}$$

$$q_1 = \frac{1}{4q_2}\left(R_{21} + R_{12}\right) \tag{B.33}$$

$$q_3 = \frac{1}{4q_2}\left(R_{23} + R_{32}\right) \tag{B.34}$$

Case 4: $\alpha_4 > \alpha_i, \quad i = 1, 2, 3$

$$q_3 = \pm\frac{1}{2}\sqrt{\alpha_4} \tag{B.35}$$

$$q_0 = \frac{1}{4q_3}\left(R_{12} - R_{21}\right) \tag{B.36}$$

$$q_1 = \frac{1}{4q_3}\left(R_{31} + R_{13}\right) \tag{B.37}$$

$$q_2 = \frac{1}{4q_3}\left(R_{32} + R_{23}\right) \tag{B.38}$$

The choice of sign in (B.27),(B.31), and (B.35) is used to ensure that the scalar part of the quaternion, q_0, is always positive. This ensures that the angle of rotation is bounded to $\pm\pi$.

B.3 Other Forms of Attitude Representation

Two other forms of attitude representation are presented in [21]. The following is a summary of the representation including some transformations between the direct cosine matrix and the quaternion.

B.3.1 Rodrigues Parameters

The Rodrigues parameter, ρ, is essentially the same as the Euler-Rodrigues parameter, except the scalar term is included within the vector term. Since the Rodrigues parameters require only three terms, it is a minimal realization at the cost of introducing a singularity.

$$\rho = \begin{pmatrix} \rho_1 \\ \rho_2 \\ \rho_3 \end{pmatrix} = \frac{q}{q_o} = \tan\left(\theta/2\right)\hat{k} \tag{B.39}$$

The singularity exists since $\rho \to \infty$ as $q_o \to 0$ or $\theta \to \pm\pi$.

$$Q = \frac{1}{\sqrt{1 + \|\rho\|^2}}\begin{pmatrix} 1 \\ \rho \end{pmatrix} \tag{B.40}$$

$$R = \left(I - S(\rho)\right)\left(I + S(\rho)\right)^{-1} \tag{B.41}$$

B.3.2 Cayley-Klein Parameters

The Cayley-Klein matrix, H, is a complex realization of the Euler-Rodrigues Symmetric parameter in matrix form given by (B.42). This matrix is formed by the Cayley-Klein parameters α, β, γ, and δ, which use the imaginary number $\mathbf{i} = \sqrt{-1}$.

$$H = \begin{pmatrix} \alpha & \beta \\ \gamma & \delta \end{pmatrix} = \begin{pmatrix} q_o + q_3\mathbf{i} & q_2 + q_1\mathbf{i} \\ -q_2 + q_1\mathbf{i} & q_o - q_3\mathbf{i} \end{pmatrix} \tag{B.42}$$

Given the quaternion used to form the Cayley-Klein matrix belongs to the set of Euler-Rodrigues parameters, the matrix H is unitary, where the inverse is given by the complex conjugate transpose. Using the * operator as the conjugate,

$$H^{-1} = (H^\star)^T \tag{B.43}$$

For representing multiple rotations, the Cayley-Klein matrix properties for multiplication is similar to that of the direct cosine matrix. This is demonstrated in (B.44), where $H(Q)$ denotes the Cayley-Klein matrix based on the unit quaternion Q.

$$H(Q_1)H(Q_2) = H(Q_1 \otimes Q_2) \tag{B.44}$$

$$R = \begin{pmatrix} \frac{1}{2}\left(\alpha^2 - \beta^2 - \gamma^2 + \delta^2\right) & -\frac{\mathbf{i}}{2}\left(\alpha^2 + \beta^2 - \gamma^2 - \delta^2\right) & -\left(\alpha\beta - \gamma\delta\right) \\ \frac{\mathbf{i}}{2}\left(\alpha^2 - \beta^2 + \gamma^2 - \delta^2\right) & \frac{1}{2}\left(\alpha^2 + \beta^2 + \gamma^2 + \delta^2\right) & -\mathbf{i}\left(\alpha\beta + \gamma\delta\right) \\ -\left(\alpha\gamma - \beta\delta\right) & \mathbf{i}\left(\alpha\gamma + \beta\delta\right) & \left(\alpha\delta + \beta\gamma\right) \end{pmatrix} \tag{B.45}$$

Appendix C

Mathematical Background

Skew symmetric matrix:

$$skew(u) = S(u) = \begin{pmatrix} 0 & -u_3 & u_2 \\ u_3 & 0 & -u_1 \\ -u_2 & u_1 & 0 \end{pmatrix} \tag{C.1}$$

Dot product:

$$u \cdot v = u^T v = u_1 v_1 + u_2 v_2 + u_3 v_3 \tag{C.2}$$

Cross product:

$$u \times v \quad = \quad S(u)v \quad = \quad \begin{pmatrix} u_2 v_3 - u_3 v_2 \\ u_3 v_1 - u_1 v_3 \\ u_1 v_2 - u_2 v_1 \end{pmatrix} \tag{C.3}$$

Vector norm:

$$\|p\| = \left(p^T p\right)^{1/2} = \left(p_1^2 + p_2^2 \cdots p_n^2\right)^{1/2} \qquad p \in R^n \tag{C.4}$$

Matrix norm (Euclidean or Frobenius):

$$\|M\| = \left(\sum_{i=1}^{m} \sum_{j=1}^{n} M_{ij}\right)^{1/2} \qquad M \in R^{m \times n} \tag{C.5}$$

C.1 Properties of the Skew-Symmetric Matrix

$$S(u)S(v) \quad = \quad vu^T - u^T v I \tag{C.6}$$

$$S(\hat{k})^2 = \hat{k}\hat{k}^T + \|\hat{k}\|^2 I_{3\times 3} \tag{C.7}$$

$$S(\hat{k})^3 = -\|u\|^2 S(\hat{k}) \tag{C.8}$$

Bibliography

[1] J.D. Anderson, *Fundamentals of Aerodynamics*, McGraw Hill, 2001

[2] C.P. Coleman, "A Survey of Theoretical and Experimental Coaxial Rotor Aerodynamic Research", *National Aeronautics and Space Administration Technical Paper* 3675, 1997

[3] D. Choukroun, I.Y. Bar-Itzhack, Y. Oshman, "Novel Quaternion Kalman Filter", *IEEE Transactions on Aerospace and Electronics Systems*, Vol. 42, No.1, Jan. 2006

[4] J. Fleming, T. Jones, P. Gelhausen, D. Enns, "Improving Control System Effectiveness for Ducted Fan VTOL UAVs Operating in Crosswinds", *American Institute of Aeronautics and Astronautics*, 2003, AIAA Paper No. 2003-6514

[5] T. Hamel, R. Mahony, "Attitude estimation on SO(3) based on direct inertial measurements," To appear in International Conference on Robotics and Automation, 2006

[6] P.C. Hughes, *Spacecraft Attitude Dynamics*, Dover Publications, Inc., 2004

[7] S.M. Joshi, A.G.Kelkar, J.T-Y Wen, "Robust attitude stabilization of spacecraft using nonlinear quaternion feedback", *IEEE Transactions on Automatic Control*, Vol. 40, No. 10, pp. 1800-1803, 1995

[8] J. Katz and A. Plotkin, *Low-Speed Aerodynamics, 2nd Edition*, Cambridge University Press, 2001

[9] Taeyoung Lee, Amit Sanyal, Melvin Leok, N. Harris McClamroch, "Deterministic Global Attitude Estimation", *45th IEEE Conference on Decision and Control*, 2006,

[10] J.G. Leishman, *Principals of Helicopter Aerodynamics*, Cambridge University Press, 2000

[11] Larry Lipera, "The Micro Craft iSTAR Micro Air Vehicle: Control System Design and Testing", *American Helicopter Society 57th Annual Forum*, 2001

[12] F. Lizarralde and J.T.Wen, "Attitude control without angular velocity measurement: A passivity approach," *IEEE Transactions on Automatic Control*, Vol. 41, No. 3, pp. 468-472, 1996

[13] Robert Mahony, Tarek Hamel, Jean-Michel Pflimlin, "Complementary filter design on the special orthogonal group SO(3)", *44th IEEE Conference on Decision and Control, and the European Control Conference*, 2005

[14] R.M. Murray, Z. Li, and S.S. Sastry, *A Mathematical Introduction to Robotic Manipulation*, CRC Press, 1994

[15] D. Newman, *Interactive Aerospace Engineering and Design*, McGraw Hill, 2002

[16] W.K. Nicholson, *Elementary Linear Algebra, First Edition*, McGraw Hill Ryerson, 2001

[17] K. Ogata, *Modern Control Engineering, Fourth Edition*, Prentice Hall,2002

[18] J.M. Pflimlin, P. Soueres, T. Hamel, "Hovering flight stabilization in wind gusts for ducted fan UAV", *43rd IEEE Conference on Decision and Control*, December 14-17, 2004, Atlantis, Paradise Island, Bahamas

[19] R.W. Prouty, *Helicopter Performance, Stability, and Control*, Robert E. Krieger Publishing Company, Inc., 1986

[20] Henrik Rehbinder, Xiaoming Hu, "Drift-free attitude estimation for accelerated rigid bodies", *Automatica* 40, pg. 653-659, 2004

[21] M.D. Shuster, "A Survey of Attitude Representations", *The Journal of the Astonautical Sciences*, Vol. 41, No. 4, October-December 1993, pp.439-517

[22] M.D. Shuster, S.D. Oh, "Three Axis Attitude Determination from Vector Observations", *AIAA Journal on Guidance and Control*, Vol. 4, No.1, 1980

[23] M.W. Spong, M. Vidyasagar, *Robot Dynamics and Control*, John Wiley and Sons, 1989

[24] A. Tayebi, "Unit quaternion observer-based attitude stabilization of a rigid spacecraft without velocity measurment", *45th IEEE Conference on Decision and Control*, 2006,

[25] A. Tayebi, "A velocity free attitude tracking controller for rigid spacecraft", *in proceedings of the 46th IEEE conference on decision and control*, New Orleans, LA, USA, 2007

[26] A. Tayebi, S. McGilvray, "Attitude stabilization of a VTOL Quadrotor Aircraft", *IEEE Transactions on Control Systems Technology*, Vol. 14, No. 3, 2006

[27] A. Tayebi, S. McGilvray, A. Roberts and M. Moallem, "Attitude estimation and stabilization of a rigid body using low-cost sensors", *in proceedings of the 46th IEEE conference on decision and control*, New Orleans, LA, USA, 2007

[28] J. Thienel, R.M. Sanner, "A Coupled Nonlinear Spacecraft Attitude Controller and Observer With an Unknown Constant Gyro Bias and Gyro Noise", *IEEE Transactions on Automatic Control*, Vol. 48,No.11, November 2003

[29] John Ting-Yung Wen, Kenneth Kreutz-Delgado, "The Attitude Control Problem", *IEEE Transactions on Automatic Control*, Vol. 36, No. 10, October 1991,